FRACTIONAL DIFFUSION MODELING OF ELECTROMAGNETIC INDUCTION IN FRACTURED ROCKS

A Dissertation

by

JIANCHAO GE

Submitted to the Office of Graduate and Professional Studies of
Texas A&M University
in partial fulfillment of the requirements for the degree of

DOCTOR OF PHILOSOPHY

Chair of Committee,	Mark E. Everett
Committee Members,	Richard L. Gibson, Jr.
	Michael S. Pilant
	Yuefeng Sun
	Hongbin Zhan
Head of Department,	Rick Giardino

August 2014

Major Subject: Geophysics

ABSTRACT

The controlled-source electromagnetic (CSEM) technique is well-established for non-invasive geophysical survey. Due to the strong attenuation of earth materials to electromagnetic signals, the effective depth of most CSEM surveys is restricted to 1-2 km, a zone where pores and fractures over various length scales are highly complicated. Spatial confinement of fluid or electric charge transport by the fractal geometry gives rise to interesting dynamic processes within the pore space and fractures, such as anomalous diffusion.

Conventionally, CSEM data are interpreted in terms of a 1-D, 2-D or 3-D piecewise constant geological structure with uniform conductivity and thickness of each cell. A very fine grid, and hence a lot of computation time, are needed to build and evaluate a model that can explain the Earths actual 3D CSEM response. Good accuracy may not be captured, using the conventional approach, in the presence of multi-scale hierarchical geoelectrical structure. Alternatively, the CSEM response of such structures are easily evaluated if the physics of anomalous diffusion of electromagnetic eddy currents is recognized and cast, for example, in terms of a continuous time random walk. Such a re-formulation leads to a generalization of Maxwell equations containing a fractional order time derivative. The fractional order of the derivative is equivalent to a roughening of the geological medium, introducing multi-scale variations of fractures and heterogeneities in a compact manner. This theory renders CSEM modeling and inversion much more efficient, as only a few model parameters are now required to be fit. However the EM fractional diffusion theory is far from perfect, e.g. the correlation between the roughness of a fracture model with its fracture properties. In this research, I use numerical modeling tool to answer this

question and explore if classical piece-wise constant conductivity model can generate a fractional type response.

In this thesis, I will review the fundamental theory of traditional CSEM survey technique and the continuous time random walk approach, and review the derivation of the generalized Maxwell equation. More importantly, I propose the finite difference method to discrete the generalized Maxwell equation in 2D and 3D. I explore a classical fractured model response created from the von Kármán random media approach. I will show that the von Kármán fractured model generates a classical type response which is inconsistent with the fractional diffusion response. It is difficult to generate a classical model numerically that is comparable with the rough natural model.

ACKNOWLEDGEMENTS

I owe my most sincere gratitude to my advisor Professor Mark Everett, whose great character, enlightening instructions and consistent commitment lead me on the right track towards the Ph.D. As my role model, his life philosophy of being curious, optimistic and friendly keeps benefiting me all the time.

I thank Professor Richard Gibson. He provided me with systematic and rigrous basic training on being a qualified researcher during my first year is the foundation of my Ph.D research.

I owe my great appreciations to Professor Chester Weiss, for his consistent service as my external committee member and research collaborator. I owe my apologies for not being able to list his name on the front page of my thesis due to some format rules. His rich experiences and sharp perspectives on the CSEM and numerical modeling techniques send me much favorable guidance and greatly improves my thesis quality.

I also deeply appreciate Professor Michel Pilant, Professor Yuefeng Sun and Professor Hongbin Zhan for their commitment as my committees and the legendary geophysicist Professor Tony Gangi. Their enlightening discussions and suggestions broaden my vision and ensure my success.

I thank the Department of Geology and Geophysics in Texas A and M University, the Berg Hughes Center, National Science Foundation, BP Corporation, Conoco Philips, Marathon and Kelly Oil for their generous funding and fellowship support.

My thanks also goes to my colleagues and staffs in this department. Their companies during these years make my life much easier. The names on this list includes but not restricts to Kai Gao, Mark Heaney, Ronroy, Au Vuong, Zhao Zhang, Tingting Zhang, Jian Gong, Zhirui Zeng, Dehan Zhu, Qifei Huang.

Finally I would owe my success to my parents, Mrs. Yang Wang and Mr. Zongqi Ge, who are common people but a great mother and father. I have nothing but my success to pay back them for their bringing me up with pains and lots of troubles.

NOMENCLATURE

CG	Conjugate Gradient
CSEM	Controlled-Source Electromagnetic
CTRW	Continuous Time Random Walk
EM	Electromagnetic
GPR	Ground Penetrating Radar
G-S	Gaver-Stehfest
IP	Induced Polarization
LIN	Low Induction Number
FD	Finite Difference
MPI	Message Passing Interface
PETSc	Portable, Extensible Toolkit for Scientific Computation
QMR	Quasi Minimum Residue
TX	Transmitter
RX	Receiver
R-L	Riemman Louiville operator
TDEM	Time-Domain Electromagnetic

TABLE OF CONTENTS

Page

ABSTRACT ii

ACKNOWLEDGEMENTS iv

NOMENCLATURE vi

TABLE OF CONTENTS vii

LIST OF FIGURES ix

1. INTRODUCTION 1

2. OVERVIEW OF THE ELECTRIC PROPERTIES OF ROCKS AND CSEM TECHNIQUE 8

   2.1 Electrical properties of rocks and EM constitution laws 8
   2.2 Controlled-source electromagnetic induction system 10
   2.3 CSEM survey in time domain 12
   2.4 Analytical solution to a 1D-layered earth response of a loop source . . 13
   2.5 The 1D-layered earth response of a loop source in time domain 20
   2.6 Conclusion 25

3. THE FRACTIONAL DIFFUSION THEORY OF ELECTROMAGNETIC INDUCTION 29

   3.1 Introduction and background review 29
   3.2 The continuous time random walk analysis of fractional diffusion . . . 31
   3.3 The definition and some properties of the fractional derivative 35
   3.4 The connection between CTRW approach with EM fractional diffusion 38
   3.5 The fractional diffusion response of a loop transmitter over a layered earth 41
   3.6 Conclusion 45

4. FRACTIONAL DIFFUSION ANALYSIS OF THE ELECTROMAGNETIC FIELD IN FRACTURED MEDIA PART I: 2-D APPROACH 47

   4.1 Introduction 47

4.2 Theoretical background 49
4.3 Code development 51
4.4 Verification of the algorithm 53
4.5 Fractional diffusion analysis of a 2D fault contact model 57
4.6 Conclusion 61

5. FRACTIONAL DIFFUSION ANALYSIS OF THE ELECTROMAGNETIC FIELD IN FRACTURED MEDIA PART II: 3-D APPROACH 63

5.1 Introduction 63
5.2 Modeling method 65
5.2.1 Fundamental derivation 65
5.2.2 Discretization scheme 67
5.2.3 1D layered model verification 68
5.2.4 3D block model verification 71
5.3 3D Fractured model response investigation 74
5.3.1 3D random media model generalization 74
5.3.2 The effect of Hurst number on CSEM response 76
5.3.3 Multi-frequency fractional diffusion analysis 79
5.4 Conclusion 84

6. CONCLUSION 85

6.1 Future research plan 87

REFERENCES 89

APPENDIX A. DERIVATION OF THE SOLUTION TO EQUATION 2.12 IN WHOLE SPACE 97

APPENDIX B. THE FINITE DIFFERENCE REPRESENTATION OF EQUATION 4.7 100

LIST OF FIGURES

FIGURE Page

1.1 Map view of a 3D fracture block. The scaling of fractures is generated with power law density distribution. 3

1.2 Comparison of a Gaussian pulse undergoing classical diffusion and an anomalous pulse undergoing subdiffusion at different time steps. (Modified from [63]) 4

2.1 Typical ranges of electrical resistivity for important Earth materials. Repeated from [56]. 9

2.2 An illustration of various measurements in a step-off TEM survey. (a) The amplitude of a step-off DC current running in a TX; (b) the voltage of induced emf proportional to the change rate of the primary magnetic field; (c) the decaying secondary magnetic field is established at t_1 due to dissipation of induced currents. Modified from [20]. . . . 13

2.3 Illustration of the changing sign of magnetic flux at RXs due to different TX-RX separations. The induced current is established like a smoke ring (grey lines) moving downward and outward. . Modified from [22]. 14

2.4 The conceptual drawing of a 1D layered Earth model with n layers. . 15

2.5 The vertical component of the total magnetic to a 3-layer earth model with respect to the TX/RX offset. (Top) the real component; (bottom) the imaginary component. The conductivity of the subsurface background $\sigma_0 = 0.03$ S/m. The mid-layer conductivity σ_1 is varied at 0.001, 0.03 and 0.1 S/m to model a resistive layer, a whole space and conductive layer response. The profile is taken at the surface in $\hat{x}$ direction, 1m offset in $\hat{y}$ direction. The dashed line denotes a negative response and solid line denotes a positive response. 19

2.6 The vertical component of the secondary field to a 3-layer earth model with respect to the TX/RX offset. (Top) the real component; (bottom) the imaginary component. The configuration of the model is shown in Figure 2.5. 21

2.7 The total vertical magnetic response of a 3-layer earth model in time domain. The receiver is fixed at 60 m away in x direction. The conductive layer solution with $\sigma_1 = 0.1$ S/m; the resistive layer solution with $\sigma_1 = 0.001$ S/m. $\sigma_0 = 0.03$ S/m. The dashed line denotes a negative response. 23

2.8 The step-off vertical magnetic response of a 3-layer earth model in time domain. The receiver is fixed at 60 m away in x direction. The conductive layer solution with $\sigma_1 = 0.1$ S/m; the resistive layer solution with $\sigma_1 = 0.001$ S/m. $\sigma_0 = 0.03$ S/m. The dashed line denotes a negative response 26

2.9 The step-off vertical magnetic response of a 3-layer earth model in time domain for different conductive mid layer conductivity. The receiver is fixed at 60m away in x direction. The background conductivity $\sigma_0 = 0.03$ S/m. The conductive layer for the other two models are $\sigma_1 = 0.1$ S/m and $\sigma_1 = 1.0$ S/m respectively. The dashed line denotes a negative response. 26

2.10 The step-off vertical magnetic response of a 3-layer earth model in time domain for different resistive mid layer conductivity. The receiver is fixed at 60 m away in x direction. The background conductivity $\sigma_0 = 0.03$ S/m. The conductive layer for the other two models are $\sigma_1 = 0.01$ S/m and $\sigma_1 = 0.001$ S/m respectively. The dashed line denotes a negative response. 27

2.11 The step-off vertical magnetic response of a 3-layer earth model in time domain with different layer depth. The receiver is fixed at 60m away in x direction. The background conductivity $\sigma_0 = 0.03$ S/m. The mid layer conducitivity is $\sigma_1 = 0.1$ S/m. The layer depth for three models are 30-260 m, 50-280 m and 100-330 m. The dashed line denotes a negative response. 27

3.1 CTRW model of a particle on a discrete lattice. The waiting time of each step is symbolized by the area of the circle associated with each node. Repeated from [47] 34

3.2 The vertical magnetic response over a halfspace earth in classical and anomalous cases. The roughness of the lower space is (A)$\beta_1 = 1/5$ (B)$\beta_1 = 1/3$ (C)$\beta_1 = 1/2$ 43

3.3 The vertical magnetic response over a 3-layer earth with different roughness for the midlayer. The conductivity for the subsurface is $\sigma_0 = 0.03$ S/m. 44

3.4 The vertical magnetic response over a 3-layer earth with different roughness for the resistive midlayer. The conductivity for the background is $\sigma_0 = 0.03$ S/m and for the midlayer is $\sigma_1 = 0.001$ S/m. . . . 44

3.5 The vertical magnetic response over a 3-layer earth with different roughness for the conductive midlayer. The conductivity for the background is $\sigma_0 = 0.03$ S/m and for the midlayer is $\sigma_1 = 0.1$ S/m. 46

4.1 Schematic drawing of the half space model. The upper half of the plane consists of air, whose conductivity and roughness β are zero. The subsurface part has conductivity of 0.005 S/m and $\beta = 0.05$, which models a highly fractured and conductive formation. 54

4.2 (a) Comparisons between FD and analytical solutions for the total field e_y to the half space model. The air conductivity and roughness are zero, and the subsurface conductivity is 0.005 S/m and roughness 0.05. The receivers locate at $z = 0$, right at the interface. The positive direction along x points from left to the right, as indicated by the annotation. (b) The homogeneous model with whole space conductivity 0.005 S/m and roughness 0. This model is the reference model to reflect the error effect of discretization. Note that the 10 kHz Laplace frequency, s, results in a real-valued electric field. 56

4.3 Schematic drawing of the 2D fault model. Below the air-Earth interface, left of the fault zone conductivity is 0.005 S/m and roughness β is 0; right of the fault zone conductivity is 0.02 S/m and roughness β is 0. The conductivity and roughness of the fault zone are varied. The profiles location is at the interface. 58

4.4 FD solutions for the secondary e_y fields of the 2D fault model along x at $z = 0$. The conductivity of block is 0.5 S/m. The plot varies with different roughness of the zone ranging from 0.01 to 0.6. The configuration of the model is drawn in Figure 4.3. Note that the real-valued Laplace variable, s, results in a real-valued electric field. . . . 60

4.5 FD solutions for the secondary e_y fields of the 2D fault model along x at $z = 0$. The roughness β of the zone is 0.1. The plot varies with different conductivites ranging from 0.001 to 1.0 S/m of the zone. The profile layout is the same with Figure 4.4. Note that the real-valued Laplace variable, s, results in a real-valued electric field. 60

5.1 The 1-D layered model with rough conductive layer between z=30-260 m. There is excellent agreement in the real component at these frequencies. The cusps in the 100-Hz and 10-kHz response curves correspond to locations where the vertical magnetic field flips sign. As the frequency decreases below 1 Hz or increases above 10 kHz, the computational cell size becomes, respectively, too coarse or too fine relative to the skin depth of the EM signal to achieve such an excellent agreement. 69

5.2 Comparisons between FD (symbols) and 1-D analytic (lines) solutions for secondary B_z at (a) 1Hz, (b) 100Hz and (c) 10kHz. 70

5.3 Layout for a 3D conductive block model. Modified from [59]. 71

5.4 Comparisons between FD (red square dot) and FE analytic (blue round dot) solutions for secondary H_z of the 3D block model using a coarse grid. 72

5.5 Comparisons between FD (red square dot) and FE analytic (blue round dot) solutions for secondary H_z of the 3D block model using a fine grid. 73

5.6 Power spectra of the von Kármán correlation function: (a) Hurst number =-0.2, 0.4, 1.0, fixed characteristic length; (b) characteristic length a= 1 m, 100 m, 10 km, fixed Hurst number 77

5.7 Plane views of the top of 3-D random media conductivity models. (a) Top left: $\nu = 0.8, a = 1.0l$; (b) Top right: $\nu = 0.2, a = 1.0l$; (c) Bottom left: $\nu = -0.1, a = 1.0l$; (d) Bottom right: $\nu = 0.2, a = 0.1l$. Note that l is the dimension of the unit cell. The reddish brown color corresponds to conductive anomalies with maximum conductivity 0.1 S/m. The sandy yellow color corresponds to a resistive matrix with conductivity 0.03 S/m. 78

5.8 (Top left) The 3-D fractured model; (top right) the stochastic conductivity model of the fractured layer; (bottom) horizontal slice of the stochastic model, $\nu = 0.8$. 80

5.9 Amplitudes of real and imaginary components of B_z for models with Hurst numbers ν = -0.1, 0.2 and 0.8. 81

5.10 The workflow of the multi frequency test. 82

5.11 Comparisons between the classical von Kármán type ($\nu = -0.1$) fractured model responses (dashed lines), effective media solutions (dotted line) and fractional diffusion solutions to the rough block model (solid lines) at different frequencies. Amplitudes (left) and phases (right) of B_z are shown. The roughness of the block β=0.09, obtained by minimizing the misfit at 100Hz. 83

B.1 The coordinate system for the discretized grid around node (z_i, x_j). . 101

1. INTRODUCTION

The controlled-source electromagnetic (CSEM) technique is well-established for non-invasive geophysical surveys, with several variants, such as airborne, land, marine and borehole logging. Historically, it has been used for mineral mining [45] and unexploded ordnance detection [57]. Nowadays, its application has been successfully expanded to hydrocarbon exploration and production [16, 17, 48], aquiferous zone characterization [46], and lithosphere geological mapping [21], etc.. In a typical EM survey, the electromagnetic properties of geological formations, such as the electric conductivity and dielectric permittivity, are assessed by analyzing either natural or artificial EM signals that diffuse into the subsurface. The factors that affect the subsurface geoelectrical structure are various, generating a broad distribution of earth material resistivities, ranging from several 0.01 Ω·m to 100 kΩ·m. The electrolyte residing in fractures and pores within a rock matrix can make the geologic structure very complicated, and the interpretation is always nonunique. At locations where the pore-scale conductivity has a moderate contrast against the matrix, the subsurface fracture network plays a dominant role in forming the bulk geoelectrical conductivity. It is essential to study the spatial distribution of subsurface fractures, as part of a geophysical survey, for many engineering applications, such as the prediction of the fracture propagation in hydraulic fracturing reservoirs, and monitoring of fluid migration [28].

Many previous studies have shown that the scaling of geometric attributes of natural fractures, such as length, aperture and spacing, in the near-surface (upper

$\sim$100 m) follows a power-law scaling dependent function [9, 35]:

$$\phi = A(l/l_0)^{\gamma}, \tag{1.1}$$

where ϕ is a geometric attribute of natural fractures, l_0 is a characteristic scale and γ is a constant describing the decay rate of the power-law function. Figure 1.1 shows the top view of a 3D fracture block, with fracture midpoint position and orientation randomly generated. The length of the fractures follows a power-law distribution. Such fracture networks can form a fractal medium that is self-similar over a wide scale range and are described by a fractal dimension D, $2 < D < 3$ [35, 43]. The irregularities appear in the fractal geometry is quantitatively described by a parameter called "roughness", related to γ in Equation 1.1. In general, "roughness" γ is the fall-off rate of a scale-dependent power spectrum of any geometrical attributes in a model, such as the fracture surface topography, length, aperture, and density, in a microscopic view [35] and the bathymetry and topography of seafloors in a macroscopic view [30] (refering the power spectrum of a von Kármán random media in Figure 5.6. Previous studies [35, 30] show that the roughness is related to the fractal dimension by $D = \gamma - 3$. I will adopt the defination of "roughness" to define the parameter β in the EM fractional diffusion theory.

The confinement on fractal pathways of fluid particles gives rise to anomalous transport processes within the pore space and fractures. Such processes are also named fractional diffusion, multi-scale diffusion or non-Fickian diffusion, to differentiate them from the classical diffusion process governed by Fick's second law. Statistically, a fractional diffusion process does not exhibit a characteristic diffusion velocity, and the mean-square-displacement of a fluid particle or charge carrier is

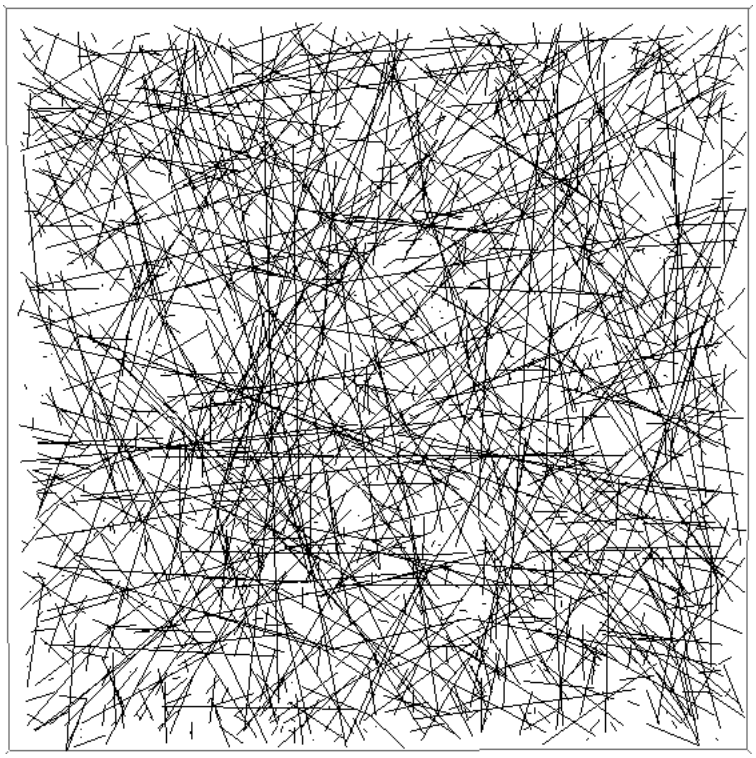

Figure 1.1: Map view of a 3D fracture block. The scaling of fractures is generated with power law density distribution.

proportional to a power law function of time:

$$< x^2(t) > \sim K_\alpha t^\alpha \tag{1.2}$$

where K_α is a generalized diffusion constant, and α varies from 0 to 1 in the case of a subdiffusive process, or 1 to 2 in the case of a superdiffusive process. In this research, the charge transport in fractured formations falls in the subdiffusion category, characterized by a late time long-tail signature in the beak-through curve at a given location (Figure 1.2) [63].

The CSEM technique analyzes the subsurface diffusion of electromagnetic eddy currents at sufficiently low frequencies ($\sigma \gg \omega\epsilon$) such that and displacement currents

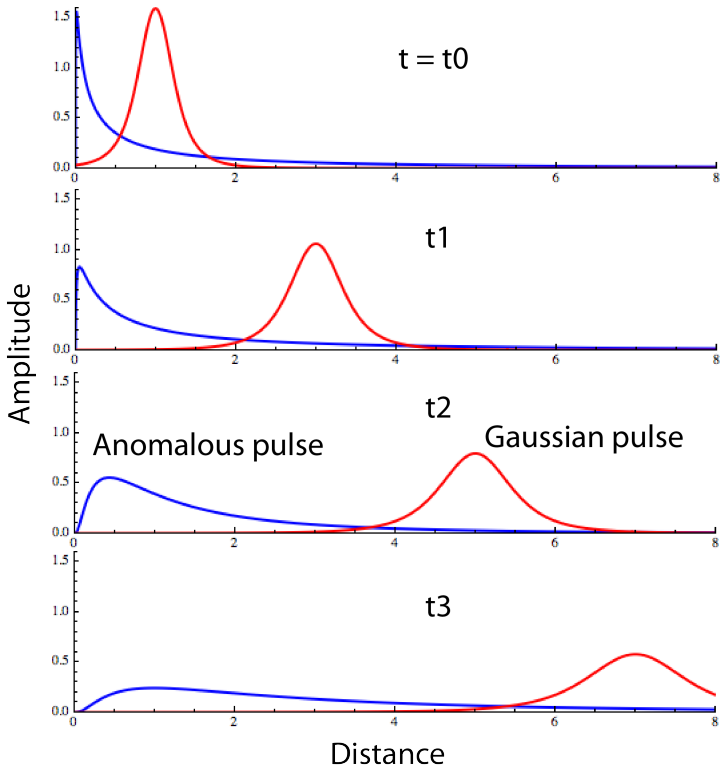

Figure 1.2: Comparison of a Gaussian pulse undergoing classical diffusion and an anomalous pulse undergoing subdiffusion at different time steps. (Modified from [63])

can be neglected. The induced eddy currents are mainly constituted by the migration of ions such as Na^+ and Cl^- in the pore fluid electrolyte. Thus the bulk geoelectrical conductivity of a naturally fractured subsurface is likely to have a similar fractal geometry as the fracture system itself. Moreover, the pathways of electrical charges are spatially correlated with those of hydraulic flow [12]. The theory for non-Fickian fluid transport in fracture rocks has been well established [7, 6]. The anomalous charge transport is thus considered to be analogous to the aforementioned results [19]. The fractional diffusion of EM eddy currents in fractured geological media is reported by [23, 73]. They found the measured zero crossing time in a transient loop-loop system exhibits a nonlinear dependent relationship with a fractional power

of source-receiver offset, denoting a subdiffusive process.

In an EM geophysical survey, the key task is to quantify the connection between CSEM data and parameters that describe the bulk electrical conductivity of the Earth. This can be assisted by numerical forward modeling to predict the Earth response based on a prior model, and an inversion calculation to extract the parameters of an unknown model based on observed responses. Conventionally, CSEM data are interpreted in terms of a multi-dimensional piecewise constant geological structure with uniform conductivity in each cell of a regular rectangular mesh. A very fine grid, and hence a long computation time, is needed to build and evaluate a model that can explain the Earth's 3D response. Good accuracy may not be captured, using the conventional approach, in the presence of multi-scale hierarchical fractal geoelectrical structure. Alternatively, the CSEM response of such structures are easily evaluated if the physics of anomalous diffusion of electromagnetic eddy currents is recognized. The governing Maxwell equation in such a case can be re-cast in terms of a continuous time random walk (CTRW) [47]. Such a re-formulation leads to a generalization of Maxwell equations containing a fractional order time derivative[19, 26]. The fractional order of the time derivative is equivalent to a "spatial roughening" of the geological medium, introducing multi-scale variations due to fractures and heterogeneities in a compact manner. This theory renders CSEM modeling and inversion much more efficient, as only a few model parameters are needed to describe this type of medium.

The Maxwell fractional-derivative equation can be solved using the finite difference (FD) method in either time, Laplace, or frequency domain. Most of the time domain methods are implicit. The time domain methods are memory intensive since to compute the response at each time step, solutions from previous steps are involved. Yuste and Acebo [78] proposed a memory-efficient, explicit method based

on a first-order truncated Grünwald-Letnikov fractional derivative. On the other hand, the fractional Maxwell equation can be solved in Laplace or frequency domain. The Laplace transform of a fractional derivative is just a power law function of the Laplace variable s [54]. Everett [19] derived the 1-D analytical solution to the fractional Maxwell equation in Laplace domain and transformed the response to time domain using the Gaver-Stehfest method.

In this research, a pair of finite difference algorithms are developed to discretize the Laplace domain fractional Maxwell equation on 2D and 3D grids. The 2D algorithm investigates the response of a fracture zone excited by an infinite line source lying along the strike direction. This provides a simple example of a fractional diffusion type EM response. I show that a fractal target may be hidden from detection even if its conductivity is different from that of the background formation. The 3D algorithm is used to compare the response of a fractured medium excited by a horizontal magnetic loop source. I explore the classical fractured model scenario, to check whether the classical diffusion fractured model could generate a fractional-diffusion-type response. By comparing the 3D classical fractured and 3D rough block model responses, I quantitatively determine the correlation between the roughness and the fracture density or length scale distribution. The 2D and 3D algorithms can also provide assistance with experiment design. Since the secondary field formulation is used, the type of the source can be easily converted to other types, such as a grounded dipole source.

The remainder of the thesis is organized as follows: Chapter 2 provides an overview of the electrical property of rocks and the fundamentals of CSEM techniques; Chapter 3 provides an overview of the fundamental theory of fractional diffusion and how it is applied to geophysical exploration using the CTRW method; Chapter 4 presents 2D fractured zone modeling, based on an infinite line source,

which is published in *Geophysics* [26]; Chapter 5 presents 3D classical fractured modeling and a comparison of the classical model response with the anomalous type response, which will be submitted to *Geophysics* for the publication. Chapter 6 provides the conclusions and outlines some future work.

2. OVERVIEW OF THE ELECTRIC PROPERTIES OF ROCKS AND CSEM TECHNIQUE

2.1 Electrical properties of rocks and EM constitution laws

The electrical properties of Earth materials include its electrical conductivity σ and electric permittivity ϵ. Electrical conductivity measures the resistance of a material to the establishment of long term current flow through it. The resistivity ρ is the inverse of the conductivity. It varies widely over several decades throughout the earth (Figure 2.1). It is the most important property in terms of low frequency (kHz-MHz) EM induction surveys, and is governed by the mobility of free charge carriers in the medium. Electric permittivity measures the ability of a material to become polarized by an external electric field, i.e. how easily a dielectric polarizes in response to an external electric field. The free space electric permittivity is equal to 8.854×10^{-12}F/m. Electric permittivity is frequency dependent. It is an important property for induced polarization (IP) surveys and also ground penetrating radar (GPR). The latter is an electromagnetic technique that operates in a much higher frequency range (>100 MHz).

The magnetic permeability μ measures the ability of a material to become magnetized by an external magnetic field. In free space or geological media in which no magnetic material is present, μ equals $4\pi \times 10^{-7}$H/m.

The most important constitutive equation in EM induction is Ohm's law, stating that if a sample of conducting material is placed in an external electric field $\mathbf{E}$, a current of density $\mathbf{J}$ $[A/m^2]$will flow in the material:

$$\mathbf{J} = \bar{\sigma}(r)\mathbf{E} \tag{2.1}$$

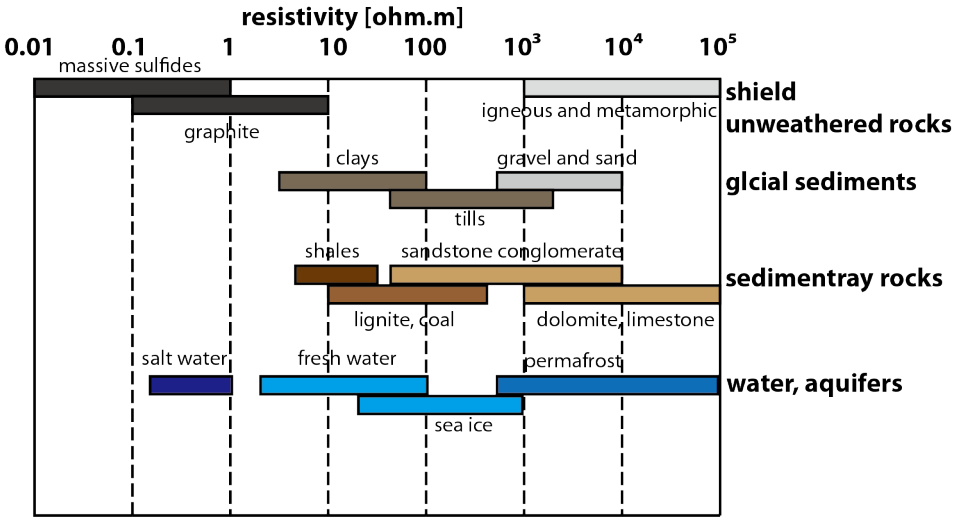

Figure 2.1: Typical ranges of electrical resistivity for important Earth materials. Repeated from [56].

In Equation 2.1, $\bar{\sigma}$ is the electrical conductivity tensor, which must be determined empirically. If the material is found to be linear and isotropic, the conductivity tensor reduces to a scalar quantity. The vertical electrical anisotropy is very important in marine EM exploration surveys, due to sedimentary depositional sequences. The vertical resistivity ρ_v is often measured to be greater than the horizontal resistivity ρ_h. An intermediate ratio between ρ_v and ρ_h in a marine crustal setting equals $2.0 \sim 3.0$ [42]. The effect on the EM response of the anisotropy depends on the TX-RX geometry and can make the interpretation more complicated.

In the near-surface environment, most rocks are composed of silicate minerals, which are essentially resistive. Water or sometimes clay is often the only conductive material presenting in the pore space within the matrix. The conductivity of porous rocks depends primarily on the porosity, the connectivity among fractures, and to a lesser extent, temperature. An empirical formula relating bulk conductivity to

porosity in fully saturated rocks is given by Archies law [2]:

$$\sigma = a\sigma_w W^m, \tag{2.2}$$

where σ_w is the conductivity of the aqueous electrolyte, W is the fraction of the volume of pore space to the total volume of the rock and a and m are empirically determined parameters. For partially saturated rocks, Archie's law is modified to:

$$\sigma = a\sigma_w S^n \theta^m, \tag{2.3}$$

where $n \approx 2$ is empirically determined, S is the fraction of the pore volume filled with aqueous electrolyte and θ is the volume fraction of space filled by gas or air in the rock.

2.2 Controlled-source electromagnetic induction system

Controlled sources that are used in a near surface prospecting survey may be either of the grounded type, such as the electric dipoles used in the resistivity method, or of the inductive type in which direct electrical contact with the ground may be avoided by using a loop source. In the latter case, the source-ground coupling is achieved by magnetic flux linkage. A summary of the early history of various types of electromagnetic exploration techniques can be found in [70].

The principle of an CSEM induction survey in the frequency domain is as follows [20]: an alternating current is passed through the transmitter (TX) coil, which generates an alternating primary magnetic field $\mathbf{B}^p(\mathbf{r}, t)$ that diffuses into the ground. When this primary field passes through the target anomaly, it generates an electromotive force, in proportion to the rate of change of primary field, which in turn drives the free charges in the conductive target to circulate inside the body, thereby

forming eddy currents. Since the eddy currents are also alternating, they further induce a secondary field $\mathbf{B}^s(\mathbf{r}, t)$, that is characteristic of the target geometry, position and conductivity. Both primary and secondary field signals are recorded by receiver (RX) coils. Since the primary field is known, depending on the TX design and the survey geometry, it can be compensated to leave only the secondary field in the data.

In a frequency domain survey, it is typical to interpret the data in terms of the apparent conductivity as a function of the transmitter/receiver midpoint position along the profile. At low induction number (TX-RX offset $s \ll \delta$) where δ is skin depth, see below, the apparent conductivity σ_A is equivalent to the conductivity of a homogeneous halfspace that would generate an identical EM response with the observed response [44]:

$$\sigma_A = \frac{4}{\mu_0 \omega s^2} Im \frac{\mathbf{B}^s}{\mathbf{B}^p} \tag{2.4}$$

where ω is the angular frequency of the source, s is the transmitter/receiver spacing and Im indicates imaginary part of the response. The apparent conductivity can be interpreted as a spatial average of the underlying conductivity distribution within the footprint of the instrument between the transmitter and receiver. The penetration depth of EM signals in the frequency domain is defined by the skin depth:

$$\delta = \sqrt{\frac{2}{\mu \sigma \omega}}, \tag{2.5}$$

indicating that incident signals lose exactly $1/e$ of their strength at the surface after penetrating one skin depth. According to Equation 2.5, the attenuation or the skin effect of earth materials increases with increasing frequency and conductivity. Usually a frequency domain EM survey is applied at sufficiently low frequencies to guarantee that the skin depth is much greater than the intercoil spacing. This is

called the LIN (low-induction-number) regime.

2.3 CSEM survey in time domain

A CSEM induction survey can be implemented in time domain as well. The induction process is equivalent to the diffusion of an image of the TX loop into a conductive medium, much similar to hydrodynamic vortex motion. In contrast to the source current used in a frequency domain survey, a typical current wave form $I(t)$ consists of slow rise to a steady value of I_0 followed by a rapid shut-off, as shown in Figure 2.2 [20]. Passing a disturbance such as this through the TX loop generates a primary magnetic field that is in-phase with, and proportional to, the TX current. After the ramp is terminated, the electromotive force vanishes and the eddy currents start to decay via Ohmic dissipation of heat. A secondary magnetic field is produced in proportion to the waning strength of the eddy currents. The receiver coil voltage measures the time rate of change of the decaying secondary magnetic field. As the eddy currents diffuse downward through the subsurface, the current vortex maintains the shape of the loop, much like the motion of a smoke ring [50]. The flux of secondary field induced by eddy currents passing the reciever coils changes sign as the eddy current smoke ring passes beneath the receiver (Figure 2.3 [20]). The zero crossing time measures the time taken for the flux to change sign from negative to positive. It is also can be thought as the traveltime for the eddy currents to diffuse from TX to RX.

The conductivity of the ground can be estimated from time-domain electromagnetic (TDEM) offset-loop sounding responses by analyzing the zero-crossing time at which sign reversals occur in the various RX coils. An apparent conductivity profile can be extracted from the TDEM data as well. The apparent conductivity at each time gate is calculated by matching the response at that time gate to the synthetic

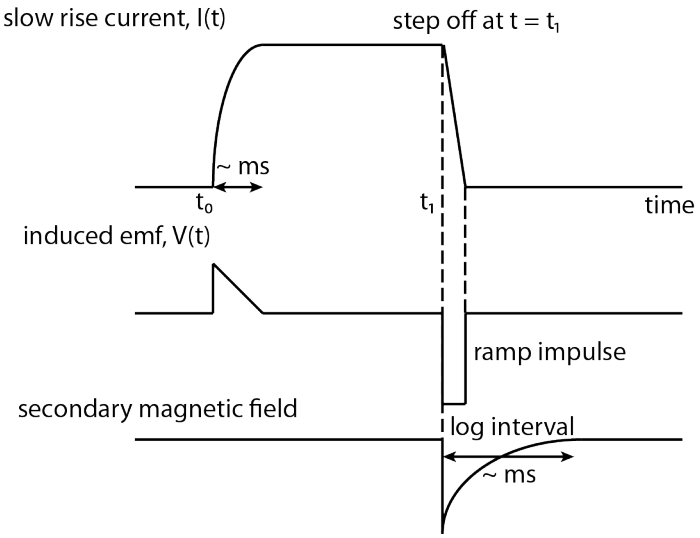

Figure 2.2: An illustration of various measurements in a step-off TEM survey. (a) The amplitude of a step-off DC current running in a TX; (b) the voltage of induced emf proportional to the change rate of the primary magnetic field; (c) the decaying secondary magnetic field is established at t_1 due to dissipation of induced currents. Modified from [20].

response of a uniform half-space.

2.4 Analytical solution to a 1D-layered earth response of a loop source

As an electromagnetic phenomenon, the CSEM geophysical prospecting technique is governed by the well-known Maxwell's equations:

$$\nabla \cdot \mathbf{E} = \frac{\rho}{\epsilon_0} \tag{2.6}$$

$$\nabla \cdot \mathbf{B} = 0 \tag{2.7}$$

$$\nabla \times \mathbf{E} = -\frac{\partial \mathbf{B}}{\partial t} \tag{2.8}$$

$$\nabla \times \mathbf{B} = \mu_0 \sigma \mathbf{E} + \mu_0 \mathbf{J_s} + \mu_0 \epsilon_0 \frac{\partial \mathbf{E}}{\partial t} \tag{2.9}$$

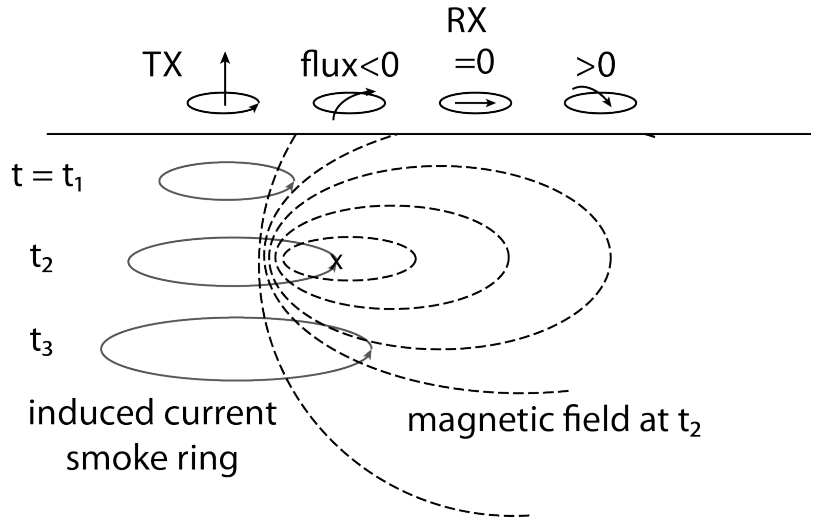

Figure 2.3: Illustration of the changing sign of magnetic flux at RXs due to different TX-RX separations. The induced current is established like a smoke ring (grey lines) moving downward and outward. . Modified from [22].

implying Gauss's electric and magnetic laws, Faraday's law and Ampeŕe's law respectively, where ρ is the volume electric charge density and $\mathbf{J}_s$ is the current density, depending on the form of the source. The above equations on hold for linear homogeneous media, where the quantities ϵ_0 and μ_0 are scalar constant. In Equation 2.9, the first two terms of right hand side are the damping terms describing the conduction current, implying Ohm's law and dominating in low frequency range. The third term of right hand side is the lossless term describing the displacement current associated with the change of electric displacement field and molecular polarization. The latter term is dominating in the high frequency range, and can be neglected in the CSEM frequency range (below 1 MHz). By neglecting the displacement current term, and combining Equations 2.8 and 2.9, a diffusion equation for the electric field can be obtained:

$$\nabla \times \nabla \times \mathbf{E} = -\mu_0 \sigma_0 \frac{\partial \mathbf{E}}{\partial t} - \mu_0 \frac{\partial \mathbf{J_s}}{\partial t} \tag{2.10}$$

To start deriving the analytical solution to EM responses of a loop source lying over a layered Earth, the model shown in Figure 2.4 is used. The model has n layers including the basal half-space. Each layer has a set of unique electric properties and a thickness. The vertical positive direction is pointing downward. The current distribution of the loop source, lying at height h m above the surface with radius equal to a, is defined by:

$$\mathbf{J_s} = \frac{I(\omega)a}{\rho}\delta(\rho - a)\delta(z + h)\hat{\phi}, \tag{2.11}$$

where $I(omega)$ is the current density in the loop, a is the radius of the loop and $\hat{\phi}$ is the azimuthal direction vector. Assuming a time harmonic dependence of $e^{i\omega t}$ for the current, and applying the Fourier transform to Equation 2.10 into frequency domain:

$$\nabla \times \nabla \times \mathbf{e} = -i\omega\mu_0\sigma_0\frac{\partial \mathbf{e}}{\partial t} - i\omega\mu_0\frac{\partial \mathbf{J_s}}{\partial t} \tag{2.12}$$

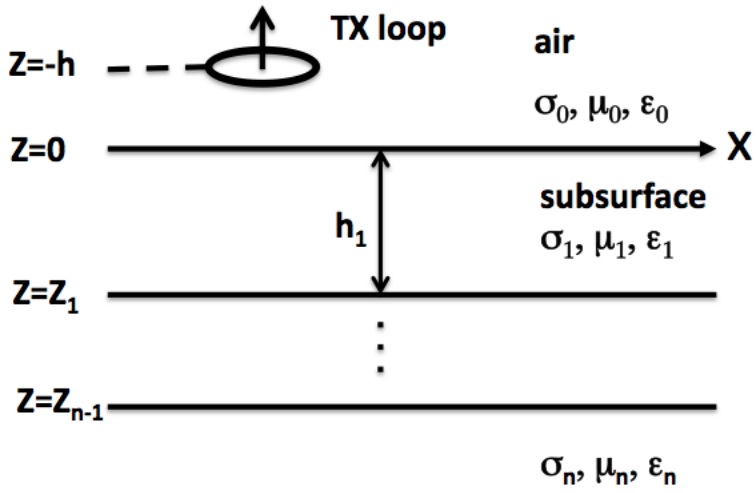

Figure 2.4: The conceptual drawing of a 1D layered Earth model with n layers.

If Equation 2.12 is solved for a uniform halfspace model, then the solution represents the primary field for the loop source. The primary field refers to the field induced directly by the physical source, without involvement of any scattered field that are induced by subsurface anomalies. The solution to the primary field of Equation 2.12 in the uniform whole space is expressed in terms of Hankel transform:

$$\begin{aligned} e_{\phi}^{p}(\rho,z)^{whole} &= \frac{-i\mu_0\omega Ia}{2}\int_0^{\infty}\frac{\lambda}{\gamma_0}e^{\gamma_0(z+h)}J_1(\lambda a)J_1(\lambda\rho)d\lambda, \quad z<-h \\ e_{\phi}^{p}(\rho,z)^{whole} &= \frac{-i\mu_0\omega Ia}{2}\int_0^{\infty}\frac{\lambda}{\gamma_0}e^{-\gamma_0(z+h)}J_1(\lambda a)J_1(\lambda\rho)d\lambda, \quad z>-h \end{aligned} \tag{2.13}$$

where $\gamma_0^2 = \lambda^2 + i\mu_0\sigma_0\omega$, and $J_1(x)$ is the Bessel function of the first kind. The positive and negative signs in the exponential function indicate upward and doward diffusion of the field. Details of the derivation is described in Appendix A. To generalize the solution 2.13 to a model with n layers, just as Figure 2.4 shows, a reflection coefficient is included:

$$e_{\phi}^{p}(\rho,z) = \frac{-i\mu_0\omega Ia}{2}\int_0^{\infty}(e^{-\gamma_0(z+h)} + r_{TE}e^{\gamma_0(z-h)})\frac{\lambda}{\gamma_0}J_1(\lambda a)J_1(\lambda\rho)d\lambda \tag{2.14}$$

where the reflection coefficient r_{TE} of the TE mode is calculated by the recursive matrix method, by considering the boundary conditions at layer interfaces, the result is [71]:

$$r_{TE} = \frac{Y_0 - \hat{Y}_1}{Y_0 + \hat{Y}_1} \tag{2.15}$$

with

$$Y_0 = \frac{\gamma_0}{i\omega\mu_0} \text{ (intrinsic admittance of free space)} \tag{2.16}$$

For an n-layer case, the surface admittance $\hat{Y}_1$is given by the recurrence relation:

$$\hat{Y}_1 = Y_1 \frac{\hat{Y}_2 + Y_1 \tanh(\gamma_1 h_1)}{Y_1 + \hat{Y}_2 \tanh(\gamma_1 h_1)} \tag{2.17}$$

$$\hat{Y}_{n-1} = Y_{n-1} \frac{\hat{Y}_n + Y_{n-1} \tanh(\gamma_{n-1} h_{n-1})}{Y_{n-1} + \hat{Y}_n \tanh(\gamma_{n-1} h_{n-1})} \tag{2.18}$$

and

$$\hat{Y}_n = Y_n = \frac{\gamma_n}{i\omega\mu_n} \tag{2.19}$$

The recursion is started from the admittance of the base layer and calculated upward to the surface, until the reflection coefficient r_{TE} is at last obtained.

Using Faraday's law and Equation 2.14, the radial and vertical components of magnetic field are:

$$b_\rho^p(\rho, z) = \frac{\mu_0 I a}{2} \int_0^\infty (e^{-\gamma_0(z+h)} - r_{TE} e^{\gamma_0(z-h)}) \lambda J_1(\lambda a) J_1(\lambda \rho) d\lambda \tag{2.20}$$

and

$$b_z^p(\rho, z) = \frac{\mu_0 I a}{2} \int_0^\infty (e^{-\gamma_0(z+h)} + r_{TE} e^{\gamma_0(z-h)}) \frac{\lambda^2}{\gamma_0} J_1(\lambda a) J_0(\lambda \rho) d\lambda \tag{2.21}$$

To numerically compute the Hankel transform in the above equations of the type:

$$\Psi(\rho) = \int_0^\infty K(\lambda, \rho) J_i(\lambda \rho) d\lambda, \tag{2.22}$$

where $K(\lambda, \rho)$ is the kernel function being transformed, the digital filter method [31] is used. In brief, the method evaluates the kernel function at a series of wavenumber

λ_i, multiplying each by a prior determined weight. The abscissa of λ_i is determined by the shift a and the sampling interval s:

$$\lambda_i = \frac{1}{\rho} \times 10^{a+(i-1)s}, \quad i = 1, 2, ...n. \tag{2.23}$$

The integral in 2.22 is approximated by the sum of the products between the kernel functions $K(\lambda_i, \rho)$ and the specific weights W_i:

$$\Psi(\rho) = \frac{1}{\rho} \sum_{i=1}^{n} K(\lambda_i, \rho) W_i \tag{2.24}$$

For the Hankel transform of J_1 type, the weights are prior determined at $n = 47$ points or $n = 140$ points for higher accuracy.

Figure 2.5 shows the analytical form of the vertical total magnetic response $B_z(x)$ of a 3-layer earth model with respect to the TX/RX offset. The loop's radius is 3 m and the current density I_0 running in the loop is 1 A. The subsurface has three layers, where the top of the second layer is at 30 m depth and the contact with the bottom layer is at 260 m. The top and base layer have the same conductivity $\sigma_0 = 0.03$ S/m. The mid-layer conductivity σ_1 is varied at 0.001, 0.03 and 0.1 S/m to model a resistive layer, a whole space and a conductive layer response. The profile is along the surface in the $\hat{x}$ direction, and the source is offset by 1 m in the $\hat{y}$ direction.

In the real component response, the resistive layer is difficult to observe since the difference is small with the whole space solution at most locations, due to an inductive EM survey being insensitive to resistive targets. The conductive layer response begins to deviate from the other two at around 400m. In the imaginary component, all of the three responses show a sign flip at a characteristic location. The mechanism is explained as in Figure 2.3, due to the opposite directions of the magnetic field flux

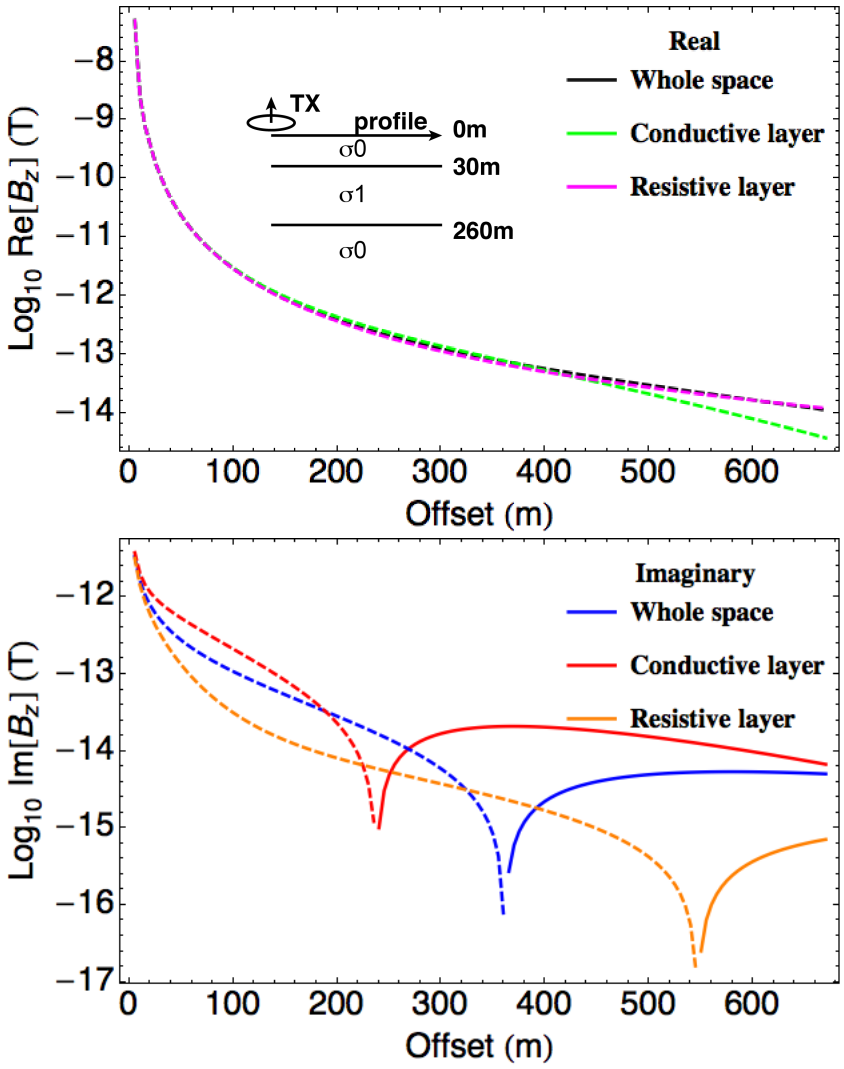

Figure 2.5: The vertical component of the total magnetic to a 3-layer earth model with respect to the TX/RX offset. (Top) the real component; (bottom) the imaginary component. The conductivity of the subsurface background $\sigma_0 = 0.03$ S/m. The mid-layer conductivity σ_1 is varied at 0.001, 0.03 and 0.1 S/m to model a resistive layer, a whole space and conductive layer response. The profile is taken at the surface in $\hat{x}$ direction, 1m offset in $\hat{y}$ direction. The dashed line denotes a negative response and solid line denotes a positive response.

that passes through the loop. For a conductive layer, which attenuates much of the field, the flux changes sign in to the area close to the source. The conductivity contrast between the mid-layer and the background is easily recognized in the imaginary component response.

On the other hand, the primary response $\mathbf{b^p}$ is essentially generated by a simple background model without an anomaly. In the 3-layer model, the mid-layer serves as the anomaly if its conductivity is different from those of the other layers. The primary response is thus generated by the halfspace background model. The secondary response $\mathbf{b^s}$ of the anomaly-layer is the difference between the total response $\mathbf{b^t}$ of the 3-layer model and the primary response $\mathbf{b^p}$ of the half space model:

$$\mathbf{b^s} = \mathbf{b^t} - \mathbf{b^p} \tag{2.25}$$

The secondary responses of the conductive layer model and resistive layer model are shown in Figure 2.6. For both components, the sign of the conductive layer response flips from negtive to positive while the resistive layer response behaves the opposite way. Comparing Figure 2.5 and 2.6, the magnitude of the real component of the total field is two orders greater than the secondary field. The character of the anomaly response is much overwhelmed by the primary response and difficult to be detect. However the secondary response is a more sensitive indicator of the conductivity anomaly.

2.5 The 1D-layered earth response of a loop source in time domain

To numerically calculate EM responses in the time domain, Equation set 2.8, 2.9 or 2.12 can be solved directly. However, to directly solve the time domain equation, one needs to start from a very early time step with an initial condition assumed, and calculate the response each time step until the required time range is covered.

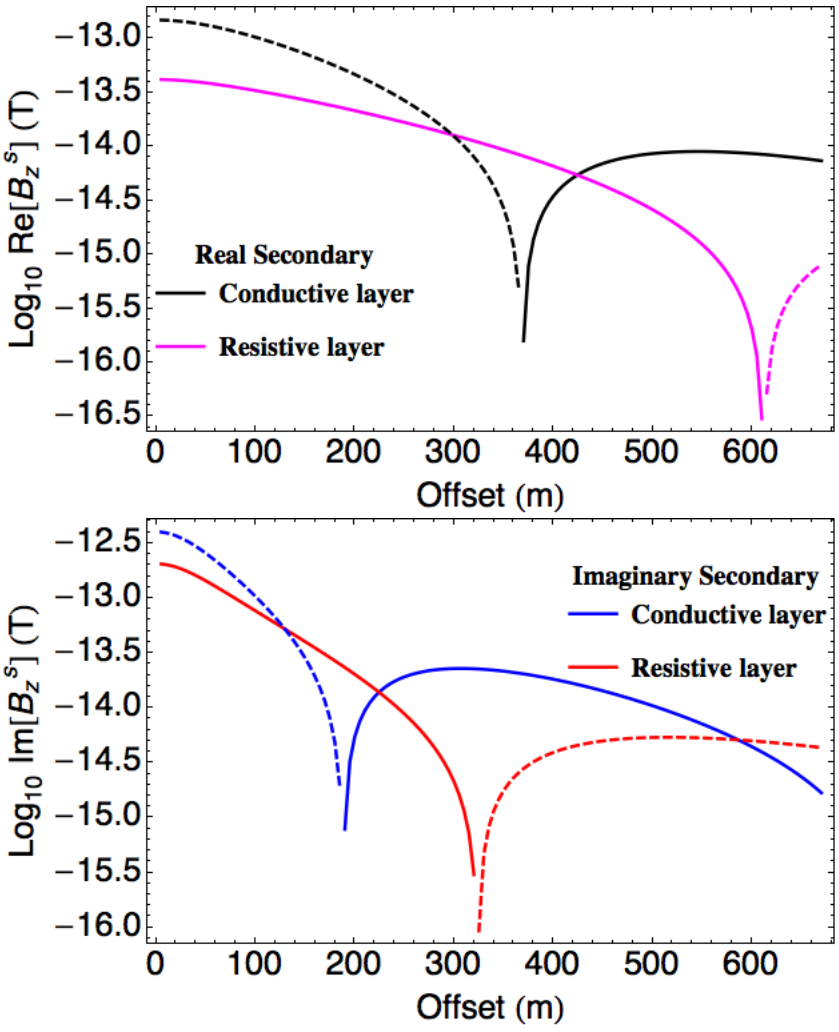

Figure 2.6: The vertical component of the secondary field to a 3-layer earth model with respect to the TX/RX offset. (Top) the real component; (bottom) the imaginary component. The configuration of the model is shown in Figure 2.5.

The early time steps need to be small to meet the stability condition of the solver, which is computational cost consuming. Alternatively, one can solve the governing equations in Laplace domain with several frequencies and the transform the solutions back to get the time domain solution. The desired time step response can be obtained without solving the full range of all time steps.

While several methods are available to perform the inverse Laplace transform [13, 15], the Gaver-Stehfest (GS) algorithm [25, 67] has long proven reliable for computing transient controlled-source EM responses in geophysics [38, 21].

Given the magnetic responses $b(s)$ in the Laplace domain, the corresponding impulse response $B(t)$ may be easily found in the time domain. The GS approximation $\hat{B}(t)$ to $B(t)$ is defined by

$$\hat{B}(t) = \frac{ln2}{t} \sum_{j=1}^{n} c_j(n) b(\frac{jln2}{t}), \tag{2.26}$$

where the GS coefficients $\{c_j(n)\}$ for $j = 1, 2, ..., n$, with n even, are given by

$$c_j(n) = (-1)^{\frac{n}{2}+j} \sum_{k=\frac{j+1}{2}}^{min(j,\frac{n}{2})} \frac{k^{\frac{n}{2}}(2k)!}{(n/2-k)!k!(k-1)!(j-k)!(2k-j)!}. \tag{2.27}$$

Note that according to Equation 2.26, the Laplace variable s is required to be a real number only ($s_j = j\frac{ln2}{t}$for $j = 1, ..., n$), without an imaginary part. This results in a purely real $b(s)$ as well. Provided the time domain solution $B(t)$ has no discontinuites, sharp peaks or rapid oscillations, the GS algorithm provides good accuracy. The number of Laplace function ($b(s)$) required in Equation 2.26 has an appropriate range from 8 to 18 [19]. Too many or too few values may result in excessive rounding errors. After calculating the function of $B(t)$ at a series of discrete time steps, a smoother time domain solution can be obtained by spline interpolation

of responses at these time steps. A detailed derivation of the GS algorithm can be found in [18].

Figure 2.7 shows the total impulse response to a 3-layered model based on the GS approximation to Equation 2.21. The configuration is the same Figure 2.5, including the whole space, conductive layer and resistive layer, respectively. The position of the receiver is fixed at 60 m from the source in $\hat{x}$ direction. The response is flat at early time less than 10^{-5} s. Then the negative response changes to a positive response at the zero crossing time and decays with time. The three responses coincide with each other in the negative region but differentiate after turning into the positive region. The resistive layer response decays faster than the other two, and has a kink in the middle of the curve. The conductive layer response decays slower.

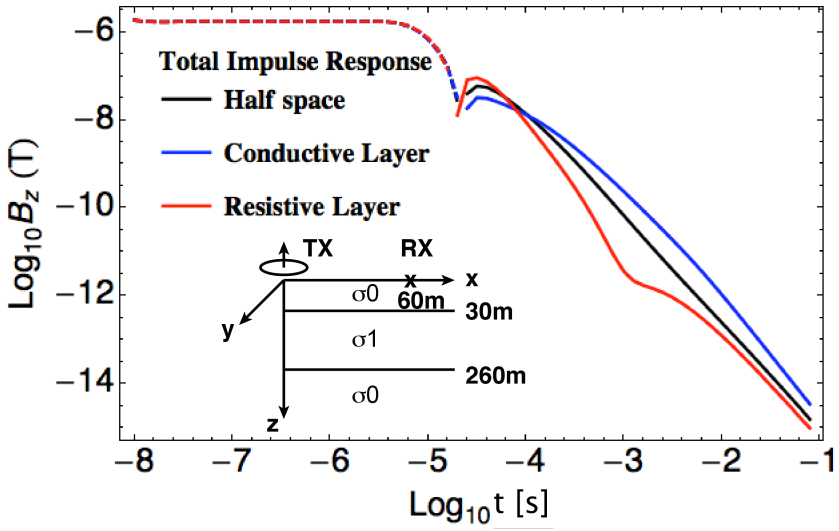

Figure 2.7: The total vertical magnetic response of a 3-layer earth model in time domain. The receiver is fixed at 60 m away in x direction. The conductive layer solution with $\sigma_1 = 0.1$ S/m; the resistive layer solution with $\sigma_1 = 0.001$ S/m. $\sigma_0 = 0.03$ S/m. The dashed line denotes a negative response.

In an actual transient EM survey, the step-off response is attractive to practition-

ers, since measurements of secondary responses may be made while primary response is off (Figure 2.2). Noted the direct GS approximation to the Equation 2.21 results in the impulse response. The step-on response $g^{step-on}(t)$ is given by the integral of the impulse response $g^{impulse}(t)$, which for a causal system is:

$$g^{step-on}(t) = \int_0^t g^{impulse}(\tau)d\tau \quad t \geq 0 \tag{2.28}$$

Then the step-off response after a constant current is turned off is [71]:

$$g^{step-off}(t) = \int_t^\infty g^{impulse}(\tau)d\tau = \int_0^\infty g^{impulse}(\tau)d\tau - \int_0^t g^{impulse}(\tau)d\tau \quad t \geq 0, \tag{2.29}$$

or

$$g^{step-off}(t) = g^{DC}(t) - g^{step-on} \tag{2.30}$$

According to 2.30, to calculate the step-off response, it is convenient to first compute the step-on response from the impulse response, which in the Laplace domain, is found using the formula:

$$L\{g(t)h(t)\} = \frac{G(s)}{s}, \tag{2.31}$$

where the $h(t)$ is the Heaviside step-on function defined by

$$h(t) = \begin{cases} 0, & t < 0_- \\ 1, & t > 0_+ \end{cases} \tag{2.32}$$

Thus the step-on response can be obtained by the GS approximation to Equation 2.21 divided by s:

$$b_z^{step-on}(\rho, z) = \frac{\mu_0 Ia}{2s} \int_0^\infty (e^{-\gamma_0(z+h)} + r_{TE}e^{\gamma_0(z-h)})\frac{\lambda^2}{\gamma_0}J_1(\lambda a)J_0(\lambda\rho)d\lambda \tag{2.33}$$

The step-off response will be:

$$b_z^{step-off}(t) = b_z^{DC} - b_z^{step-on}(t) \tag{2.34}$$

Figure 2.8 shows the step-off vertical magnetic response of the 3-layer model. Note that the half-space model response follows a $t^{-3/2}$ power-law decay, which is marked by the 56.3° asymptotic line on the graph. The late-time power-law decay rate does not depend on the conductivity of the subsurface or the TX-RX separation. This will be a critical hint to differentiate the classical model response from the anomalous response as shown in later chapters [19].

Figures 2.9 and 2.10 show the trend for the conductive layer model step-off responses and resistive model responses. For conductive layer models, the magnetic responses are more sensitive and show significant differences among the different conductivites.

Figure 2.11 shows the model step-off responses for different conductive layer depths at 30-260m, 50-280m and 100-330m. From the graphs shown, the deeper the layer, the weaker the anomaly response. For the response of the 100-330 m layer, the curve even bends inward and shows a resistive like character.

2.6 Conclusion

In this chapter, I have reviewed some of the fundamentals of geophysical electromagnetism, including the electrical property of rocks and EM constitutive laws. The CSEM survey frequency range is below 1 MHz, where the displacement currents can be ignored. The techniques of frequency domain and time domain CSEM surveys are introduced. Traditionally the observed data are converted to an apparent conductivity profile for interpretation. The zero crossing time is when the sign of responses flip in time domain. The analytical solution to the 1D layered model response of a mag-

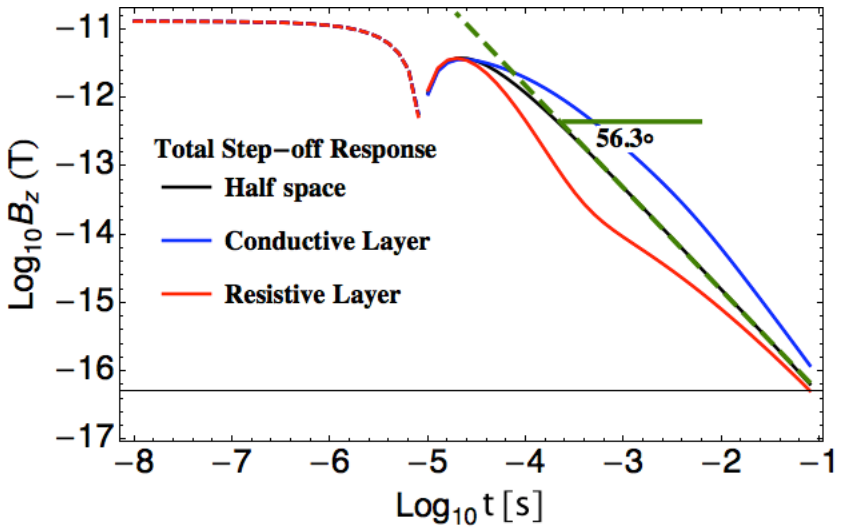

Figure 2.8: The step-off vertical magnetic response of a 3-layer earth model in time domain. The receiver is fixed at 60 m away in x direction. The conductive layer solution with $\sigma_1 = 0.1$ S/m; the resistive layer solution with $\sigma_1 = 0.001$ S/m. $\sigma_0 = 0.03$ S/m. The dashed line denotes a negative response

.

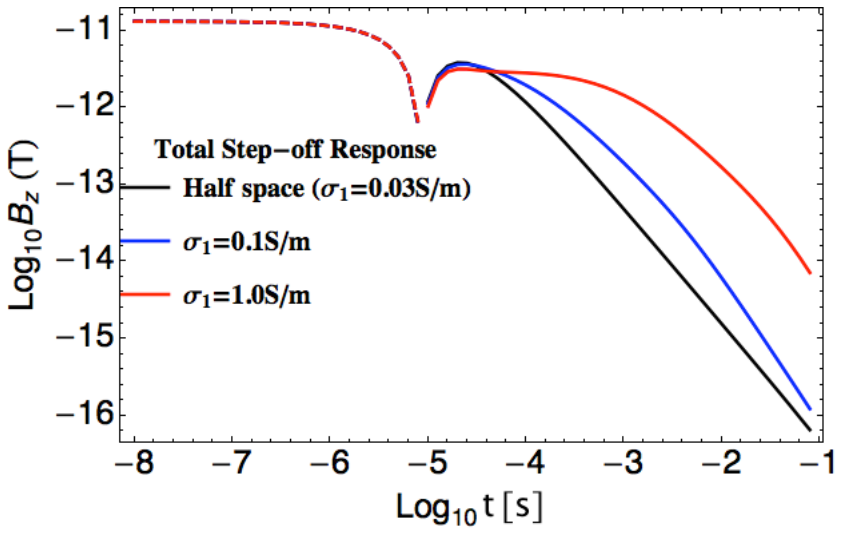

Figure 2.9: The step-off vertical magnetic response of a 3-layer earth model in time domain for different conductive mid layer conductivity. The receiver is fixed at 60m away in x direction. The background conductivity $\sigma_0 = 0.03$ S/m. The conductive layer for the other two models are $\sigma_1 = 0.1$ S/m and $\sigma_1 = 1.0$ S/m respectively. The dashed line denotes a negative response.

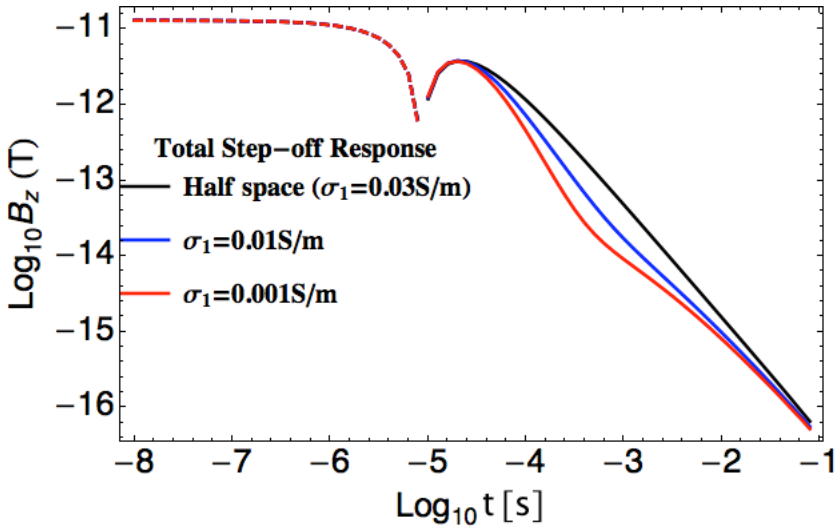

Figure 2.10: The step-off vertical magnetic response of a 3-layer earth model in time domain for different resistive mid layer conductivity. The receiver is fixed at 60 m away in x direction. The background conductivity $\sigma_0 = 0.03$ S/m. The conductive layer for the other two models are $\sigma_1 = 0.01$ S/m and $\sigma_1 = 0.001$ S/m respectively. The dashed line denotes a negative response.

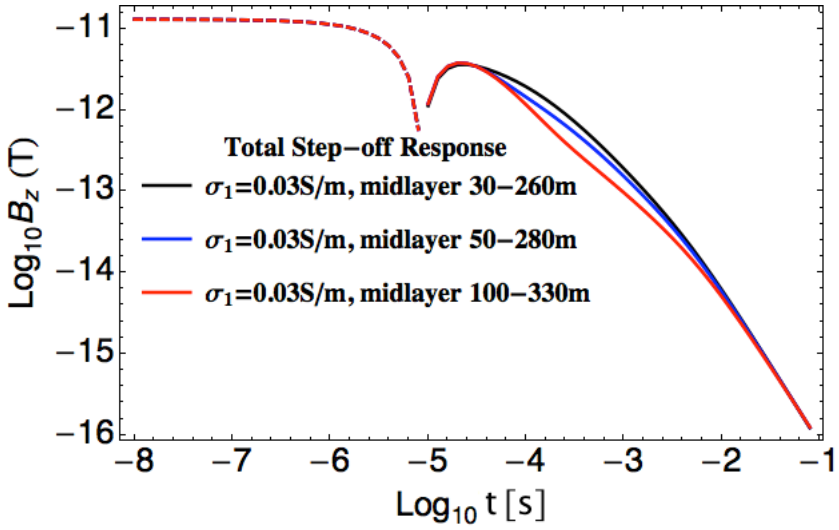

Figure 2.11: The step-off vertical magnetic response of a 3-layer earth model in time domain with different layer depth. The receiver is fixed at 60m away in x direction. The background conductivity $\sigma_0 = 0.03$ S/m. The mid layer conducitivity is $\sigma_1 = 0.1$ S/m. The layer depth for three models are 30-260 m, 50-280 m and 100-330 m. The dashed line denotes a negative response.

netic loop source is derived . The time domain response can be obtained through G-S algorithm based on several frequency domain responses. Secondary magnetic responses of halfspace, resistive-layered and conductive-layered model are compared in frequency and time domain. The classical step-off response of a half-space model follows a $t^{-3/2}$ power-law decay. The difference of responses of conductive targets is more significant than resistive targets. In the next chaper, I introduce fractional diffusion theory and explore how it is associated with the classical CSEM technique explained in this chapter.

3. THE FRACTIONAL DIFFUSION THEORY OF ELECTROMAGNETIC INDUCTION

3.1 Introduction and background review

The classical perspective on transport processes in geological media is mostly concerned with diffusion, which is the automatic movement of a substance from a region of high concentration to a region of low concentration. For example, convective advection is a transport mechanism of a substance embedded in a fluid due to the fluid bulk motion; while hydrodynamic dispersion is the microscopic fluctuation of the substance with respect to the bulk fluid. These transport processes in a homogeneous medium have long been well treated by Fick's law, which gives rise to the deterministic advection-dispersion equation (ADE):

$$\frac{\partial \phi}{\partial t} = D \frac{\partial^2 \phi}{\partial x^2} \tag{3.1}$$

where the ϕ is the concentration of the substance and D is the diffusion constant depdending on the medium's hydraulic properties. Fick's law involves two assumptions that lead to a classical Gaussian transport behavior: first, the medium is homogeneous or at least it can be described by local, averaged macroscale properties; second, the diffusion velocity field is constant, without spatial or temporal dependence. In contrary, a non-Fickian transport phenomenon emerges in many realms, such as charge carrier diffusion in amorphous semiconductors [63]; and solute and heat transport in fractured rocks [8, 27, 28]. Such anomalous transport processes are not fully explained by Fick's law, and are characterized by preferential flow paths [51] and the appearance of "scale-dependent dispersion" [29] for which the measured

conductivity is scale and temporally dependent. Long tails occur in the late time of breakthrough curves (which measures the concentration with respect to time at a fixed point in the medium) [8] (Figure 1.2). The reason for the ADE failing to describe such anomalous diffusion processes owes to the broad scale variation of heterogeneties in the media. The ADE is not able to capture the complete details of the transport property using its local macroscale-averaging approach, especially for scales of heterogeneites that are comparable with the characteristic lengths of the diffusion velocity field.

Natural fractures, such as cracks, fissures, joints and faults with inclusions other than the material of the rock matrix, form a major component of heterogeneties in rocks. The displacement between fracture walls can be either perpendicular to the interface, as in joints, or parallel with the interface, as in faults. The fracture surface is usually irregular and typically possesses self-affine fractal properties described by a fractal dimension, or "roughness" [64, 35]. In addition, many geometric properties of natural fracture networks, such as the length, aperture and density follow a power law scaling distribution, contributing to the roughness of fractures. Due to the fractal geometry of the fracture network, the hydraulic transport within conduits is often anomalous such that is not resolved by the classical ADE. Since the anomalous diffusion velocity is generally slower than the classical diffusion velocity, the transport in scale-dependent geomaterials is also called the subdiffusion [47].

To model anomalous diffusion, existing approaches are mainly based on classical deterministic ADE or a generalized ADE of a stochastic nature. The deterministic ADE involves mapping the realistic fracture network to a discrete computational domain, thus generating a very complicated heterogeneity model [28, 30]. A fracture model can be generated by either the known fracture structure, or a stochastic random media approach, in which the spatial correlation of geometric properties in

the medium is preserved [37, 34]. However, to generate such a complicated model is computationally intensive. The scale of heterogeneities is limited by the support scale of subgrids on which the parameters of the ADE are defined. This often fails to capture anomalous diffusion since the full wavenumber spectrum of the heterogeneties is not resolved. The stochastic approach seeks to generalize the classical ADE to a fractional ADE (fADE) that is nonlocal in space and/or time and is based on a stochastic framework such as the continuous-time random walk (CTRW) approach[7, 47], generalized master equation[36], Lagarangian approach[79], or the particle tracking method based on Langevin equation[66]. Using the CTRW formulation, the property coefficients in the ADE become nonlocal, being convolved with coefficients at other time steps or spatial locations. The model complexity is introduced into the governing equation by means of a fractional integral.

In the following sections, I will introduce the CTRW derivation of fADE, and will review the fundamentals of fractional derivatives. Then I introduce the fractional derivative Maxwell equations.

3.2 The continuous time random walk analysis of fractional diffusion

The CTRW model was initiated by Montroll, Weiss and Scher with their piorneering efforts (e.g. [49, 63, 75]) to explain the anomalous diffusion of charge carriers in amorphous semi-conductors. In their model, the waiting time of a charge carrier undergoing a random walk in a discrete network obeys a power-law probability density distribution. This successfully reproduces the long tailed dispersion in the transient current measurement. The concept of CTRW then became popular in many other physical applications. A thorough description of the theory and some of its applications is given by Metzler et.al. [47].

The CTRW model is versatile to describe a classical diffusion process as well as

a fractional diffusion case. In a simple discrete random walk model, the transport of a substance is analogous to a group of particles undergoing a random walk on a discrete lattice. In 1D, the probability density function (PDF) of a particle to jump to the i^{th} node at time $t + \Delta t$, from adjacent nodes at time t is given by:

$$p_i(t + \Delta t) = \frac{1}{2}p_{i-1}(t) + \frac{1}{2}p_{i+1}(t) \tag{3.2}$$

In the continuum limit $\Delta t \to 0$ and $\Delta x \to 0$, Taylor expansions in Δt and Δx are

$$p_i(t + \Delta t) = p_i(t) + \Delta t\frac{\partial p_i}{\partial t} + O([\Delta t]^2) \tag{3.3}$$

and

$$p_{i\pm1}(t) = p_i \pm \Delta x\frac{\partial p_i}{\partial x} + \frac{\Delta x^2}{2}\frac{\partial^2 p_i}{\partial x^2} + O([\Delta x]^3). \tag{3.4}$$

Combining these equations leads to the classical ADE equation

$$\frac{\partial p}{\partial t} = K_1\frac{\partial^2}{\partial x^2}p(x,t), \tag{3.5}$$

where K_1 is the diffusion constant. The CTRW model is based on the idea that the length of a given jump, as well as the waiting time between two successive jumps, following certain PDFs drawn from a PDF kernel $\psi(x,t)$. The jump length PDF is then

$$\lambda(x) = \int_0^\infty dt\psi(x,t) \tag{3.6}$$

while the waiting time PDF is

$$w(t) = \int_{-\infty}^\infty dx\psi(x,t), \tag{3.7}$$

where $\lambda(x)dx$ describes the probability for a jump length in the interval (x, x+dx) and $w(t)dt$ describes the probability for a waiting time in the interval (t,t+dt) (Figure 3.1). With these definitions, a CTRW process can be described through an appropriate generalized master equation:

$$\eta(x,t) = \int_{\infty}^{\infty} dx' \int_{0}^{\infty} dt' \eta(x',t')\psi(x-x',t-t') + \delta(x)\delta(t) \tag{3.8}$$

which relates the pdf η(x,t) of having just arrived at position x at time t, with the pdf $\eta(x',t')$ of having just arrived at x' at time t', . The term $\delta(x)\delta(t)$ denotes the initial condition of the random walk. Consequently, the PDF p(x,t) of being at position x at time t is given by:

$$p(x,t) = \int_{0}^{t} dt \eta(x,t')[1 - \int_{0}^{t-t'} dt'' w(t'')] \tag{3.9}$$

In Fourier-Laplace space, the PDF p(x,t) obeys the algebraic relation:

$$p(k,s) = \frac{1-w(s)}{s} \frac{p_0(k)}{1-\psi(k,s)} \tag{3.10}$$

where $p_0(k)$ denotes the Fourier transform of the initial condition $p_0(x)$

Given a long-tailed waiting time PDF with the asymptotic behavior:

$$w(t) \sim A_\alpha (1/t)^{1+\alpha} \tag{3.11}$$

for $0 < \alpha < 1$, together with the classical Gaussian jump length PDF, the relation 3.10 in Fourier Laplace domain becomes

$$p(k,s) = \frac{[p_0(k)/s]}{1 + K_\alpha s^{-\alpha} k^2} \tag{3.12}$$

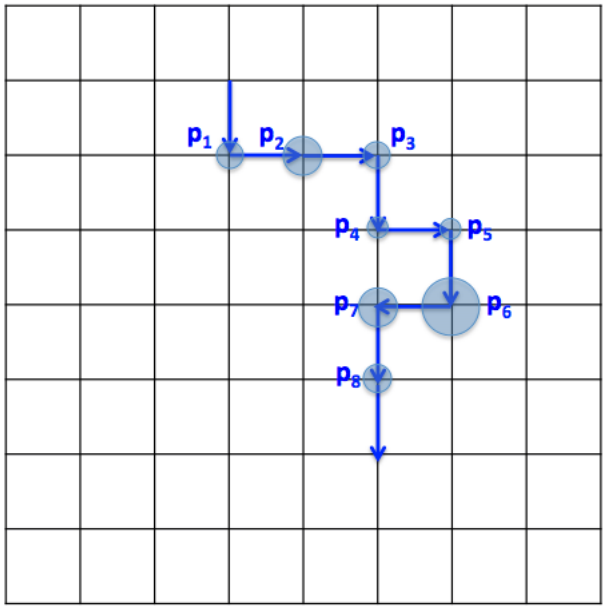

Figure 3.1: CTRW model of a particle on a discrete lattice. The waiting time of each step is symbolized by the area of the circle associated with each node. Repeated from [47]

in the $(k, s) \to (0, 0)$ classical diffusion limit. Employing the Laplace transform for fractional integrals [54],

$$\mathcal{L}\{{}_0D_t^{-\alpha}p(x,t)\} = s^{-\alpha}p(x,s) \tag{3.13}$$

one infers the fractional integral equation

$$p(x,t) - p_0 =_0 D_t^{-\alpha}K_\alpha\frac{\partial^2}{\partial x^2}p(x,t) \tag{3.14}$$

from relation 3.12. By application of the differential operator $\partial/\partial t$, one finally arrives at the fADE

$$\frac{\partial p}{\partial t} =_0 D_t^{1-\alpha}K_\alpha\frac{\partial^2}{\partial x^2}p(x,t) \tag{3.15}$$

where ${}_0D_t^{-\alpha}$ is the fractional derivative operator, whose defintion will be given in the next section.

3.3 The definition and some properties of the fractional derivative

The concept of differentiation and integration of noninteger order dates back to the 18th century by Leibniz and L'Hopital, who discussed the meaning of a derivative of order one half. Since then, many famous mathematicians have worked on this and related questions, developing the field which has become known as fractional calculus. A list of mathematicians who have provided important contributions up to the middle of last century includes Laplace, Fourier, Abel, Liouville, Riemann, Grunwald, Letnikov, Levy, Marchaud, Erdelyi, and Riesz. Nowadays, the books by Oldham and Spanier [54] and Podlubny [58] are popular ones that provide good tutorials on fractional differentiation.

There are two major approaches for defining a fractional derivative. The first considers differentiation and integration as limits of finite difference. This concept used the Gunwald-Letnikov definition. Specifically, it is first shown that differentiation of integer order is [54]

$$\frac{d^n f(x)}{dx^n} = \lim_{h\to 0} \frac{1}{h^n} \sum_{k=0}^{n} (-1)^k \binom{n}{k} f(x-hk) \tag{3.16}$$

while integration is

$$\frac{d^{-n} f}{[d(x-a)]^{-n}} = \lim_{N\to\infty} \{[\frac{x-a}{N}]^n \sum_{j=0}^{N-1} \binom{j+n-1}{j} f(x-j[\frac{x-a}{N}])\} \tag{3.17}$$

Combining and extending these two relations generates the definition of the qth order

"differintegrals":

$$\frac{d^{-q}f}{[d(x-a)]^{-q}} = \lim_{N\to\infty}\{\frac{[\frac{x-a}{N}]^{-q}}{\Gamma(-q)}\sum_{j=0}^{N-1}\frac{\Gamma(j-q)}{\Gamma(j+1)}f(x-j[\frac{x-a}{N}])\} \tag{3.18}$$

Another approach to fractional differentiation is based on Cauchy's formula for repeated integration:

$$\frac{d^{-n}f}{[d(x-a)]^{-n}} = \frac{1}{(n-1)!}\int_a^x [x-y]^{n-1}f(y)dy \tag{3.19}$$

The Riemann-Liouville definition is expressed as a convolution integral:

$${}_aD^q f(x) := \frac{1}{\Gamma(-q)}\int_a^x \frac{f(t)}{(x-t)^{q+1}}dt, \quad q<0 \tag{3.20}$$

using the gamma function to generalize the factorial function. This integral diverges when $q > 0$. To avoid this and extend the definition to $q > 0$, the convention is to shift the order by an integer, and then undo this operation by differentiation, such that, for $q > 0$, choose integer $n > q$:

$${}_aD^q f(x) := \frac{d^n}{dx^n}\frac{1}{\Gamma(n-q)}\int_a^x \frac{f(t)}{(x-t)^{q+1-n}}dt, \quad n-1\le q<n \tag{3.21}$$

Meanwhile, M. Caputo gave another definition for the fractional derivative, in his 1967 paper [10]:

$${}_a\bar{D}^q f(t) := \begin{cases} \frac{1}{\Gamma(-q)}\int_a^x \frac{f(t)}{(x-t)^{q+1}}dt, & q<0 \\ \frac{1}{\Gamma(n-q)}\int_a^x \frac{f^{(n)}(t)}{(x-t)^{q+1-n}}dt, & n-1\le q<n \end{cases} \tag{3.22}$$

in which, the definition for the $q < 0$ regime is the same as the R-L definition, but for the $q > 0$ regime, the differentiation to the order n is firstly conducted then is the

convolution integral. Due to such definition, there are some distinguishing property of the Caputo definition, which makes it attractive:

Firstly the R-L operator on a constant is not zero, which is not consistent with the integer differintegrals:

$$ {}_aD^{-q}C = C\frac{(x-a)^q}{\Gamma(q+1)}, \quad q > 0 \tag{3.23} $$

and

$$ {}_aD^{q}C = \frac{d^n}{dx^n}C\frac{(x-a)^{n-q}}{\Gamma(n-q+1)} = \frac{d^n}{dx^n}C\frac{(x-a)^{-q}}{\Gamma(q+1)}, \quad q > 0 \tag{3.24} $$

For integer $q > 0$, we get $\Gamma(1+q) = \pm\infty$, so the derivative is zero as expected. While for the Caputo derivative, ${}_a\bar{D}^q$ is always zero for real positive q.

Secondly, the Laplace transform of R-L derivative and Caputo derivative have different properties. Recall the Laplace transform:

$$ \mathcal{L}\{f(t)\} = \int_0^\infty f(t)e^{-st}dt = \bar{f}(s) \tag{3.25} $$

Let $q > 0$, for the R-L derivative, we have:

$$ \mathcal{L}\{{}_aD^q f(t)\} = s^q\bar{f}(s) - \sum_{k=0}^{n-1} s_0^k D^{q-k-1}f(0), \tag{3.26} $$

when $n-1 < q \leq n$ and for the Caputo definition:

$$ \mathcal{L}\{{}_a\bar{D}^q f(t)\} = s^q\bar{f}(s) - \sum_{k=0}^{n-1} s_0^{q-k-1} D^k f(0), \tag{3.27} $$

The difference in the two transform results is the second term in the right hand side, denoting the initial condition for system is associated with a fractional derivative for

the R-L definition while an integer derivative for the Caputo definition. The initial condition for the R-L derivative is difficult to explain in terms of its physical meaning while the Caputo derivative seems easier and more straightforward to explain. Nowadays, people still have debate on the utility of either definition, who find the Caputo derivative has some inconsistency with the classical integer derivative [41]. People also try to find a physical interpretation for the initial conditions with R-L fractional derivatives [33].

In this work, I choose to use the R-L definition of the fractional derivative.

3.4 The connection between CTRW approach with EM fractional diffusion

The CSEM technique analyzes the subsurface diffusion of electromagnetic eddy currents at sufficiently low frequencies ($\sigma \gg \omega\epsilon$) such that displacement currents can be neglected. The induced eddy currents are mainly constituted by the migration of ions such as Na^+ and Cl^- in the pore fluid electrolyte. Thus the bulk geoelectrical conductivity of a naturally fractured subsurface is likely to have a similar fractal geometry as the fracture system itself. Moreover, the pathways of electrical charges are spatially correlated with those of hydraulic flow [12]. The anomalous charge transport is thus considered to be analogous to the aforementioned hydrodynamic case. The fractional diffusion of EM eddy currents in fractured geological media is reported by [23, 73]. They found the measured zero crossing time in a transient loop-loop system exhibits a nonlinear dependent relationship with a fractional power of source-receiver offset, denoting a subdiffusive process. Everett [19] derived the fractional differential Maxwell equation by writing the Ohm's law in its the convolution integral form, which naturally introduces the R-L derivative.

Here is a brief introduction to the derivation. The Ohm's law is written in its

time-convolutional form:

$$\mathbf{J} = \sigma_\beta * \mathbf{E} \equiv \int_0^t \frac{dt' \sigma_\beta \mathbf{E}(t')}{(t-t')^{1-\beta}} \tag{3.28}$$

where σ_β is a generalized electrical conductivity. Relation 3.28 can be derived from the CTRW approach by considering of a charge carrier under going a random walk in a fractal geoelectrical network, supposing a power law pdf $t^{1-\beta}$ of the waiting time. The model heterogeneity is introduced through the convolution integral and the charge transport process becomes nonlocal. Neglecting the displacement current, Ampere's law becomes:

$$\nabla \times \mathbf{B} = \mu_0 \sigma_\beta * \mathbf{E} + \mu_0 \mathbf{J}_s(t) \tag{3.29}$$

where $\mathbf{J}_s(t)$ denotes a source term. By combining Equation 3.29 with Faraday's law:

$$\nabla \times \mathbf{E} = -\frac{\partial \mathbf{B}}{\partial t} \tag{3.30}$$

The magnetic field $\mathbf{B}$ can be eliminated, leading to a convolutional vector diffusion equation for the electric field $\mathbf{E}$:

$$\nabla \times \nabla \times \mathbf{E} = -\mu_0 \frac{\partial}{\partial t}[\sigma_\beta * \mathbf{E} + \mathbf{J}_s] \tag{3.31}$$

Note that the first term in the right hand side of Equation 3.31 is identical with the R-L operator:

$$\frac{\partial}{\partial t}\sigma_\beta * \mathbf{E} = \frac{\sigma_\beta}{\Gamma(\beta)}\frac{\partial}{\partial t}\int_0^t \frac{dt' \mathbf{E}(t')}{(t-t')^{1-\beta}} \equiv \sigma_{\beta 0} D_t^{1-\beta}\mathbf{E}(t). \tag{3.32}$$

The generalized conductivity σ_β has dimensions of $[\sigma]s^{-\beta}$, where the usual dimensions of conductivity σ in SI units are $[\sigma]$=AV^{-1}m^{-1}=A^{2}s^{3}kg^{-1}m^{-3}. Accordingly we can write $\sigma_\beta \sim \sigma t^{-\beta}$, which is associated with a temporal evolution, that corresponds to the anomalous diffusion. The parameter β determines the waiting time distribution in the CTRW model, and is correlated to the model roughness. The limiting case $\beta = 0$ leads Equation 3.31 to the classical Maxwell equation, if one refers to Cauchy's formula for repeated integration (3.19). As $\beta \to 1$, Equation 3.31 describes a diffusion process that is highly anomalous and takes place in a very rough medium. Consequently, the introduction of generalized Ohm's law generates an anomalous EM induction in a geologically rough medium.

We can write Equation 3.31 in a compact form:

$$\nabla \times \nabla \times \mathbf{E} = -\mu_0 \sigma_{\beta 0} D_t^{1-\beta} \mathbf{E}(t) - \mu_0 \frac{\partial}{\partial t} \mathbf{J_s}. \tag{3.33}$$

Equation 3.33 is normally difficult to solve directly in the time domain. It proves more convenient to transform Equation 3.33 into Laplace domain, using:

$$\mathcal{L}\{{}_aD^q f(t)\} = s^q \bar{f}(s) - \sum_{k=0}^{n-1} s_0^k D^{q-k-1} f(0). \tag{3.34}$$

Assuming a zero initial condition for the step-off case, the Laplace transform of Equation 3.33 becomes

$$\nabla \times \nabla \times \mathbf{e} = -\mu_0 \sigma_0 s^{1-\beta} \mathbf{e}(s) - \mu_0 s \mathbf{j}_s(s), \tag{3.35}$$

where $\mathbf{e}(s)$ is the Laplace transformed electrical field $\mathbf{E}(t)$. Equation 3.35 is similar to the classical Maxwell equation except that s is replaced by $s^{1-\beta}$. In the following section, I will present the EM response of a layered rough earth by solving Equation

3.35.

3.5 The fractional diffusion response of a loop transmitter over a layered earth

To consider the loop TX response of a layered earth, note that the circular loop source has only an azimuthal component:

$$\mathbf{J}_D(t) = \frac{Ia}{\rho}\delta(\rho - a)\delta(z)\delta(t)\hat{\phi} \tag{3.36}$$

where I is the current and a is the radius of the loop. The delta function $\delta(t)$ denotes a transient impulse. It is straightforward to insert expression 3.36 to Equation 3.35 and solve it using a similar technique described in Appendix A. The azimuthal component of the electric field over a layered earth is:

$$e_\phi(s) = \frac{-\mu_0 sIa}{2}\int_0^\infty (e^{-\gamma_0(z+h)} + r_{TE}e^{\gamma_0(z-h)})\frac{\lambda}{\gamma_0}J_1(\lambda a)J_1(\lambda\rho)d\lambda \tag{3.37}$$

where $\gamma_0^2 = \lambda^2 + s^{1-\beta}\mu_0\sigma_0$ and the reflection coefficient r_{TE} is calculated using the recursive relation 2.15. Similarly, the radial and vertical components of the magnetic fields are:

$$b_\rho(s) = \frac{\mu_0 Ia}{2}\int_0^\infty (e^{-\gamma_0(z+h)} - r_{TE}e^{\gamma_0(z-h)})\lambda J_1(\lambda a)J_1(\lambda\rho)d\lambda \tag{3.38}$$

and

$$b_z(s) = \frac{\mu_0 Ia}{2}\int_0^\infty (e^{-\gamma_0(z+h)} + r_{TE}e^{\gamma_0(z-h)})\frac{\lambda^2}{\gamma_0}J_1(\lambda a)J_0(\lambda\rho)d\lambda \tag{3.39}$$

The above solutions are formulated in the Laplace domain and can be converted to the time domain using the G-S algorithm modified to treat step-off excitation. Everett [19] and Decker and Everett [14] previously found the anomalous EM response

of a layered earth. Here I reproduce some of the critical results to illustrate the distinguishing characteristics of the EM anomalous response compared to its classical counterpart.

Figure 3.2 shows a comparison between the classical and anomalous vertical magnetic responses of a halfspace model. The roughness of the lower space in the anomalous case is $\beta = 1/5$, $1/3$ and $1/2$ respectively. As per the configuration in Chapter 2, the RX is located 60 m from the TX in the x direction. The subsurface conductivity is 0.03 S/m for all models. As mentioned in Chapter 2, for the halfspace model, the classical late time step-off response decays following a $t^{-3/2}$ power-law, which is not affected by the TX-RX seperation or the subsurface conductivity. Here, as the result shows, the decay rate follows power law functions with different exponents as the roughness β changes. The slope of the asymptotic line changes as 39.8°, 33.7°, 26.5° in correspondence with $\beta = 1/5$, $\beta = 1/3$, $\beta = 1/2$ respectively. The late-time slope is a critical parameter to distinguish subsurface structures with different roughness. Everett [19] mentioned that for the emf response, which classically follows the $t^{-5/2}$ decay rate, the exponent of the decay function $\gamma \sim \beta - 2$ roughly holds for $\beta > 1/4$.

Another observation is the migration of the zero crossing time T_0 migrate to earlier time as β increases. The diffusion velocity for EM induction is inversely proportional to the conductivity. The roughness β behaves similarly as the apparent conductivity of the subsurface decreases, i.e. it becomes more resistive.

Figure 3.3 shows the vertical magnetic response of a three layered model with a rough layer in the middle. The roughness of the layer varies from 0 (classical) to 0.2 and 0.4. The late time responses (after 10^{-5} s) show significant differences for different rough mid-layers. The curve bends inward, just as the classical resistive response behaves.

Figures 3.4 and 3.5 show the vertical magnetic response of a three layered model

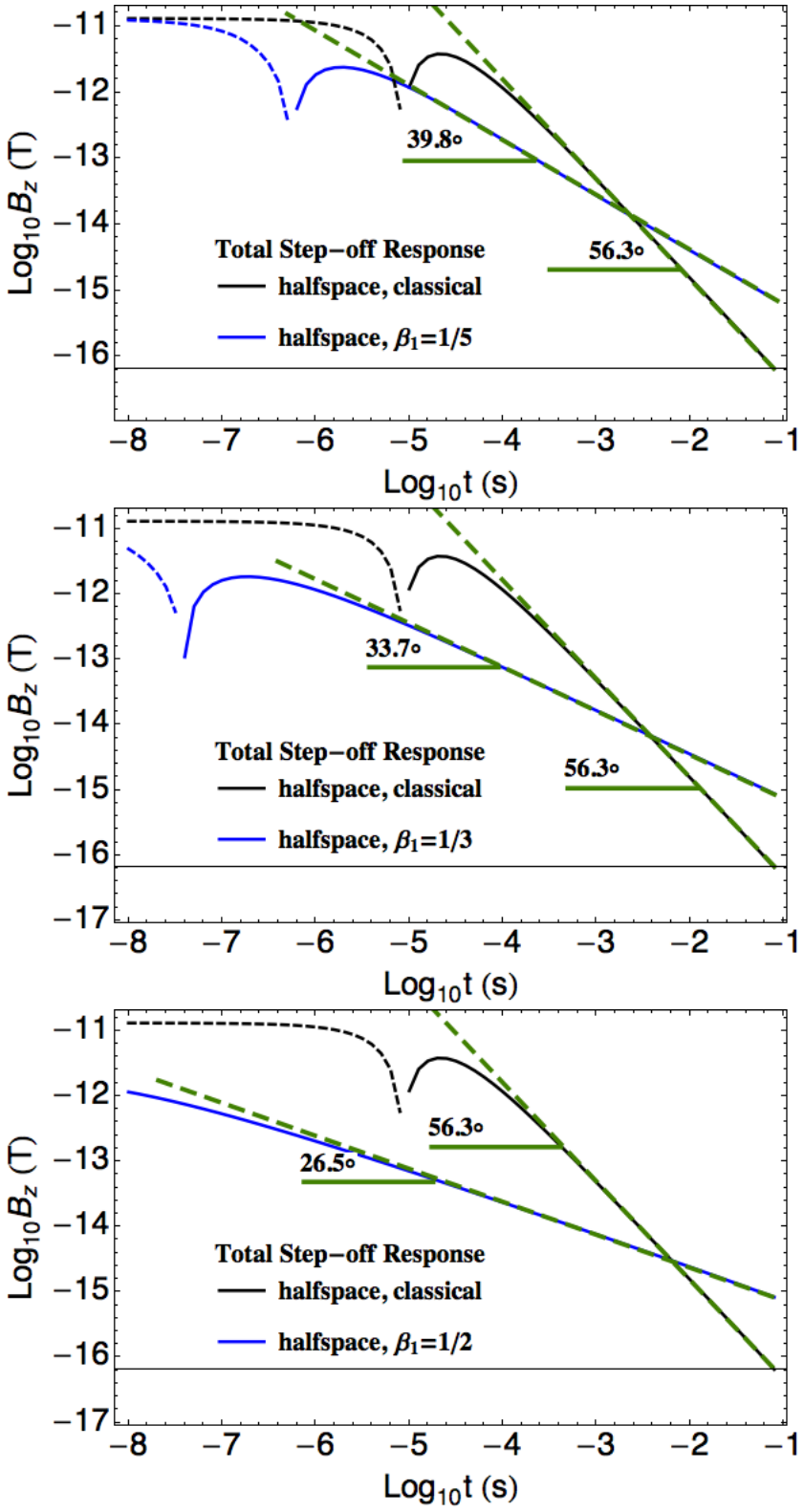

Figure 3.2: The vertical magnetic response over a halfspace earth in classical and anomalous cases. The roughness of the lower space is (A)$\beta_1 = 1/5$ (B)$\beta_1 = 1/3$ (C)$\beta_1 = 1/2$

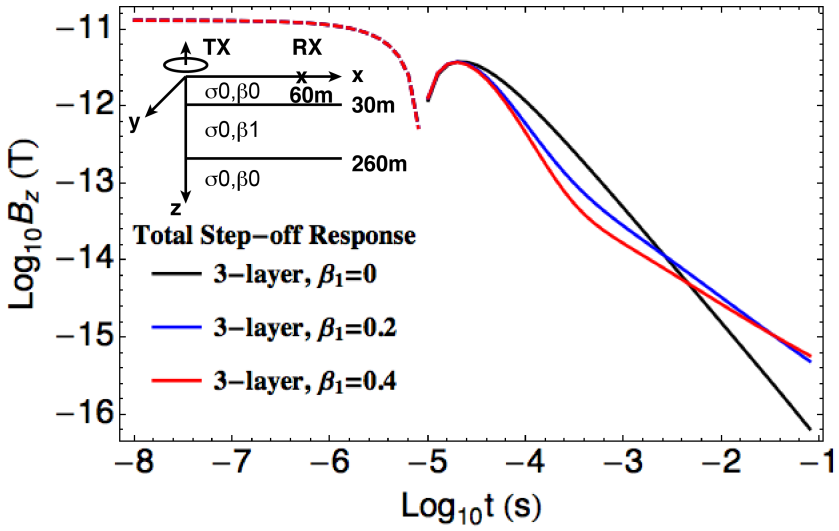

Figure 3.3: The vertical magnetic response over a 3-layer earth with different roughness for the midlayer. The conductivity for the subsurface is $\sigma_0 = 0.03$ S/m.

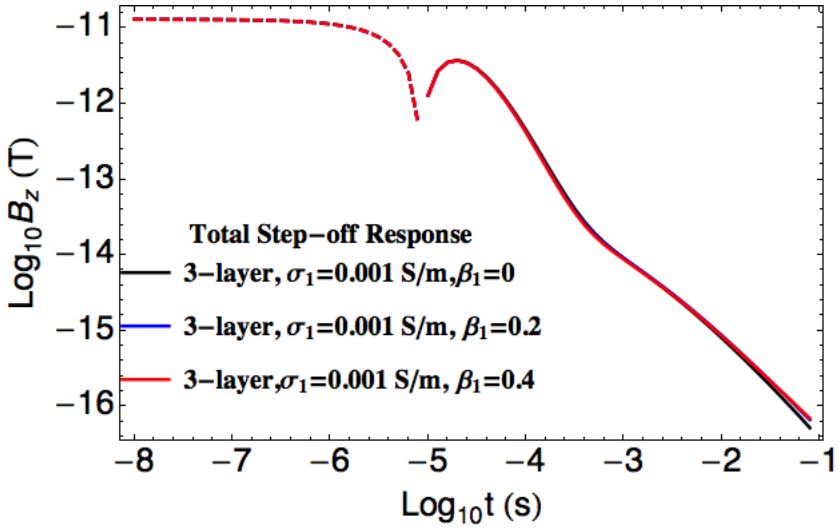

Figure 3.4: The vertical magnetic response over a 3-layer earth with different roughness for the resistive midlayer. The conductivity for the background is $\sigma_0 = 0.03$ S/m and for the midlayer is $\sigma_1 = 0.001$ S/m.

with a rough resistive/conductive layer in the middle. As an EM induction survey is known to be insensitive to a resistive target, the response curves in Figure 3.5 are similar for different roughness values. However for the conductive layer response, the difference of the roughness is reflected very well in the responses (see Figure 3.4).

3.6 Conclusion

In this chapter, I reviewed the physical reasoning of the anomalous diffusion to emerge and its significance. The classical ADE fails to capture the full details of the model heterogeneity since it is a local analysis. The CTRW approach convolves the model complexity with the governing equations explicitly which makes it successfully describes an anomalous diffusion phenomenon. Using fractional calculus as the fundamental theory, provides strong support to the CTRW approach. I choose the R-L definition of the fractional derivative to generalize the Maxwell equation. Finally I showed the comparisons between classical and anomalous responses of a layered earth. The transient time domain measurement can distinguish the difference between two responses very well.

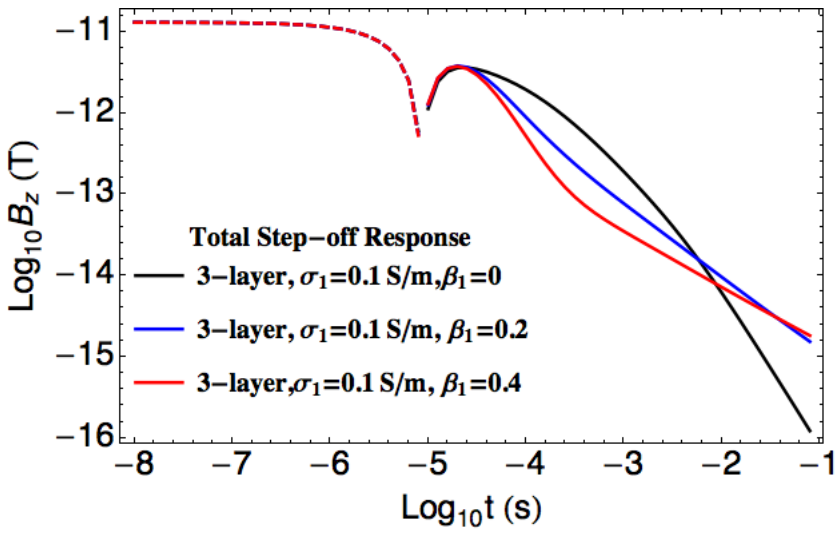

Figure 3.5: The vertical magnetic response over a 3-layer earth with different roughness for the conductive midlayer. The conductivity for the background is $\sigma_0 = 0.03$ S/m and for the midlayer is $\sigma_1 = 0.1$ S/m.

4. FRACTIONAL DIFFUSION ANALYSIS OF THE ELECTROMAGNETIC FIELD IN FRACTURED MEDIA PART I: 2-D APPROACH*

4.1 Introduction

Since the anomalous diffusion of charges in amorphous semiconductors was first described by [61, 62], many additional studies have reported evidence of this process, such as the transport of solutes in fractured geological formations [7]. The presence of fractures provides a confined geometry for hydraulic transport, but also introduces multi-scale variations to the permeability field, resulting in anomalous diffusion that can not be easily reconciled with classical fluid transport models. At a microscopic level, diffusion is generated by the random motion of individual particles, and is traditionally described as a stochastic Gaussian process. However, in anomalous diffusion, the mean square variance of the particle displacement grows faster (superdiffusion) or slower (subdiffusion) than that of a Gaussian diffusion process. Here, we mainly focus on the subdiffusion of EM eddy currents, which would happen in fractured formations. A typical signature of the anomalous diffusion is a long tail in the concentration-time curve. The continuous time random walk (CTRW) theory [63] is able to account for this process. In CTRW theory, a transport process is modeled by the hopping of particles from node to node within a connected network. A key aspect is the specification of a continuous distribution of particle waiting time at each node. If the waiting time distribution does not have long tails but is Gaussian-like, the CTRW would model the classical diffusion. However, fractional or anomalous diffusion is modeled if a long tail waiting time distribution function is

*Reprinted with permission from "Fractional diffusion analysis of the electromagnetic field in fractured media part I: 2-D approach" by J. Ge, M. E. Everett and C. J. Weiss, 2012, *Geophysics*, 77(4), WB213-WB218, DOI: http://dx.doi.org/10.1190/geo2012-0072.1, Copyright [2012] by Society of Exploration Geophysicists.

chosen, such as $t^{-(1+\alpha)}$, where $0 < \alpha < 1$.

The spatial distribution of induced electrical current in geological formations is also controlled in part by the presence of connected fractures. Although electrical current and fluid flow paths are spatially correlated, it is well known that EM data cannot resolve details of individual hydraulic paths. Weiss and Everett [73] found evidence for the fractional diffusion of EM eddy currents in a floodplain setting using time-domain electromagnetic (TDEM) data. In their work, they define a spatially uniform roughness parameter β to characterize the complexity of the geoelectrical structure. The β parameter, ranging from 0 to 1, is hypothesized to be related to the subsurface fracture density; the precise relationship is yet to be determined by additional field studies.

As described above, anomalous diffusion is strongly associated with spatial variations of material properties. These may be generated, for example, by the presence of fractures. In this work, the value $\beta = 0$ corresponds to classical diffusion in a homogeneous medium while β approaching 1 corresponds to subdiffusion. Although the EM response of geological media is a complicated function of grain/fluid interactions and pore-scale electrochemistry, the spatial hierarchy of fractured systems also strongly influences the geometry of electric current pathways, just as it does the geometry of fluid pathways. The application of fractional calculus to geoelectromagnetic induction, as done here, is an empirically driven attempt to describe the effects of fractured media on Maxwell's equations. Everett [19] solved the Maxwell equations in a rough medium generated by a loop source, and investigated the behavior of the solution in the time domain. In the present study, we extend this work by considering 2-D idealized geologic systems. We introduce a strike direction along which the geoelectrical structure is invariant.

Herein, we develop a new 2D FD algorithm in the frequency domain to model

fractional diffusion of EM eddy currents generated by a line source. We start by comparing the FD solution with the analytical solution to a rough half space model. Then we introduce a subsurface fracture zone, modeled with uniform conductivity and roughness β, buried in a classical background medium. We show that using synthetic data that the target roughness is detectable. We explore the sensitivity of 2D EM responses to subsurface. It is assumed, but not explicitly shown here, that the roughness parameter β is a useful proxy for fracture density. As mentioned above, further experimental studies are needed to rigorously evaluate this assumption. In a companion paper (part II: 2.5D approach), a more realistic 2.5D problem configuration with the 2D structure geometry and 3D source will be investigated in the time domain using staggered FD algorithm to provide more comparable data for experimental studies.

4.2 Theoretical background

Weiss and Everett [73] derived the EM fractional diffusion governing equations starting from the conventional Maxwells equations. They incorporate the time-convolution form of Ohm's law within Ampere's law:

$$\nabla \times \mathbf{B} = \mu_0 \sigma_\beta * \mathbf{E} + \mu_0 \mathbf{J}_s(t) \tag{4.1}$$

namely,

$$\sigma_\beta * \mathbf{E} \equiv \int_0^t \frac{dt' \sigma_\beta \mathbf{E}(t')}{(t-t')^{1-\beta}} \tag{4.2}$$

Here, σ_β is a generalized electrical conductivity and μ_0 is the free space magnetic permeability, which is set to $4\pi \times 10^{-7}$ H/m. It can be shown that under general conditions, the Form 4.2 which involves $(t-t')^{1=\beta}$ describes subdiffusion [47]. The line source current density is described by $\mathbf{J}_s(t)$. The time derivative of Equation 4.2

is identical with the fractional derivative or Riemann-Louiville (R-L) operator [54]:

$$\frac{\partial}{\partial t}\sigma_\beta * \mathbf{E} = \frac{\sigma_\beta}{\Gamma(\beta)}\frac{\partial}{\partial t}\int_0^t \frac{dt'\mathbf{E}(t')}{(t-t')^{1-\beta}} \equiv \sigma_{\beta 0} D_t^{1-\beta}\mathbf{E}(t) \tag{4.3}$$

where Γ is the Gamma function serving as a normalizing constant. The R-L definition of a fractional order derivative is the fundamental governing operator of a fractional transport process and is a direct result from CTRW theory [47]. Combining Equations 4.1 to 4.3 with Faraday's law, following Everett [19] we can eliminate **B** field and obtain a fractional differential equation for the **E** field:

$$\nabla \times \nabla \times \mathbf{E} = -\mu_0 \sigma_{\beta 0} D_t^{1-\beta}\mathbf{E}(t) - \mu_0 \frac{\partial}{\partial t}\mathbf{J_s} \tag{4.4}$$

The laplace transform of Equation 4.4 is

$$\nabla \times \nabla \times \mathbf{e} = -\mu_0 \sigma_0 s^{1-\beta}\mathbf{e}(s) - \mu_0 s\mathbf{j}_s(s), \tag{4.5}$$

where **e** is denoted as the Laplace transform of **E** and s is the Laplace variable. In the following computation we should assume the frequency $f = s/2\pi i$. However, though generally s is a complex number, we only take s as a pure real number for the need of of Gaver-Stehfest algorithm when transforming the solution back to the time domain in the future work. Following this assumption, we simply adopt $f = s/2\pi$, with no harm to the original setting. Herein we solve Equation 4.5 numerically in two dimensions. In our computations, we first construct a 2D grid in the $x-z$ plane. A line source of strength I lies in the $\hat{y}$ direction and is perpendicular to the plane, yielding

$$\mathbf{J}_s(x,z) = I\delta(x)\delta(z)\hat{y} \tag{4.6}$$

Since the electrical conductivity σ varies only as a function of x and z, the source term $\mathbf{J}_s$ in Equation 4.6 generates only a single component of electric field $\mathbf{E} = E_y\hat{y}$ throughout the model domain. Consequently there is no charge buildup present that distorts the electric field so that the vector components in the $\hat{x}$ or $\hat{z}$ directions vanish. Hence, for both anomalous and classical diffusion, there is only one non-vanishing component of the induced electric field, namely $E_y(x, z)$, along with two magnetic field components, B_x and B_z. The resulting 2D partial differential equation in the Laplace domain is,

$$\frac{\partial^2 e_y}{\partial x^2} + \frac{\partial^2 e_y}{\partial z^2} - \mu_0 \sigma s^{1-\beta} e_y = \mu_0 s J_s \tag{4.7}$$

Equation 4.7 is then solved by the FD method described in the following section.

4.3 Code development

The computational domain consists of a 2D Cartesian grid, whose inner region is uniform and outside region on all four sides is padded by a non-uniform grid to push the boundary far away from the source. The fractional Helmholtz Equation 4.7 is discretized on the grid using a standard 5-point stencil while the field ey is evaluated at each node of the grid. The material properties, namely the conductivity and roughness β, at each node are approximated by a weighted sum of the properties of the neighboring cells. The contribution of each cell is weighted by their area. As in the third term of the left hand side of Equation 4.7, the roughness β presents in the exponent of s and their product with the conductivity forms the whole term, we choose to apply the averaging scheme on the product of them, that is "$\sigma s^{1-\beta}$", instead of on them separately. It turns out this scheme works well as we discuss in the next section. No additional errors are introduced. A thorough derivation of the discretization scheme is published in [55]. And a detailed FD representation of Equation 4.7 is presented in the Appendix B.

A Dirichlet condition is applied at the grid boundaries. Specifically, we set the boundary values of ey as the primary fields for the background halfspace model. The primary-field solution for the halfspace model can be valued analytically [71] as discussed below. The boundary conditions for the 2D fault zone model are more complicated, as we show below, since they vary according to location.

To address the singularity in the source term of Equation 4.6, we use a hat or tent function to represent the delta function,

$$\delta(x) = \begin{cases} \frac{(l-|x|)}{l^2} & |x| < l \\ 0 & |x| \geq l \end{cases} \tag{4.8}$$

where $|x|$ is the distance of the node to the source location and l is the distance between neighboring nodes. The hat function is discretized on the nodes around the source location ([40], Equation 1.3). If the transmitter is deployed at a particular node in the grid, then Equation 4.8 is simplified as

$$\delta(z_j, x_j) = \begin{cases} 1 & i = p \& j = q \\ 0 & others \end{cases} \tag{4.9}$$

where the location of the transmitter is at the node (z_p, x_q). After discretization using the standard 5-point stencil, Equation 4.7 is assembled into a system of linear equations

$$\mathbf{ME} = \mathbf{s}, \tag{4.10}$$

where in a mesh of $N_x \times N_z$ cells $\mathbf{E}$ is the unknown vector of dimension $N_x N_z$ representing ey on all nodes, the vector $\mathbf{s}$ describes the source term and the boundary conditions, while $\mathbf{M}$ is the coefficient matrix of size $(N_x N_z)^2$. The matrix $\mathbf{M}$ is sparse and symmetric, and could be either solved by iterative solvers or direct solvers. The

iterative solvers, such as the well-known conjugate gradient (CG) method [32], and the quasi-minimum residual (QMR) technique [24], are very prevalent in 3D EM modeling algorithms [3, 52, 74]. They require relatively little memory storage and are faster if a single source configuration problem is considered. However, if the equation system is ill-conditioned, the iterative solvers would encounter divergence problems and need particular preconditioners to be associated. This is especially common for 3D EM modeling, when the frequency is lower to the static limit [65, 53, 74]. Nevertheless if the problem size is well manageable, a direct solver is appropriate for choice, which is more stable and could avoid slow or non-converging problem at low frequency EM modeling algorithms. In this paper, the MUMPS direct solver[1] is chosen to solve the Equation 4.10. It performs a direct LU factorization on the system. We implemented the code using the PETSc (Portable, Extensible Toolkit for Scientific Computation) open source package [4, 5]. PETSc contains a comprehensive suite of parallel linear and nonlinear equation solvers. PETSc solvers utilize a compressed sparse storage format in which only the non-zero elements of the matrix and their locations are stored, hence significantly reducing the memory requirement. PETSc also has a well-designed parallel computing interface based on the Message Passing Interface (MPI) standard, such that parallelization is realized through the entire computation including initializing and solving the equation systems.

4.4 Verification of the algorithm

The previous discussion has described the theoretical development of the fractional EM diffusion equation, and outlined the 2D FD code implementation. In this section we illustrate the performance and accuracy of the algorithm by checking against a half space model. In the next section, we present modeling results for more complicated subsurface geometries.

In Figure 4.1 is shown the layout of the 2D half space model. The inner computational domain discretized by the uniform grid is of dimension $930 \times 930\text{m}^2$ and contains 156×156 nodes, so that the node spacing is 6 m. Each side of the inner grid is padded with 25 non-uniform nodes, characterized by a doubling of the node spacing every 5 nodes. Thus, the outergrid node spacing varies as 12, 24, 48, 96 and 192 m. The line source transmitter of 1 kHz is located at the origin of the $x - z$ plane, lying on the interface between the air and subsurface, and oriented parallel to strike.

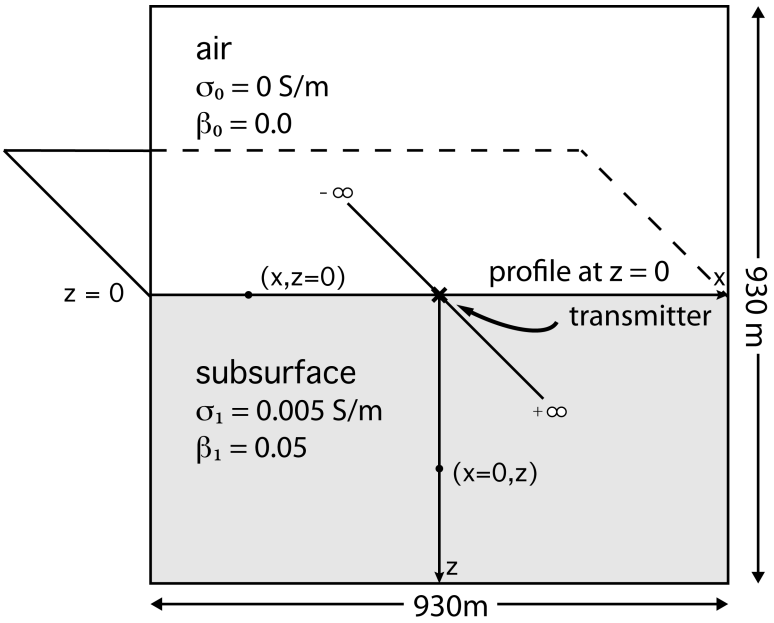

Figure 4.1: Schematic drawing of the half space model. The upper half of the plane consists of air, whose conductivity and roughness β are zero. The subsurface part has conductivity of 0.005 S/m and $\beta = 0.05$, which models a highly fractured and conductive formation.

An array of receivers is situated right at the interface between the air and subsur-

face, with spacing 6 m. The vertical direction is positive downward. The conductivity and roughness of the air are zero. The subsurface conductivity is 0.005 S/m and its roughness β is 0.05. These values model a fractured formation characterized by spatially hierarchical diffusion of the EM eddy currents. The analytical solutions for the total field ey are expressed as cosine transforms [71]:

$$\begin{aligned} e_y^{upper}(s) &= -\frac{\mu_0 sI}{\pi}\int_0^\infty \frac{e^{-u_0 z}}{u_0+u_1}cos(\lambda x)d\lambda, \quad z>0 \\ e_y^{lower}(s) &= -\frac{\mu_0 sI}{\pi}\int_0^\infty \frac{e^{-u_1 z}}{u_0+u_1}cos(\lambda x)d\lambda, \quad z<0 \end{aligned} \tag{4.11}$$

here, $u_0^2 = {}^2 + s^{1\beta_0}\mu_0\sigma_0$, and $u_1^2 = {}^2 + s^{1\beta_1}\mu_0\sigma_1$. The subscripts 0 and 1 denote the upper space and lower space respectively. Note that the Laplace variable s is raised to the fractional power 1β. We calculate the value of e_y at the boundary nodes using Equation 4.11 in order to realize the Dirichlet boundary condition.

In Figure 4.2A, we compare the FD and analytical solution for the total field ey of the half space model at the receiver locations for $x > 0$. The magnitude of ey field is greater around the location of the transmitter, and decays with distance from the center, as expected. The comparison is excellent even at the node close to the interface, with $\sim 1\%$ error. The error is largest at the location closest to the transmitter, and could be improved with a finer grid. At regions far from the source, an empirical rule is to mesh at least 10 nodes per skindepth. Using this rule, we need not be concerned about large errors at the nodes near the source, since we henceforth model the secondary field, with which the singularity at the source location is removed and the field is smoother than the total field.

In order to assess our averaging scheme on the term "$\sigma s^{1-\beta}$", here we provide the FD result in Figure 4.2B for a reference homogeneous model, with the conductivity for the whole space being 0.005 S/m and roughness 0. In this model, there is no

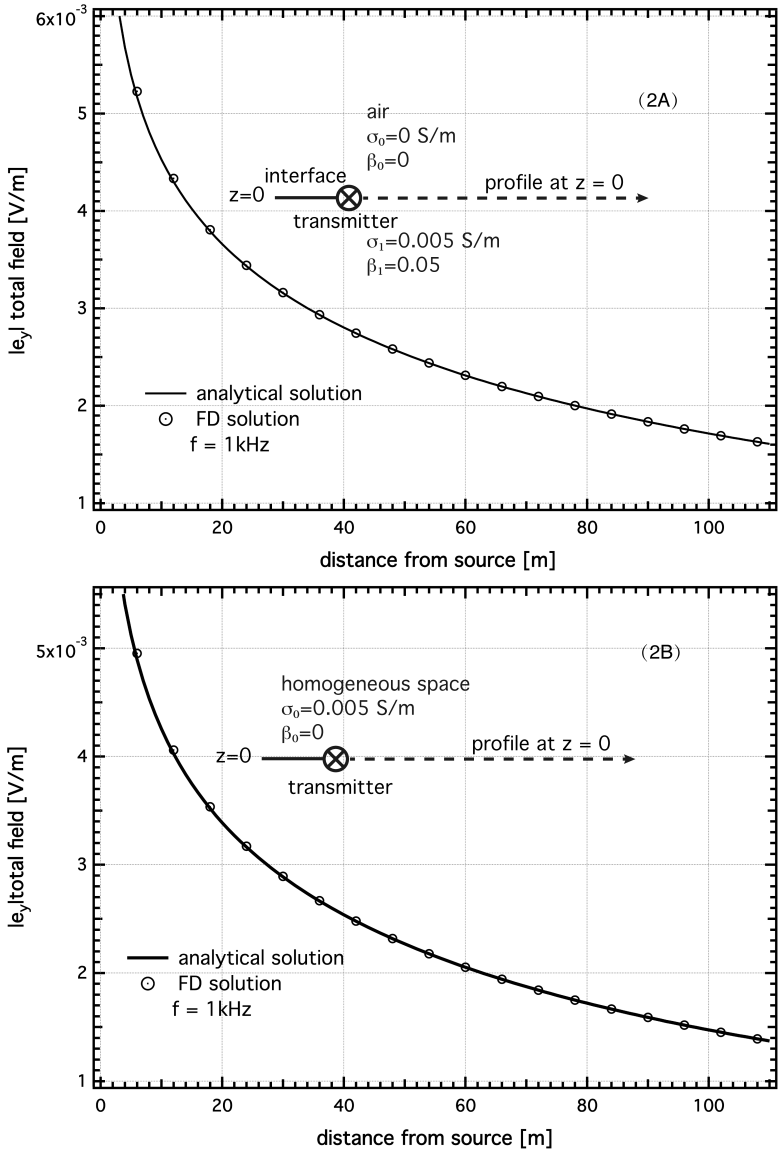

Figure 4.2: (a) Comparisons between FD and analytical solutions for the total field e_y to the half space model. The air conductivity and roughness are zero, and the subsurface conductivity is 0.005 S/m and roughness 0.05. The receivers locate at $z = 0$, right at the interface. The positive direction along x points from left to the right, as indicated by the annotation. (b) The homogeneous model with whole space conductivity 0.005 S/m and roughness 0. This model is the reference model to reflect the error effect of discretization. Note that the 10 kHz Laplace frequency, s, results in a real-valued electric field.

conductivity and roughness discontinuities in the space. Comparing results in Figure 4.2A and B, both of the relative errors at the node closest to the source location are ~ 0.01, and at other locations are much the same. This reflects that the major cause for the error is not due to the averaging scheme on the material property. Additional testing does show that finer grids could eliminate the error on the nodes around the source location, but it is outweighed by the additional computational cost.

The total unknowns in our problem is $204 \times 204 = 41616$ (not including the nodes at boundaries), for which it takes < 10 s for MUMPS to reach the solution on a single processor.

4.5 Fractional diffusion analysis of a 2D fault contact model

With confidence in the accuracy of the FD solution, we proceed to explore the behavior of EM eddy currents in spatially hierarchical media. The computational grids are the same as used in the previous validation exercise. In Figure 4.3 is shown the test problem geometry: air occupies the upper halfspace, while the subsurface consists of a buried fault zone located in the contact region between two quarterspaces. The roughness of the quarterspaces is $\beta = 0$, forming a heterogeneous but non-fractured background.

The fault zone is contained in the right quarterspace, with its left boundary in contact with the vertical interface between the two quarterspaces. The width of the fault zone is 30 m, while its bottom extends to the mesh boundary. The roughness of the fault zone is not zero, as it is expected to contain many fractures. In this modeling exercise, both the conductivity and roughness of the fault zone are varied.

We display the modeling result in terms of the secondary field, or difference between the total and primary field. The latter is the response of a background model without conductivity anomalies. The secondary field is frequently used in

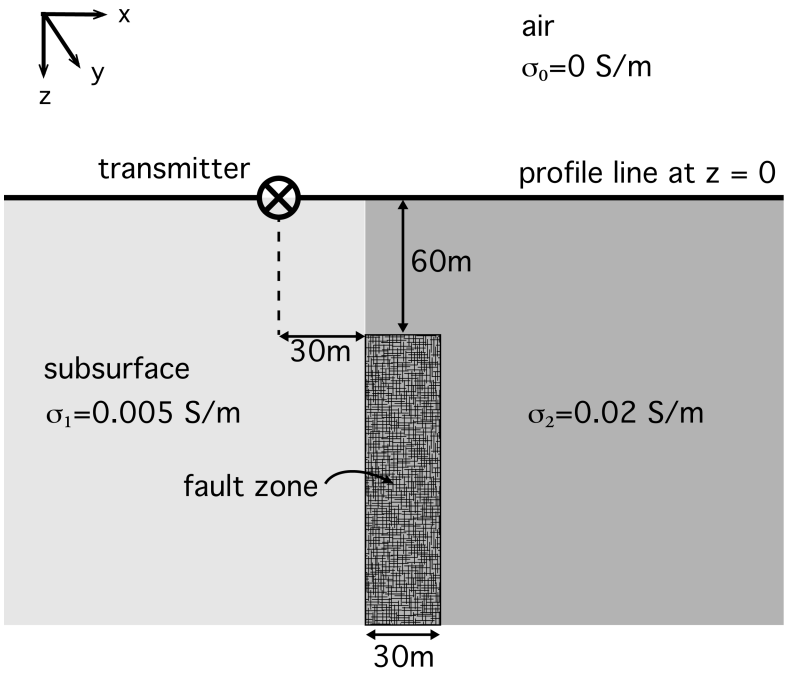

Figure 4.3: Schematic drawing of the 2D fault model. Below the air-Earth interface, left of the fault zone conductivity is 0.005 S/m and roughness β is 0; right of the fault zone conductivity is 0.02 S/m and roughness β is 0. The conductivity and roughness of the fault zone are varied. The profiles location is at the interface.

practice for locating small-scale conductivity anomalies, whose induced response is usually a small fraction the primary response. In our problem, the background model is formed by the upper halfspace and the lower two quarterspaces, without the fault zone. To calculate the primary field, we establish the boundary conditions using Equation 4.11 with lower-halfspace conductivity set to that of the left or right quarterspace, as appropriate. We use the same boundary condition for the total field calculation. This is justified since the boundary is far removed from the source and the secondary response there is assumed to be greatly attenuated.

In Figures 4.4 and 4.5 is shown the FD-computed secondary response of the fault zone as a function of receiver location. In Figure 4.4, the conductivity of

the fault zone is 0.5 S/m and its roughness β varies from 0.01 to 0.6. In Figure 4.5, the roughness β of the block is fixed at 0.1 while its conductivity varies from 0.001 to 1.0 S/m. As expected, the secondary response generated by the fault-zone anomaly peaks above the zone. The peak amplitude varies with conductivity and roughness of the fault zone. A resistive anomaly enclosed within a relatively conductive background generates a positive response, and vice versa. The secondary response is also expected to vary with frequency. For receiver locations outside the zone, the secondary response diminishes quickly.

It is interesting to note that, for certain combinations of fault-zone conductivity and roughness, i.e. the curve labeled $\beta = 0.368$ in Figure 4.4 and $\sigma_1 = 0.048$ S/m in Figure 4.5, the secondary field response vanishes and the zone cannot be detected. In classical diffusion theory, the vanishing of the secondary response implies that the conductivity of the fault zone is the same as the background. However, in the anomalous diffusion approach, a zero secondary response clearly does not necessarily indicate the same conductivity of the anomaly and the background.

The foregoing analysis suggests an advantage of the fractional diffusion model. Recall that the classical diffusion coefficient for EM eddy currents is $1/(\mu_0\sigma_0)$. As μ_0 is constant, conductivity is the single parameter that controls the diffusion rate. However, with reference to the first term in the right hand side of Equation 4.5, the anomalous diffusion constant is related to a coupling term $\sigma_1 s^{1-\beta}$, and is controlled by both the conductivity and the roughness β. In the classical diffusion case with conductivity σ_0, this term converges to $\sigma_0 s$. Hence, the response of the anomalous diffusion will appear to be "classical" when the conductivity $\sigma_1 = \sigma_0 s^{\beta}$; or equivalently, when $\beta = ln(\sigma_1/\sigma_0)/ln(s)$. It is conventional to use a layered model with piece-wise constant conductivities to simulate inhomogeneities in the earth. However, when using the fractional diffusion approach, fewer parameters are needed to

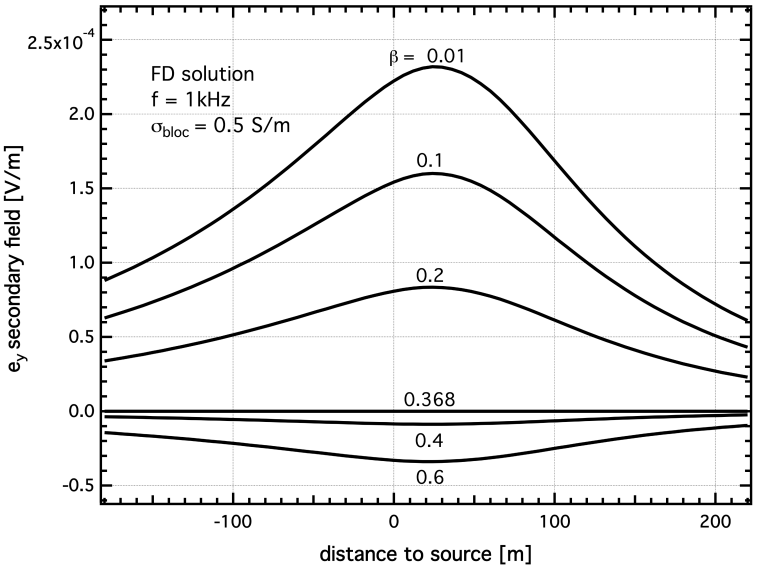

Figure 4.4: FD solutions for the secondary e_y fields of the 2D fault model along x at $z = 0$. The conductivity of block is 0.5 S/m. The plot varies with different roughness of the zone ranging from 0.01 to 0.6. The configuration of the model is drawn in Figure 4.3. Note that the real-valued Laplace variable, s, results in a real-valued electric field.

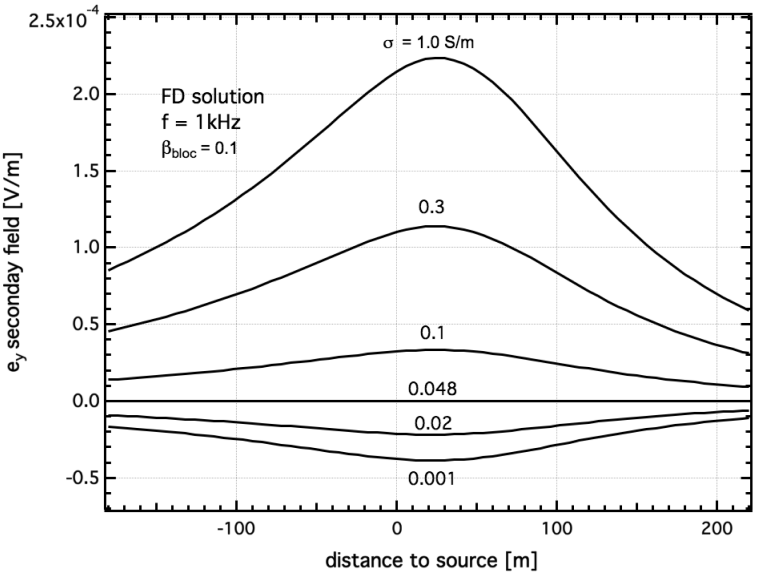

Figure 4.5: FD solutions for the secondary e_y fields of the 2D fault model along x at $z = 0$. The roughness β of the zone is 0.1. The plot varies with different conductivites ranging from 0.001 to 1.0 S/m of the zone. The profile layout is the same with Figure 4.4. Note that the real-valued Laplace variable, s, results in a real-valued electric field.

describe the EM response of spatially hierarchical geoelectrical structures.

In our following companion paper, we will extend our study to the 2.5D modeling problem, where a 3D loop source is deployed over a 2D fractured structure, whose conductivity and roughness are invariant along the strike direction. The governing fractional Maxwell equations are Fourier transformed in the along-strike direction and solved by the staggered-grid FD approach in the along-strike wavenumber domain. The spatial domain solutions are obtained by the inverse Fourier transform of the results. As the 3D source geometry is more frequently used in real experiments, this work would provide more insightful results that are comparable with the field data.

4.6 Conclusion

The fractional EM diffusion equation can efficiently model eddy currents in rough media. The spatially hierarchical diffusion of eddy currents is treated by introducing a roughness parameter β. We have modeled 2-D secondary responses in the frequency domain to line source excitation. A future publication will compute 2.5-D responses in the time domain to compare with actual data from TDEM surveys.

The EM fractional diffusion equation is discretized herein by a standard finite difference method and nodes near material interfaces are specially treated by a spatial averaging scheme. The sparse matrix equation system is solved by the MUMPS direct solver implemented with the PETSc open-source computational package. We found excellent agreement between the FD solution and analytical total-field solutions for the half space model. A 2D fault zone response is then investigated and behaves as expected. The fractional diffusion theory introduces an additional material parameter, roughness, to describe fracture zones. In such geological formations, it is of interest to compare the anomalous and classical descriptions of EM diffusion. Our results show that certain combinations of faultzone conductivity and response

may generate a zero secondary response and the zone would be undetected. Future work includes finding equivalent classical models to further understand the physical meaning of the roughness parameter β and, particularly, its precise relationship to fracture density. Moreover the modeling will be extended to the time domain with 2D and 2.5D problem geometries in order to expand our understanding of EM fractional diffusion.

5. FRACTIONAL DIFFUSION ANALYSIS OF THE ELECTROMAGNETIC FIELD IN FRACTURED MEDIA PART II: 3-D APPROACH

5.1 Introduction

The controlled-source electromagnetic (CSEM) technique is well-established for non-invasive hydrocarbon exploration [72], aquiferous zone characterization, and lithosphere geological mapping [21]. Due to the strong attenuation of earth materials to electromagnetic signals, the effective depth of most CSEM surveys is restricted to 1-2 km, a zone where pores and fractures over various length scales are highly complicated. It is evident from many previous studies that inhomogeneities and fractures in near-surface geological formations have a fractal structure over a wide range of spatial scales [9, 35, 77]. The scaling of heterogeneities often follows a power-law distribution. Spatial confinement of fluid or electric charge transport by the fractal geometry gives rise to interesting dynamic processes within the pore space and fractures, such as anomalous diffusion [8, 23, 28]. Research on anomalous hydraulic transport has been intensively conducted [28]. Statistically, the mean-square displacement of a tracer of contaminant particle transported within a fractal geometry obeys a fractional power law function of time, with the exponent smaller than unity, indicating a subdiffusion process .[47] The characteristic long-tail signature developed in the concentration curve at late time differentiates the process from classical, Gaussian-like diffusion.

The CSEM technique analyzes the diffusion of electromagnetic eddy currents at sufficiently low frequencies that displacement currents can be neglected. The geoelectrical structure of a naturally fractured subsurface is likely to have a similar fractal geometry as the fracture system itself. Moreover, the pathways of electrical currents

are spatially correlated with those of the hydraulic flow [12]. Thus it is expected to observe fractional diffusion phenomenon for electromagnetic eddy currents in fractured geological media [23, 73]. The key task is to quantify the connection between CSEM data and parameters that describe the electrical conductivity of a self-similar conducting Earth. Conventionally, CSEM data are interpreted in terms of a 1-D, 2-D or 3-D piecewise constant geological structure with uniform conductivity and thickness of each cell. A very fine grid, and hence a lot of computation time, are needed to build and evaluate a model that can explain the Earths actual 3D CSEM response. Good accuracy may not be captured, using the conventional approach, in the presence of multi-scale hierarchical geoelectrical structure. Alternatively, the CSEM response of such structures are easily evaluated if the physics of anomalous diffusion of electromagnetic eddy currents is recognized and cast, for example, in terms of a continuous time random walk (CTRW) [47]. Such a re-formulation leads to a generalization of Maxwell equations containing a fractional order time derivative [19, 26]. The fractional order of the derivative is equivalent to a roughening of the geological medium, introducing multi-scale variations of fractures and heterogeneities in a compact manner. This theory renders CSEM modeling and inversion much more efficient, as only a few model parameters are now required to be fit.

The Maxwell fractional-derivative equation can be solved using the finite difference (FD) method in both time [39] and frequency [26] domains. Most of the time domain methods are implicit. Such methods are memory intensive since to compute each time step, solutions from previous steps are involved. Yuste and Acebo[78] proposed a memory-efficient, explicit method based on a first-order truncated Grunwald-Letnikov fractional derivative. The governing fractional-order equation is then solved in either Laplace or frequency domain. The Laplace transform of a fractional derivative is just a fractional order power function of the Laplace variable s [54]. Everett

[19] derived the 1-D analytical solution to the fractional Maxwell equation in Laplace domain and transformed it to time domain using the Gaver-Stehfest method. Ge et.al.[26] developed a 2-D FD approach to modeling the CSEM response of a fault zone possessing hierarchical geoelectrical structure. In this paper, we describe a 3-D FD scheme to solve the fractional Maxwell equation on a staggered grid. A statistical multi-scale fracture model is created based on a power-law autocorrelation function. The classical Maxwell equation solution is then compared with equivalent model responses generated from fractional diffusion formulation. We explore the correspondence between the fractional and classical model responses at various frequencies to probe whether the classical Maxwell equation can capture multi-scale electromagnetic diffusion processes in hierarchical Earth structures. The fractional-order Maxell equation is naturally equipped to describe such phenomena.

5.2 Modeling method

5.2.1 Fundamental derivation

The fractional Maxwell equation, as described by Everett [19], incorporates the fractional time derivative as a Riemann-Louiville (R-L) integral operator. Combining Amperes law and Faradays laws and eliminating the magnetic field $\mathbf{B}$, the electric field $\mathbf{E}$ satisfies the fractional vector-Helmholtz equation:

$$\nabla \times \nabla \times \mathbf{E}(t) = -\mu_0 \sigma_{\beta 0} D_t^{1-\beta} \mathbf{E}(t) - \mu_0 \frac{\partial}{\partial t} \mathbf{J}_s(t), \tag{5.1}$$

where μ_0 is the free space magnetic permeability, σ_β is a generalized conductivity, $\mathbf{J}_s$ is the source current density, and

$${}_0D_t^{1-\beta} \mathbf{E}(t) \equiv \frac{1}{\Gamma(\beta)} \frac{\partial}{\partial t} \int_0^t \frac{dt' \mathbf{E}(t')}{(t-t')^{1-\beta}} \tag{5.2}$$

is the R-L integral operator [54]. The "roughness" parameter β ranges between 0 and 1 and indicates the degree of heterogeneity of the medium, or in our case the multi-scale variability of the geoelectrical structure as it is induced, for example, by natural fractures. The limit $\beta \to 0$ corresponds to classical electromagnetic diffusion within a piecewise homogeneous medium. Conveniently, the Fourier transform of the R-L operator has a simple analytic form [47]:

$$\mathcal{F}\{{}_0D_t^{1-\beta}\mathbf{E}(t)\} = (i\omega)^{1-\beta}\tilde{\mathbf{E}}(\omega) \tag{5.3}$$

To obtain a non-singular solution at the location of the physical source, we choose to work with the secondary electric field $\mathbf{E}^s$ defined by:

$$\mathbf{E}^s = \mathbf{E}^t - \mathbf{E}^p, \tag{5.4}$$

where the total electrical field $\mathbf{E}^t$ is split into a known primary field $\mathbf{E}^p$ excited by a layered background model and an unknown secondary field $\mathbf{E}^s$ excited by local conductivity anomalies. Equation 5.1 is then transformed into frequency domain, assuming $e^{i\omega t}$ time dependence, to obtain:

$$\tilde{\nabla} \times \tilde{\nabla} \times \tilde{\mathbf{E}}^s + \mu_0\sigma_\beta(i\omega)^{1-\beta}\tilde{\mathbf{E}}^s = -\mu_0[(i\omega)^{1-\beta}\sigma_\beta - i\omega\sigma^p]\tilde{\mathbf{E}}^p, \tag{5.5}$$

where σ^p denotes the background conductivity model, and the right-side indicates the source term. Equation 5.5 is the fundamental equation to be solved herein by the FD approach.

5.2.2 Discretization scheme

The fractional vector-Helmholtz Equation 5.5 is discretized on a 3-D face-centered staggered grid [65, 68]. The Cartesian components of the secondary electric fields are evaluated at the corresponding face centers of each cell. The two model parameters, electric conductivity σ and roughness β, are assumed to be constant within each cell. The values of these parameters at a cell face-center are volumetric averages of their values in adjacent cells sharing the common face. For example, the conductivity on the nodes of E_x is

$$\sigma_{i+1/2,j,k} = \frac{\Delta x_i \sigma_{i,j,k} + \Delta x_{i+1} \sigma_{i+1,j,k}}{\Delta x_i + \Delta x_{i+1}}, \tag{5.6}$$

where$\sigma_{i+1/2,j,k}$ is assigned to the common face center of the i^{th} and $(i+1)^{th}$ cells along the x-direction, and Δx is the width of each cell in the x-direction. A similar averaging scheme is applied separately for the roughness β.

As customary in CSEM modeling, a homogeneous Dirichlet boundary condition is applied to the secondary electrical field at the exterior boundary of the grid. The size of the five most exterior cells is increased successively by a factor of two, to minimize the boundary effects. The aforementioned discretization scheme results in a linear equation system:

$$\mathbf{A}\mathbf{E}^s = \mathbf{J}^s, \tag{5.7}$$

where matrix $\mathbf{A}$ is complex and non-symmetric. It is preconditioned using incomplete LU factorization [60] and the Equation 5.7 is solved using the biconjugate gradient stabilized (BiCGS) method [69]. The solver is robust in the 10 Hz $\sim$ 10 kHz frequency range, obviating the need for a divergence correction [65]. The entire workflow is implemented in the PETSc scientific parallel computation package [5]. After the values for secondary electric field are obtained at each node, the magnetic

field components are calculated by an FD representation of Faraday's law at the middles of the edges of each cell.

5.2.3 1D layered model verification

To verify the accuracy of the FD scheme, a rough 1D layered model (Figure 5.1) is created for testing the numerical code against the equivalent analytical solution. In the model, the background medium is nonfractured ($\beta = 0$) and homogeneous with conductivity $\sigma_1 = 0.03$ S/m. The model contains a rough conductive layer in the depth interval 30-260 m with conductivity $\sigma_2 = 0.1$ S/m and roughness $\beta_2 = 0.1$. An air layer of thickness 100 m overlies the subsurface. A loop source of 3 m radius carrying an oscillating current of amplitude 1 A resides at the origin of the Cartesian coordinates. The model is discretized using a $72 \times 72 \times 72$ interior uniform mesh with nominal cell size $20 \times 20 \times 10$ m, comprising a total of 1.1 million unknown secondary electric field values.

The analytical solution for a rough 1-D model takes the form of a Hankel transform [71]. The expression in the Laplace domain for the vertical component of magnetic field is

$$B_z = \frac{\mu_0 I a}{2} \int_0^\infty (e^{-\gamma_0(z+h)} + r_{TE} e^{\gamma_0(z-h)}) \frac{\lambda^2}{\gamma_0} J_1(\lambda a) J_0(\lambda \rho) d\lambda \tag{5.8}$$

where I is the current amplitude, a is the radius of the loop, h is the height of the loop above the surface, J_0 and J_1 are Bessel functions of the first kind and $\gamma_0^2 = \lambda^2 + s^{1-\beta}\mu_0\sigma_0$. In the present case, $\sigma_0 = \beta_0 = 0$ since medium-0 corresponds to air, and the frequency-domain solution is found by the replacement $s = i\omega$. The reflection coefficient r_{TE} can be calculated using a matrix recursion method and involves the non-zero conductivity and roughness values of each of the layers [71]. The Hankel transform in Equation 5.8 is evaluated using a digital filter [31]. Comparisons

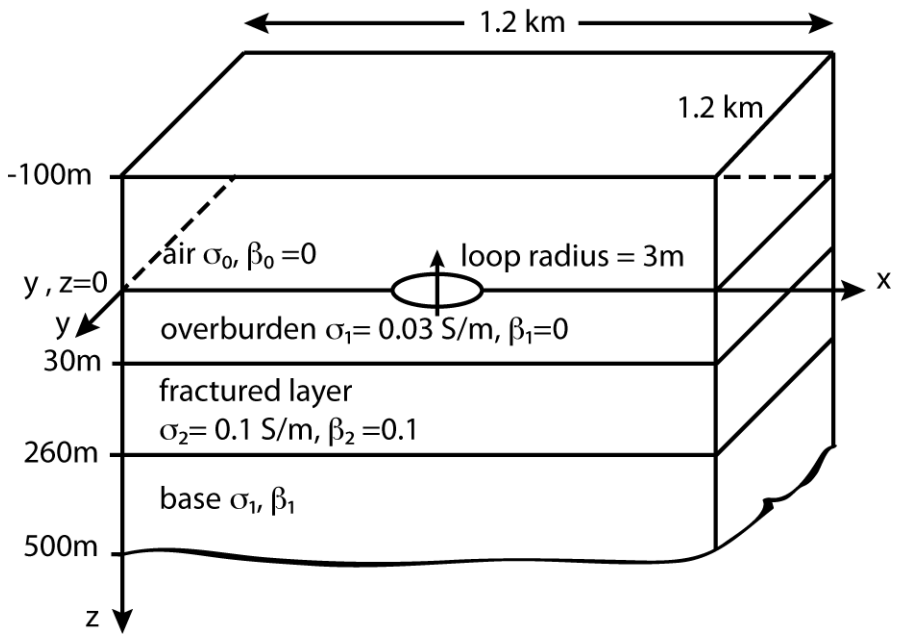

Figure 5.1: The 1-D layered model with rough conductive layer between z=30-260 m. There is excellent agreement in the real component at these frequencies. The cusps in the 100-Hz and 10-kHz response curves correspond to locations where the vertical magnetic field flips sign. As the frequency decreases below 1 Hz or increases above 10 kHz, the computational cell size becomes, respectively, too coarse or too fine relative to the skin depth of the EM signal to achieve such an excellent agreement.

between the FD and analytical solution for B_z at three frequencies are shown in Figure 5.2. The profile is taken at the surface along the x direction, at $y = 60$ m.

There is excellent agreement in the real component at these frequencies. The cusps in the 100-Hz and 10-kHz response curves correspond to locations where the vertical magnetic field flips sign. As the frequency decreases below 1Hz or increases above 10kHz, the computational cell size becomes, respectively, too coarse or too fine relative to the skin depth of the EM signal to achieve such an excellent agreement.

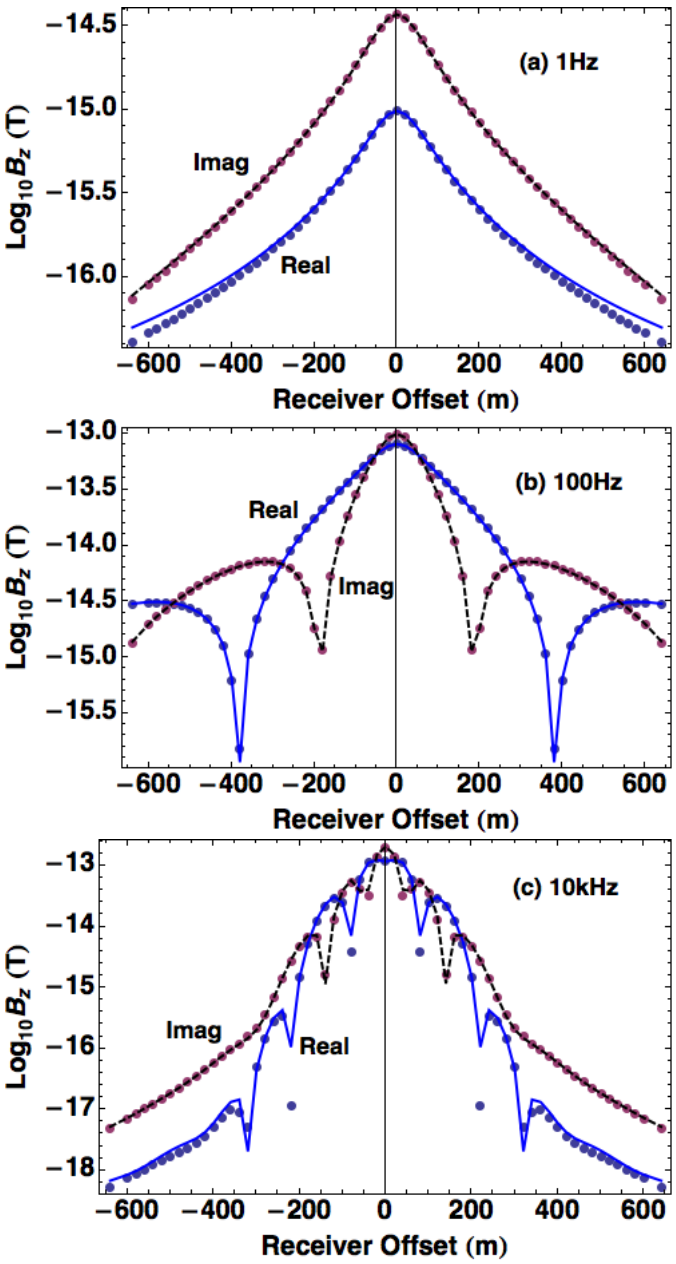

Figure 5.2: Comparisons between FD (symbols) and 1-D analytic (lines) solutions for secondary B_z at (a) 1Hz, (b) 100Hz and (c) 10kHz.

5.2.4 3D block model verification

To verify the accurateness of the 3D finite difference program for the galvanic effect, which may result modeling errors when a discontinuity of the electrical field presents when the field crosses a conductivity interface in the normal direction [11], I generate a FD solution to the vertical magnetic field strength of a 3D conductive block model developed by Pridmore et.al. [59]. The FD solution is compared against a finite element solution in [59] and generated from **E** fields using the Green's function. The model configuration is shown in Figure 5.3. The TX is running at 1 kHz. The block center is 75 m from the loop TX center in x direction, with dimension of 30 m in x and 120 m in y directions and height 90 m. The top of the block is at 30m deep. Conductivity of the block is 1.0 S/m. The subsurface background conductivity is 0.0333 S/m. The profile is taken in the x direction.

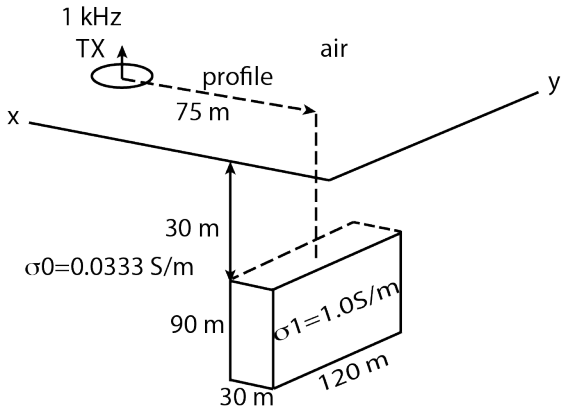

Figure 5.3: Layout for a 3D conductive block model. Modified from [59].

Figure 5.4 and Figure 5.5 show the comparison between the FD (red dot) and FE solutions (blue dot) using two sets of grids of different grid sizes to generate solutions. The coarse grid has minimum cell size 15 m in x and z directions and 20

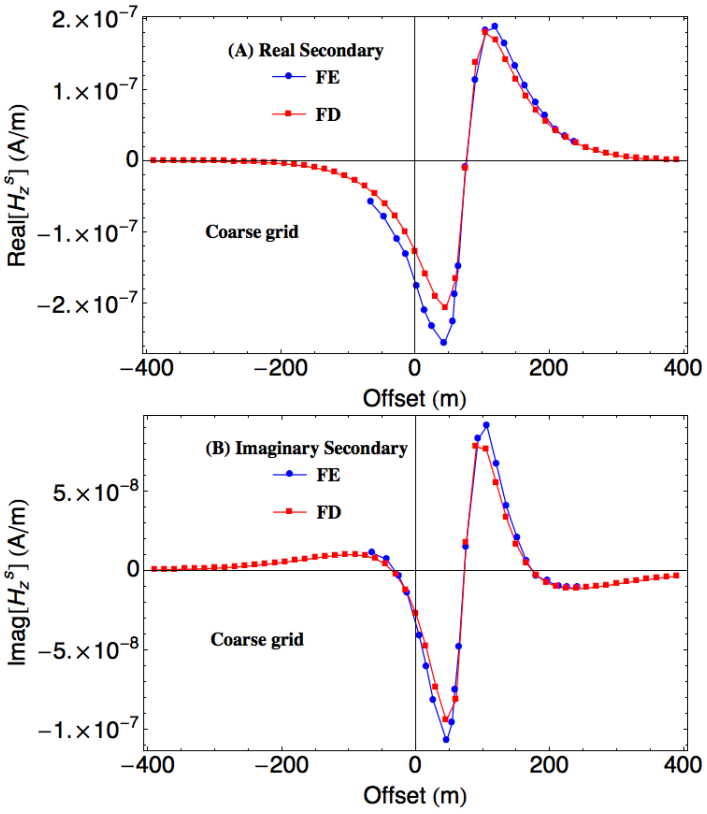

Figure 5.4: Comparisons between FD (red square dot) and FE analytic (blue round dot) solutions for secondary H_z of the 3D block model using a coarse grid.

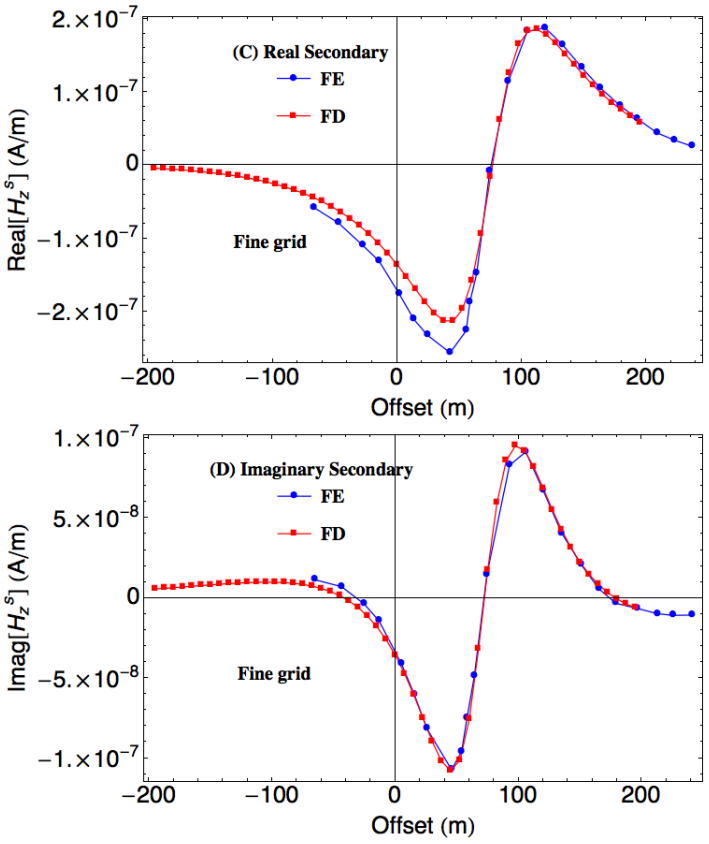

Figure 5.5: Comparisons between FD (red square dot) and FE analytic (blue round dot) solutions for secondary H_z of the 3D block model using a fine grid.

m in y directions. The fine grid has minimum cell size 7.5 m in x and z directions and 10 m in y directions. In general, the real and imaginary components of FD and FE solutions are in good agreement with each other, except for a little misfit in the real component in region to the left of 50 m. The fine grid solution has a better fit than the coarse grid solution. An empirical standard for a reasonable cell size is 10 times smaller than the skin depth, to obtain a good numerical accuracy. Since the skin depth within the block is 16 m, which is comparable with the coarse cell size, the fine grid solution is improved with a smaller grid size, even it does not meet the empirical standard. In the following modeling work, the grid size will be adjusted to meet the standard as the source frequency changes. I generate a broader range for the FD solution, to show that the secondary field will fall off at locations further from the anomaly block, since it is excited by the block.

5.3 3D Fractured model response investigation

5.3.1 3D random media model generalization

To accurately calculate the classical CSEM response of a fractured geological formation, it is essential to capture the complexity of the geoelectrical structure on a discrete 3D grid. It is impractical to model the fine details of the fracture geometry and heterogeneities of the formation. But it is possible to model spatially-averaged statistical properties of the actual formation by generating a random medium [30, 34, 77]. The basic idea is to decompose the conductivity into a large-scale deterministic representation superimposed with small-scale fluctuations:

$$\sigma(\mathbf{x}) = \sigma^0 + \delta\sigma(\mathbf{x}), \tag{5.9}$$

where σ_0 denotes the large-scale simple structure and represents small-scale random inhomogeneities.

Our procedure to generate a random medium follows [37]: (1) define an autocorrelation function on the 3-D grid and calculate its Fourier power spectrum in the wavenumber domain; (2) calculate the Fourier transform of a white noise field defined on the same grid; (3) multiply the square root of the autocorrelation spectrum with the Fourier transform of the white noise field, and transform the product back to the spatial domain, and label the result as $\delta\sigma(x)$. Then the complete stochastic conductivity model $\sigma(x)$ is obtained by adding $\delta\sigma(x)$ to σ_0.

Common autocorrelation functions for realizing stochastic geological media include von Kármán, exponential and power law. Random media generated by these functions retain a fractal-like self-similar property over certain length scales. The isotropic von Kármán correlation function used herein is:

$$C_k((r(\mathbf{x}))) = \frac{2^{1-\nu}}{\Gamma(\nu)}(\frac{r}{a})^{\nu}K_{\nu}(\frac{r}{a}) \quad -\frac{1}{2} < \nu < 1 \cap \nu \neq 0 \tag{5.10}$$

where a is the correlation length, K_ν is the Bessel function of second kind of non-integer order, ν is the Hurst number that controls the decay rate of the function, Γ is the gamma function, and $r = |x|$. The 3-D Fourier transform of Equation 5.10 yields:

$$\tilde{C}_k(\mathbf{k}) = \frac{(4\pi a^2)^{1.5}\Gamma(\nu + 1.5)}{(1 + a^2k^2)^{\nu+1.5}\Gamma(\nu)}, \tag{5.11}$$

which corresponds to the power spectrum of $C_K(k)$ in the k-wavenumber domain. Plots of the spectrum with different Hurst numbers and correlation lengths are shown in Figure 5.6. It is worth noting that the von Kármán function exhibits power-law behavior at large wavenumbers. The asymptotic slope is controlled by Hurst

number and corresponds to the roughness, or the multi-scale distribution of fractures. The smaller is ν, the more equably are distributed the small heterogeneities. As ν decreases towards -1.5, the power spectrum becomes pure fractal such that all length scales have the same contribution. On the other hand, the curve flattens at $1/a$. The wavenumber range hosting the falloff of the spectrum indicates the length scales over which the geometry is self-affine. Length scales below the correlation length lie within this range. As $a \to \infty$, the von Kármán function converges to a pure power law function indicating a self-affine medium over all scales. But with a finite correlation length, the von Kármán function acts as a band-limited scale filter.

3-D random media realized on a discrete grid according to the above prescription are shown in Figure 5.7 for different Hurst numbers and correlation lengths. When the Hurst number is large, $\nu = 0.8$, the model is characterized by coarse heterogeneities. The boundaries between the conductivity anomalies and the background matrix are distinct. As ν decreases, the coarse anomalies break down into finer constituents, and the model develops a mosaic texture corresponding to significant power at smaller length scales. The bottom-right panel is generated with $\nu = 0.8$ a shorter correlation length. This model has richer small-scale heterogeneities and fractal-like geometry.

5.3.2 The effect of Hurst number on CSEM response

Since Hurst number is connected to roughness, it is of interest to check how changing the Hurst number of the stochastic conductivity model affects its classical CSEM response.

In the test, a 3-D stochastic ("fractured") conductivity model is constructed (Figure 5.8), using a similar configuration as the rough 1-D model, except that the rough layer of uniform roughness is now replaced by a fractured layer generated using

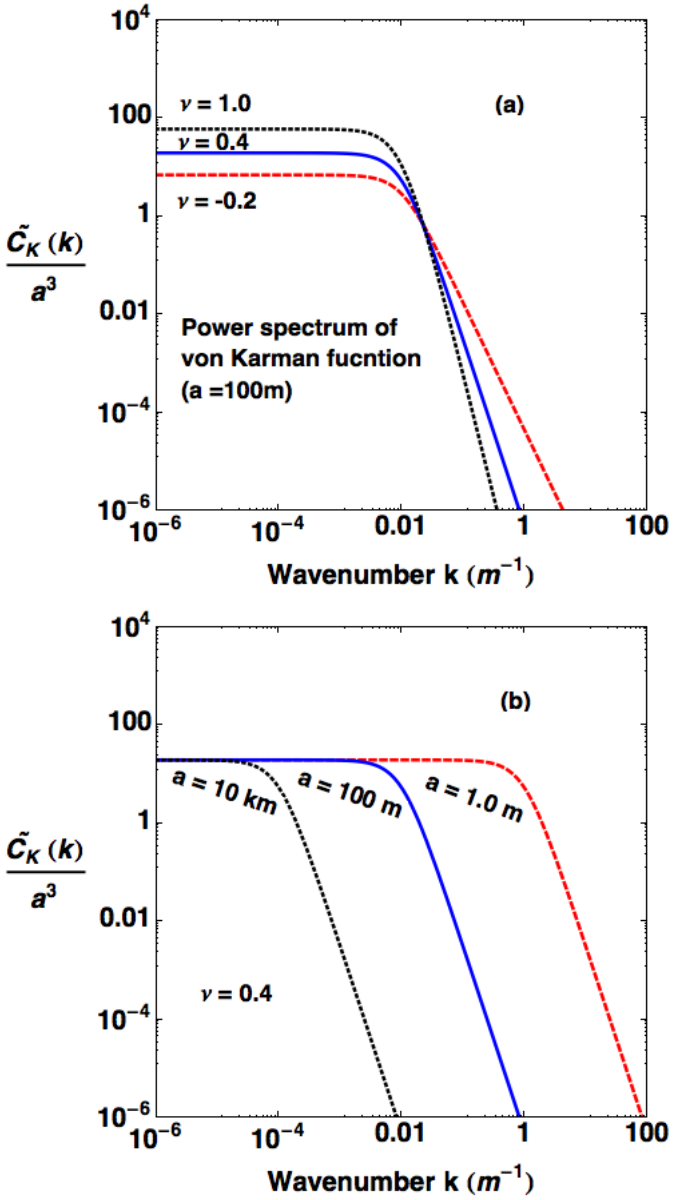

Figure 5.6: Power spectra of the von Kármán correlation function: (a) Hurst number =-0.2, 0.4, 1.0, fixed characteristic length; (b) characteristic length a= 1 m, 100 m, 10 km, fixed Hurst number

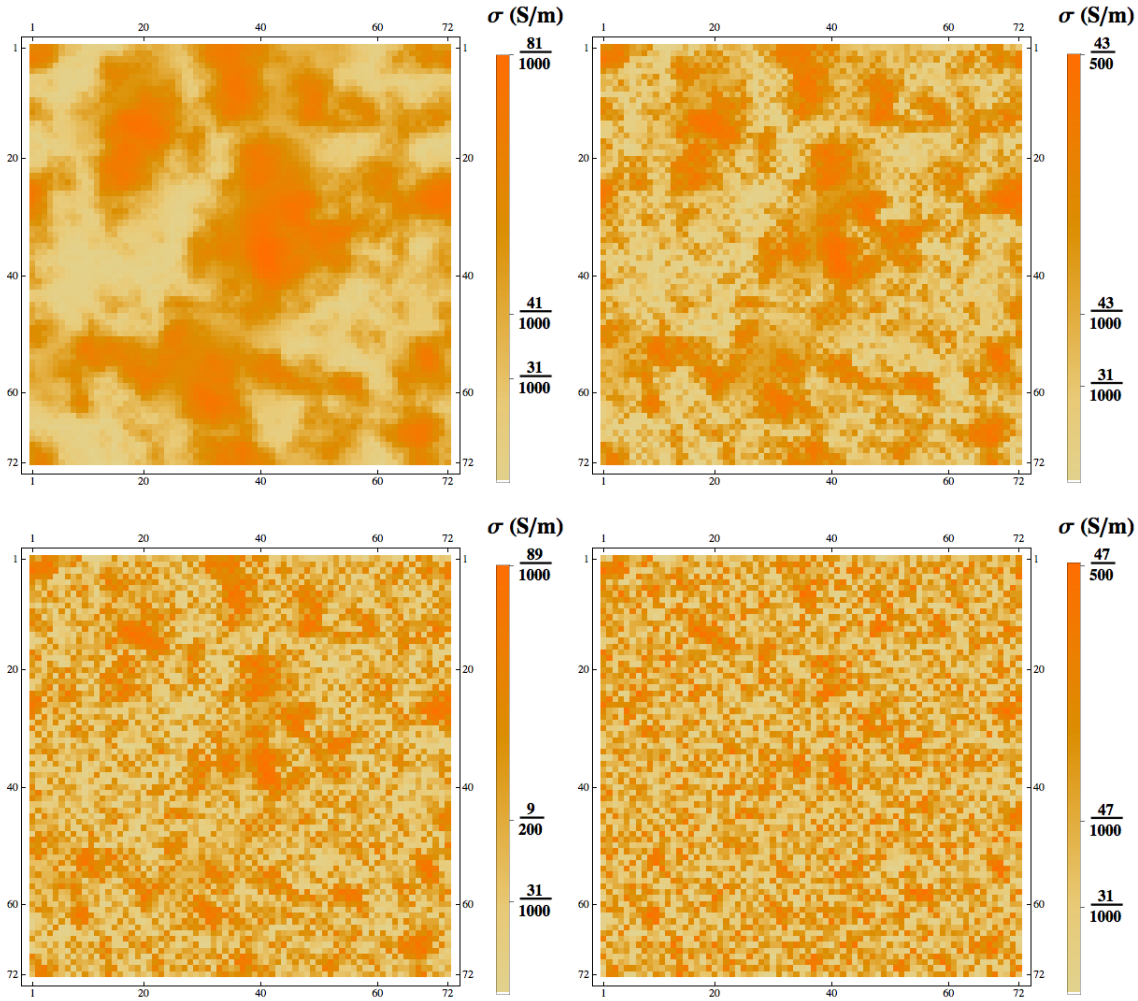

Figure 5.7: Plane views of the top of 3-D random media conductivity models. (a) Top left: $\nu = 0.8, a = 1.0l$; (b) Top right: $\nu = 0.2, a = 1.0l$; (c) Bottom left: $\nu = -0.1, a = 1.0l$; (d) Bottom right: $\nu = 0.2, a = 0.1l$. Note that l is the dimension of the unit cell. The reddish brown color corresponds to conductive anomalies with maximum conductivity 0.1 S/m. The sandy yellow color corresponds to a resistive matrix with conductivity 0.03 S/m.

the statistical approach. The conductivity of the matrix of the layer is 0.03 S/m, as the background, while the fracture conductivity is variable, as high as 0.1 S/m. CSEM responses are evaluated for Hurst numbers ν= -0.1, 0.2 and 0.8. The source is operated at 100 Hz. The real and imaginary parts of B_z are shown in Figure 5.9. For small Hurst numbers -0.1 and 0.2, the responses are similar. Considering the skin depth is ∼300 m, the length scale of the heterogeneities at small Hurst number is below the CSEM resolution. The model response at $\nu = 0.8$ has an observable discrepancy with the other two. A similar effect was found when models with different correlation lengths were tested.

5.3.3 Multi-frequency fractional diffusion analysis

It is of interest to test fractional diffusion responses against classical Maxwell equation solutions at multiple frequencies. For this purpose, we generate two von Kármán type fractured models, as shown in Figure 5.7, with Hurst numbers ν= -0.1 and 0.8. The classical B_z response is first calculated. Then a 3D model is generated containing a uniform, rough subsurface block and its solution is calculated based on the fractional Maxwell equation. The layout for both models is shown in Figure 5.8.

In this test, the roughness β of the block is not specified a priori, but rather is calculated using the conjugate gradient nonlinear inversion technique. The objective function is the $L2$ norm of the difference between classical and fractional B_z responses:

$$||B_z^{classical}(\mathbf{x}, f) - B_z^{fractional}(\mathbf{x}, f, \sigma_0, \beta)||_{L2} \tag{5.12}$$

Noted that the conductivity σ_0 of the block in the model is fixed at 0.08 S/m, while only the roughness is adjusted in the inversion. Model responses at 100 Hz are assessed along three profiles in the x direction, at y = -60, 60, and 120m, for a total of 180 locations. Using the optimal value for β obtained for the 100 Hz responses, the

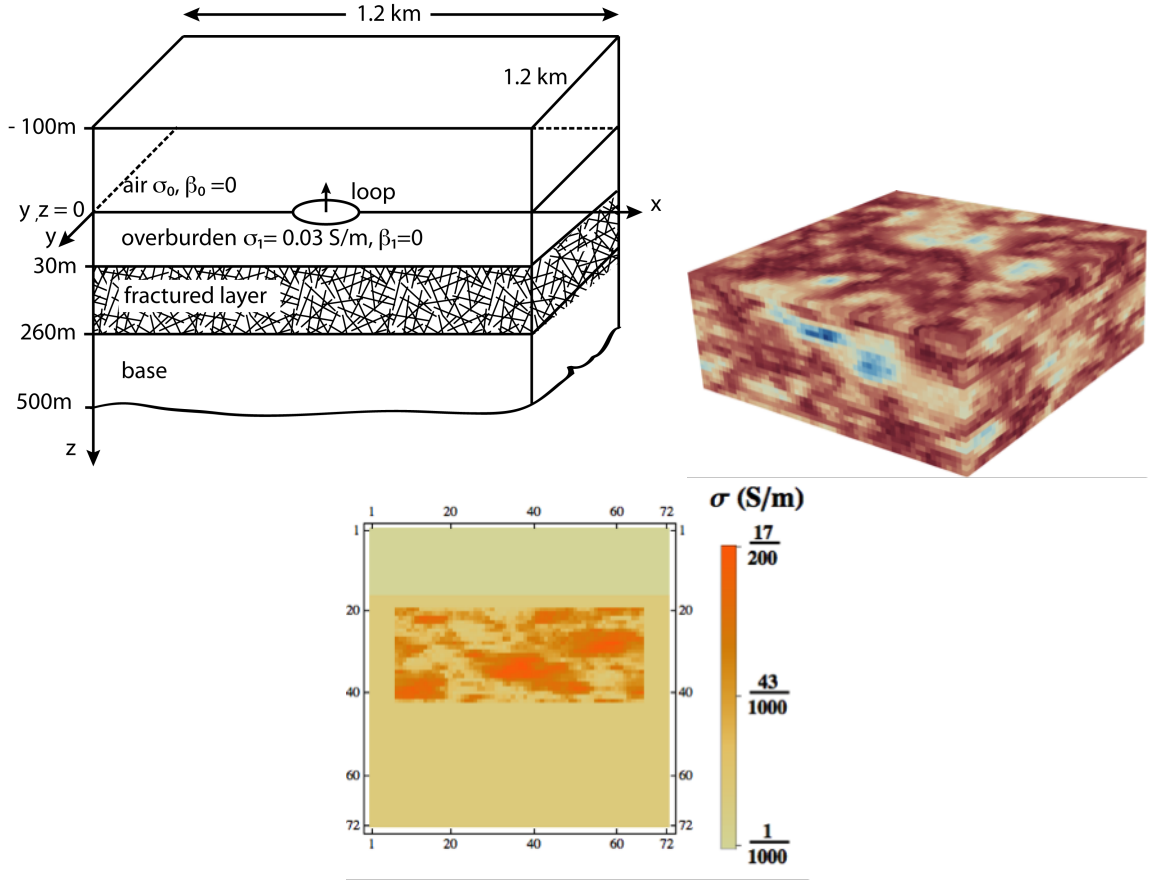

Figure 5.8: (Top left) The 3-D fractured model; (top right) the stochastic conductivity model of the fractured layer; (bottom) horizontal slice of the stochastic model, $\nu = 0.8$.

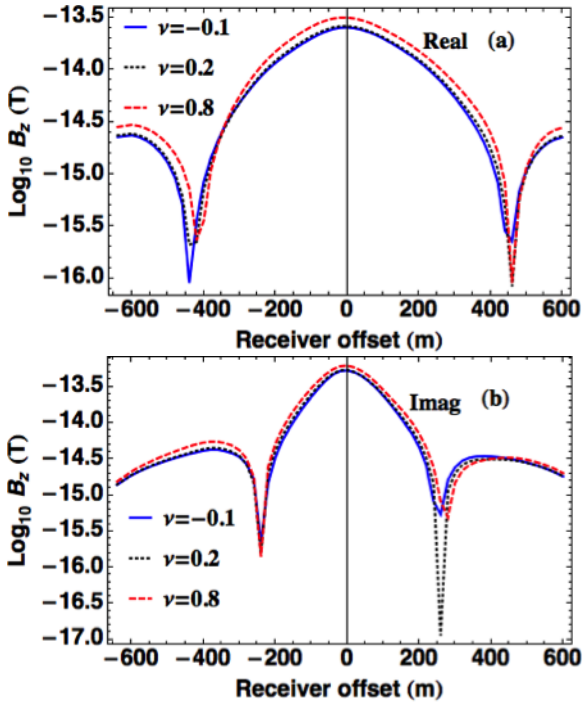

Figure 5.9: Amplitudes of real and imaginary components of B_z for models with Hurst numbers ν = -0.1, 0.2 and 0.8.

classical and uniform responses are then compared at other frequencies. The idea is to investigate if the optimal roughness β derived from the 100 Hz responses applies to other frequencies. In other words, we address the important question: how well does the von Kármán fractured model reproduce the multi-scale response predicted by the fractional diffusion model? The general workflow is given in Figure 5.10.

Figure 5.11 shows comparisons between the classical Maxwell equation solutions for the von Kármán type ($\nu = -0.1$) fracture model and the fractional diffusion solution to the uniform rough block model as well as the effective media block response, in which the block conductivity is uniform at 0.046 S/m and its roughness is zero. The effective media response stands for a classical type resonse. The roughness of the block in the rough model is $\beta = 0.09$, which is the optimal value obtained by

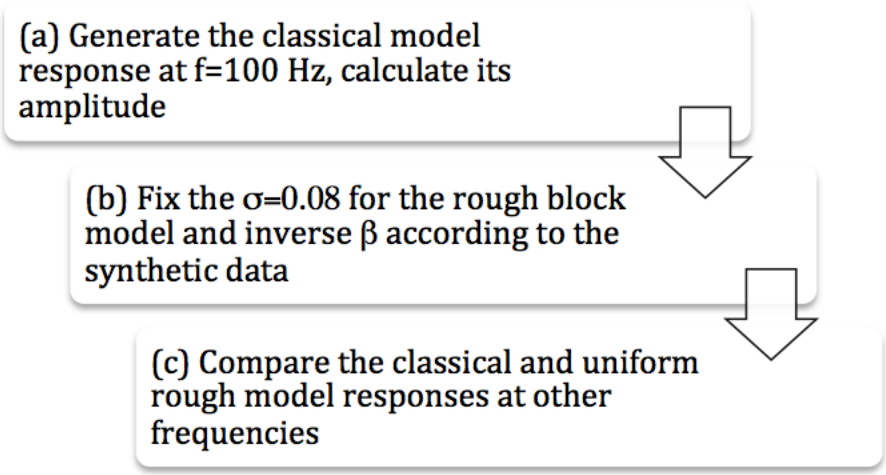

Figure 5.10: The workflow of the multi frequency test.

matching the classical model response at 100 Hz. We also calculate the responses at 10 Hz, 1 kHz and 10 kHz. Except for a good agreement at 100 Hz, a certain amount of discrepancy is observed in the amplitudes between the classical von Kármán response and the anomalous response. The amplitude of the classical solution is lower than the fractional solution at 10 Hz and greater at 1 kHz and 10 kHz. However the classical von Kármán response is consistent with the effective media block response, denoting its classical type.

It is clear from the above results that the optimal roughness found at 100 Hz does not apply to other frequencies. This indicates that the von Kármán type model does not generate an equivalent fractional diffusion response. There are several explanations. First is that the von Kármán type model is not a purely self-affine model. The former has only a band limited power-law length distribution . Secondly, the finite difference mesh is characterized by the size of the unit cell. In the simulations, the smallest cell dimension is 20 m, which is large compared to the scale of nature fractures. It is not possible to model realistic multi-scale geometry on such grids.

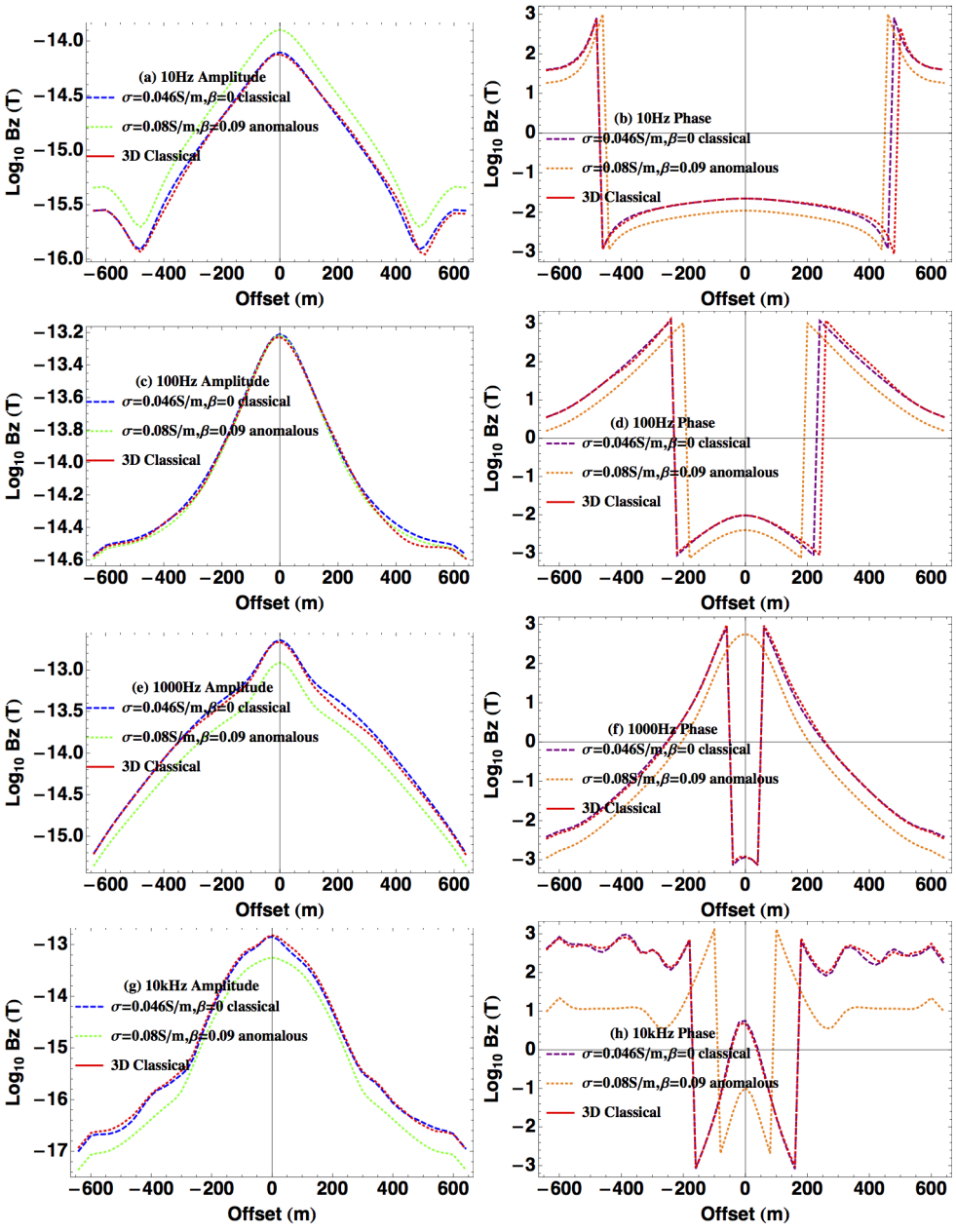

Figure 5.11: Comparisons between the classical von Kármán type ($\nu = -0.1$) fractured model responses (dashed lines), effective media solutions (dotted line) and fractional diffusion solutions to the rough block model (solid lines) at different frequencies. Amplitudes (left) and phases (right) of B_z are shown. The roughness of the block β=0.09, obtained by minimizing the misfit at 100Hz.

It is possible to increase the source frequency and decreases of the size of a unit cell. However the computational costs must be raised to keep the outer mesh dimension large enough to still capture the large-scale fractures. Third, its questionable whether the diffusive CSEM classical physics can resolve wide scale variations in a stochastic conductivity model. The classical responses of the model generated using different Hurst numbers are found to be close, even though the individual models are substantially different.

5.4 Conclusion

We generate a 3D staggered grid finite difference modeling method to discretize and solve the fractional diffusion Maxwell equation. The good agreement between the numerical solution and a semi-analytical solution to a rough layered model response validates the accuracy of the program. We also develop a discrete multi-scale heterogeneous model using the von Kármán type length distribution. It coincides with a band-limited power law function. The classical CSEM response of this model with various Hurst numbers is examined. For small conductivity contrast in the fractured layer, only minor differences are found among responses with different Hurst numbers. Finally, multi-frequency CSEM responses for the classical fractured model and uniform rough block model are investigated. The optimal roughness obtained at 100 Hz does not make the two responses at other frequencies consistent. The likely explanation is that the classical fractured model does not contain enough fracture scales to reproduce the fractional diffusion behavior. A finer computational mesh is essential to further probe the correspondence between classical and fractional electromagnetic diffusion in fractured media.

6. CONCLUSION

This research starts from the classical aspect of the CSEM fundamentals and explore the fractal characteristics of CSEM induction in fractured rocks through numerical modeling approaches, to seek a more precise and compact interpretation of anomalous CSEM data based on the fractional diffusion theory.

In chapter 2, I have reviewed some of the fundamentals of geophysical electromagnetism, including the electrical property of rocks and EM constitution laws. The CSEM survey frequency range is below 1 MHz, where the displacement currents can be ignored. The techniques of frequency domain and time domain CSEM surveys are introduced. Traditionally the observed data are converted to an apparent conductivity profile for interpretation. The zero crossing time is when the sign of responses flip. The analytical solution to the 1D layered model response of a magnetic loop source is derived . The time domain response can be obtained through G-S algorithm based on several frequency domain responses. Various types of model responses are compared. Due to the inductive characteristic of the loop system, the survey is more suited to detect conductive target.

In chapter 3, I overview the reason for the anomalous diffusion to emerge and its significance. The classical ADE fails to capture the full details of the model property as a local method. The CTRW approach convolve with the model complexity with the equation explicitly which makes it successfully predict the anomalous diffusion phenomenon. The fractional calculus as the fundamental theory, provides strong support to the CTRW approach. We choose R-L definition of the fractional derivative to generalize the Maxwell equation. Finally we shows the comparison between classical and anomalous responses of the layered earth model. The transient time

domain measurement can distinguish the difference between two responses very well.

In chapter 4, I show the fractional EM diffusion equation can efficiently model eddy currents in rough media. The spatially hierarchical diffusion of eddy currents is treated by introducing a roughness parameter β. I have modeled 2-D secondary responses in the frequency domain to line source excitation. A future publication will compute 2.5-D responses in the time domain to compare with actual data from TDEM surveys.

The EM fractional diffusion equation is discretized herein by a standard finite difference method and nodes near material interfaces are specially treated by a spatial averaging scheme. The sparse matrix equation system is solved by the MUMPS direct solver implemented with the PETSc open-source computational package. We found excellent agreement between the FD solution and analytical total-field solutions for the half space model. A 2D fault zone response is then investigated and behaves as expected. The fractional diffusion theory introduces an additional material parameter, roughness, to describe fracture zones. In such geological formations, it is of interest to compare the anomalous and classical descriptions of EM diffusion. Our results show that certain combinations of faultzone conductivity and response may generate a zero secondary response and the zone would be undetected. Future work includes finding equivalent classical models to further understand the physical meaning of the roughness parameter β and, particularly, its precise relationship to fracture density. Moreover the modeling will be extended to the time domain with 2D and 2.5D problem geometries in order to expand our understanding of EM fractional diffusion.

In chapter 5, I generate a 3D staggered grid finite difference modeling method to discretize and solve the fractional diffusion Maxwell equation. I also develop a discrete multi-scale heterogeneous model using the von Kármán type length distri-

bution. It coincides with a band-limited power law function. The classical CSEM response of this model with various Hurst numbers is examined. For small conductivity contrast in the fractured layer, only minor differences are found among responses with different Hurst numbers. Finally, multi-frequency CSEM responses for the classical fractured model and uniform rough block model are investigated. The optimal roughness obtained at 100 Hz does not make the two responses at other frequencies consistent, while the good agreement between the von Kármán model response and the effective block model classical response further confirms the classical type of the response generated by the von Kármán model. The likely explanation is that the classical fractured model does not contain enough fracture scales to reproduce the fractional diffusion behavior. A finer computational mesh is essential to further probe the correspondence between classical and fractional electromagnetic diffusion in fractured media.

6.1 Future research plan

Since the field data collected by Everett and Weiss [73, 23] have confirmed the existence of the fractional diffusion characteristics of EM induction in rough natural formations, there should be a corresponding model either classical or fractional to generate such responses. It is impossible to map the complete detail of the natural fracture networks to an artificial numerical model. The fundamental causes of the anomalous diffusion phenomenon is the smooth and broad spectrum of the fracture scale variation which forms the self-similar fractal characteristic of natural media. However in most numerical modeling methods, the model is generated on discrete grids which lose lots of scale spectrum bands and is limited by the unit cell size. Thus it is difficult to find a comparable classical piece-wise constant model to generate a fractional type response.

For the numerical aspect, I propose to employ finite element method which can generate irregular meshes to reduce the minimum cell size and model more complicated scenarios. If the model is created with a fractal geometry containing broad enough spectrum of heterogeneity scales, the fractional type response may be generated.

This is the reason we seek to rely on the fractional diffusion theory based on CTRW approach, which provides a much more compact description of the physics and produce rather explicit result. I also propose to conduct more field experiments, and directly compare the real field data with the fractional diffusion model data, and investigate the correlation between the roughness parameter with the fracture properties, such as the scale variation, the density etc.. If it is successful, the interpretation of anomalous CSEM data will be greatly improved.

REFERENCES

[1] P. R. Amestory, A. Guermouche, L. J.-Y., and S. Pralet. Hybrid scheduling for the parallel solution of linear systems. *Parallel Computing*, 32(2):136–156, 2006.

[2] G. E. Archie. The electrical resistivity log as an aid in determining some reservoir characteristics. *Petroleum Transactions of AIME*, 146(1):54–62, 1942.

[3] E. Badea, M. E. Everett, G. A. Newman, and O. Biro. Finite-element analysis of controlled-source electromagnetic induction using coulomb-gauged potentials. *Geophysics*, 66(3):786–799, 2001.

[4] S. Balay, J. Brown, K. Buschelman, W. D. Gropp, D. Kaushik, M. G. Knepley, L. C. McInnes, B. F. Smith, and H. Zhang. Petsc users manual. Report ANL-95/11–Revision 3.5, Argonne National Laboratory, 2014.

[5] S. Balay, J. Brown, K. Buschelman, W. D. Gropp, D. Kaushik, M. G. Knepley, L. C. McInnes, B. F. Smith, and H. Zhang. Petsc web page, 2014.

[6] B. Berkowitz, A. Cortis, M. Dentz, and H. Scher. Modeling non-fickian transport in geological formations as a continuous time random walk. *Reviews of Geophysics*, 44(2), 2006.

[7] B. Berkowitz and H. Scher. On characterization of anomalous dispersion in porous and fractured media. *Water Resour. Res.*, 31(6):1461–1466, 1995.

[8] B. Berkowitz and H. Scher. Anomalous transport in random fracture networks. *Phys. Rev. Lett.*, 79:4038–4041, 1997.

[9] E. Bonnet, O. Bour, N. E. Odling, P. Davy, I. Main, P. Cowie, and B. Berkowitz. Scaling of fracture systems in geological media. *Reviews of Geophysics*, 39(3):347–383, 2001.

[10] M. Caputo. Linear models of dissipation whose q is almost frequency

independent-ii. *Geophys. J. R. Astr. SOC*, 13(5):529–539, 1967.

[11] S. Constable. Ten years of marine csem for hydrocarbon exploration. *Geophysics*, 75(5):75A67–75A81, 2010.

[12] C. David. Geometry of flow paths for fluid transport in rocks. *Journal of Geophysical Research*, 98(B7):12267–12278, 1993.

[13] B. Davies and B. Martin. Numerical inversion of the laplace transform: survey and comparison of methods. *J. Comput. Phys.*, 33(1):1–32, 1979.

[14] K. Decker and M. E. Everett. Roughness of a layered geological medium and implications for interpretation of the transient electromagnetic response of a loop source. *Symposium on the Application of Geophysics to Engineering and Environmental Problems 2009*, pages 188–196, 2009.

[15] R. N. Edwards. Two-dimensional modeling of a towed in-line electric dipole-dipole sea-floor electromagnetic system: The optimum time delay or frequency for target resolution. *Geophysics*, 53(6):846–853, 1988.

[16] R. N. Edwards. Marine controlled source electromagnetics: Principles, methodologies, future commercial applications. *Surveys in Geophysics*, 26(6):675–700, 2005.

[17] T. Eidesmo, S. Ellingsrud, L. M. MacGregor, S. Constable, M. C. Sinha, S. Johansen, F. N. Kong, and H. Westerdahl. Sea bed logging (sbl), a new method for remote and direct identification of hydrocarbon filled layers in deepwater areas. *First Break*, 20(3):144–152, 2002.

[18] M. E. Everett. *Active electromagnetics at the midocean ridge*. Thesis, University of Toronto, 1990.

[19] M. E. Everett. Transient electromagnetic response of a loop source over a rough geological medium. *Geophy. J. Int.*, 177(421-429), 2009.

[20] M. E. Everett. *Near-surface applied geophysics*. Cambridge University Press,

2013.

[21] M. E. Everett and R. N. Edwards. Transient marine electromagnetics: the 2.5-d forward problem. *Geophy. J. Int.*, 113(3):546–561, 1993.

[22] M. E. Everett and M. A. Meju. *Near-surface controlled-source electromagnetic induction: Background and recent advances*, volume 50 of *Hydrogeophysics*. Springer, New York, 2005.

[23] M. E. Everett and C. J. Weiss. Geological noise in near-surface electromanetic induction data. *Geophy. Res. Lett.*, 29(1):10–1–10–4, 2002.

[24] R. W. Freund. Conjugate gradient-type methods for linear systems with complex symmetric coefficient matrices. *SIAM J. on Sci. and Stat. Computing*, 13:425–448, 1992.

[25] D. Gaver. Observing stochastic processes, and approximate transform inversion. *Operational Res.*, 14(3):444–459, 1966.

[26] J. Ge, M. E. Everett, and C. J. Weiss. Fractional diffusion analysis of the electromagnetic field in fractured media, part i: 2d approach. *Geophysics*, 77(4):WB213–WB218, 2012.

[27] S. Geiger, A. Cortis, and J. T. Birkholzer. Upscaling solute transport in naturally fractured porous media with the continuous time random walk method. *Water Resour. Res.*, 46(12):W12530, 2010.

[28] S. Geiger and S. Emmanuel. Non-fourier thermal transport in fractured geological media. *Water Resour. Res.*, 46(7):W07504, 2010.

[29] L. W. Gelhar, C. Welty, and K. R. Rehfeldt. A critical review of data on field-scale dispersion in aquifers. *Water Resour. Res.*, 28(7):1955–1974, 1992.

[30] J. A. Goff and T. H. Jordan. Stochastic modeling of seafloor morphology: Inversion of sea beam data for second-order statistics. *J. of Geophy. Res.*, 93(B11):13589–13608, 1988.

[31] D. Guptasarma and B. Singh. New digital linear filters for hankel j0 and j1 transforms. *Geophysical Prospecting*, 45(5):745–762, 1997.

[32] M. R. Hestenes and E. Stiefel. Methods of conjugate gradients for solving linear systems. *J. of Res. of the National Bureau of Stadards*, 49:409–436, 1952.

[33] N. Heymans and I. Podlubny. Physical interpretation of initial conditions for fractional differential equations with riemann-liouville fractional derivatives. *Rheologica Acta*, 45(5):765–771, 2006.

[34] L. T. Ikelle, S. K. Yung, and F. Daube. 2-d random media with ellipsoidal autocorrelation functions. *Geophysics*, 58(9):1359–1372, 1993.

[35] A. J. Katz and A. H. Thompson. Fractal sandstone pores: Implications for conductivity and pore formation. *Phy. Rev. Lett.*, 54(12):1325–1328, 1985.

[36] V. Kenkre, E. Montroll, and M. Shlesinger. Generalized master equations for continuous-time random walks. *J. Stat. Phys*, 9(45), 1973.

[37] L. Klimes. Correlation functions of random media. *Pure and applied geophysics*, 159(7-8):1811–1831, 2002.

[38] J. Knight and A. Raiche. Transient electromagnetic calculations using the gaver-stehfest inverse laplace transform method. *Geophysics*, 47(1):47–50, 1982.

[39] T. A. M. Langlands and B. I. Henry. The accuracy and stability of an implicit solution method for the fractional diffusion equation. *Journal of Computational Physics*, 205:18, 2005.

[40] R. J. Leveque and Z. Li. The immersed interface method for elliptic equations with discontinuous coefficients and singular sources. *SIAM J. Num. Anal.*, 31(4):1019–1044, 1994.

[41] C. Li, D. Qian, and Y. Chen. On reimann-liouville and caputo derivatives. *Discrete Dynamics in Nature and Society*, 2011, 2011.

[42] X. Lu and C. Xia. Understanding anisotropy in marine csem data. *SEG Tech-*

nical Program Expanded Abstracts 2007, 2007.

[43] B. B. Mandelbrot. *The fractal geometry of nature*. Macmillan, 1983.

[44] J. D. McNeill. Applications of transient electromagnetic techniques. *Geonics Ltd. Technical Note TN-17*, 1980.

[45] M. A. Meju. Geoelectromagnetic exploration for natural resources: Models, case studies and challenges. *Surveys in Geophysics*, 23(2-3):133–206, 2002.

[46] M. A. Meju, P. Denton, and P. Fenning. Surface nmr sounding and inversion to detect groundwater in key aquifers in england: comparisons with ves-tem methods. *Journal of Applied Geophysics*, 50(1-2):95–111, 2002.

[47] R. Metzler and J. Klafter. The random walk's guide to anomalous diffusion: a fractional dynamics approach. *Physics Reports*, 339:1–77, 2000.

[48] W. Michael and D. L. Alumbaugh. Electromagnetic methods for development and production: State of the art. *The Leading Edge*, 17(4):487–487, 1998.

[49] E. W. Montroll and H. Scher. Random walks on lattices. iv. continuous time random walks and indluence of absorbing boundaries. *J. Stat. Phys*, 9(2):101–135, 1973.

[50] M. N. Nabighian. Quasi-static transient response of a conducting half-space - an approximate representation. *Geophysics*, 44(10):1700–1705, 1979.

[51] I. Neretnieks, T. Eriksen, and P. Tahtinen. Tracer movement in a single fissure in granitic rock: Some experimental results and their interpretation. *Water Resour. Res.*, 18(4):849–858, 1982.

[52] G. A. Newman and D. L. Alumbaugh. Frequency-domain modelling of airborne electromagnetic responses using staggered finite differences. *Geophyical Prospecting*, 43(8):1021–1042, 1995.

[53] G. A. Newman and D. L. Alumbaugh. Three-dimensional induction logging problems, part 2: A finite-difference solution. *Geophysics*, 67(2):484–491, 2002.

[54] K. B. Oldham and J. Spanier. The fractional calculus; theory and applications of differentiation and integration to arbitrary order. *Academic Press*, 1974.

[55] M. L. Oristaglio and G. W. Hohmann. Diffusion of electromagnetic fields into a two-dimensional earth: A finite-difference approach. *Geophysics*, 49(7):870–894, 1984.

[56] G. J. Palacky. Resistivity characteristics of geologic targets. In M. N. Nabighian, editor, *Electromagnetic methods in applied geophysics: theory*, volume 1. Society of Exploration Geophysicists, Tulsa, Oklahoma, 1988.

[57] L. R. Pasion. *Detecting unexploded ordance with time domain electromagnetic induction*. Thesis, Simon Fraser University, 1996.

[58] I. Podlubny. *Fractional differential equations*. Academic Press, New York, 1999.

[59] D. Pridmore, G. Hohmann, S. Ward, and W. Sill. An investigation of finite-element modeling for electrical and electromagnetic data in three dimensions. *Geophysics*, 46(7):1009–1024, 1981.

[60] Y. Saad. *Iterative methods for sparse linear systems*. Siam, Boston, 2003.

[61] H. Scher and M. Lax. Stochastic transport in a disordered solid. ii. impurity and conduction. *Phys. rev. B*, 7:4502–4519, 1973a.

[62] H. Scher and M. Lax. Stochastic transport in a disordered solid. i. theory. *Phys. rev. B*, 7:4491–4502, 1973b.

[63] H. Scher and E. W. Montroll. Anamalous transit-time dispersion in amorphous solids. *Phys. Rev., B Solid State*, 12:2455, 1975.

[64] J. Schmittbuhl, F. Schmitt, and C. Scholz. Scaling invariance of crack surfaces. *Journal of Geophysical Research*, 100(B4):5953–5973, 1995.

[65] J. T. Smith. Conservative modeling of 3d electromagnetic fields, part ii: Biconjugate gradient solution and an accelerator. *Geophysics*, 61:1319–1324, 1996.

[66] G. Srinivasan, D. Tartakovsky, M. Dentz, H. Viswanathan, B. Berkowitz, and

B. Robinson. Random walk particle tracking simulations of non-fickian transport in heterogeneous media. *Journal of Computational Physics*, 229(11):4304–4314, 2010.

[67] H. Stehfest. Numerical inversion of laplace transforms. *Communication of the A.C.M.*, 13:3, 1970.

[68] R. Streich. 3d finite-difference freuqncy-domain modeling of controlled-source electromagnetic data: Direct solution and optimization for high accuracy. *Geophysics*, 74(5):F95–F105, 2009.

[69] H. A. Van der Vorst. Bi-cgstab: A fast and smoothly converging variangt of bi-cg for the solition of nonsymmetric linear systems. *SIAM J. Sci. and Stat. Comput.*, 13(2):631–644, 1992.

[70] S. H. Ward. Electrical, electromagnetic, and magnetotelluric methods. *Geophysics*, 45(11):8, 1980.

[71] S. H. Ward and G. W. Hohmann. Electromagnetic theory for geophysical applications. In M. N. Nabighian, editor, *Electromagneti methods in applied geophysics*, volume 1. Society of Exploration Geophysicists, Tulsa, Oklahoma, 1988.

[72] C. J. Weiss and S. Constable. Mapping thin resistors in the marine environment, part ii: modeling and analysis in 3d. *Geophysics*, 71(6):G321–G332, 2006.

[73] C. J. Weiss and M. E. Everett. Anomalous diffusion of electromagnetic eddy currents in geological formations. *J. Geophys. Res.*, 112(B8), 2007.

[74] C. J. Weiss and G. A. Newman. Electromagnetic induction in a fully 3d anisotropic earth. *Geophysics*, 67(4):1104–1114, 2002.

[75] G. Weiss. *Aspects and applications of random wlaks*. North-Holland, Amsterdam, 1994.

[76] I. Wolfram Research. *Mathematica*. Wolfram Research, Inc., Champaign, Illinois, version 9.0 edition, 2012.

[77] R. S. Wu and K. Aki. Elastic wave scattering by a random medium and the small-scale inhomogeneities in the lithosphere. *Journal of Geophysical Research*, 90(B12):10261–10273, 1985.

[78] S. B. Yuste and L. Acebo. An explicit finite difference method and a new von neumann-type stability analysis for fractional diffusion equations. *SIAM Journal on Numerical Analysis*, 42(5):13, 2006.

[79] Y. Zhang and A. D. Benson. Lagrangian simulation of multidimensional anomalous transport at the made site. *Geophysical Research Letters*, 35(7), 2008.

APPENDIX A

DERIVATION OF THE SOLUTION TO EQUATION 2.12 IN WHOLE SPACE

Due to the symmetry of the source, the azimuthal component is the only component of electric field for the loop source in whole space. Equation 2.12 is more conveniently solved in cylindrical coordinates:

$$\frac{1}{\rho}\frac{\partial}{\partial\rho}(\rho\frac{\partial e(\rho,z)}{\partial\rho})+\frac{\partial^2 e(\rho,z)}{\partial z^2}=i\mu_0\sigma_0\omega e+i\mu_0\omega J_s \tag{A.1}$$

Assume the Hankel transform and Fourier transform convention for the radial and height components, to apply to Equation A.1:

$$e(\rho,z)=\int_0^\infty \bar{e}(\lambda,z)J_1(\lambda\rho)\lambda d\lambda \tag{A.2}$$

$$\bar{e}(\lambda,z)=\frac{1}{2\pi}\int_{-\infty}^{\infty}\bar{\bar{e}}(\lambda,k)e^{+ikz}dk \tag{A.3}$$

And take advantage of the identities:

$$\frac{1}{\rho}\frac{\partial}{\partial\rho}(\rho\frac{\partial}{\partial\rho}\{J_1(\lambda\rho)\})=-\lambda^2 J_1(\lambda\rho) \tag{A.4}$$

$$\frac{\partial^2}{\partial z^2}e^{+ikz}=-k^2e^{+ikz} \tag{A.5}$$

Equation A.1 is converted to

$$[-\lambda^2-i\mu_0\sigma_0\omega-k^2]\bar{\bar{e}}(\lambda,k)=i\mu_0\omega\bar{\bar{J}}_s(\lambda,k) \tag{A.6}$$

where,

$$\bar{\bar{J}}_s(\lambda, k) = Iae^{+ikh} J_1(\lambda a) \tag{A.7}$$

Thus, the solution to Equation A.6

$$\bar{\bar{e}}(\lambda, k) = -\frac{i\mu_0\omega Iae^{+ikh} J_1(\lambda a)}{\lambda^2 - i\mu_0\sigma_0\omega + k^2} \tag{A.8}$$

Or in a simplified form:

$$\bar{\bar{e}}(\lambda, k) = -\frac{i\mu_0\omega Iae^{+ikh} J_1(\lambda a)}{\gamma_0^2 + k^2} \tag{A.9}$$

where,

$$\gamma_0^2 = \lambda^2 + i\mu_0\sigma_0\omega \tag{A.10}$$

To convert the solution A.9 back to spatial domain, the inverse Fourier transform is firstly applied on A.9, such that:

$$\bar{e}(\lambda, z) = -\frac{i\mu_0\omega Ia J_1(\lambda a)}{2\pi} \int_{-\infty}^{\infty} \frac{e^{ik[z+h]}}{\gamma_0^2 + k^2} dk \tag{A.11}$$

Considering the symmetry of the model, Equation A.9 is simplified as:

$$\bar{e}(\lambda, z) = -\frac{i\mu_0\omega Ia J_1(\lambda a)}{\pi} \int_{0}^{\infty} \frac{\cos\left(k[z+h]\right)}{\gamma_0^2 + k^2} dk \tag{A.12}$$

Calculating the integral in Equation A.12 using the commercial computational software Mathematica [76], which is:

$$\int_{0}^{\infty} \frac{\cos\left(k[z+h]\right)}{\gamma_0^2 + k^2} dk = \frac{\pi}{2\gamma_0} e^{\pm(\gamma_0[z+h])} \tag{A.13}$$

Still, the positive and negative sign in the exponential function is decided by the field diffusion direction. Thus,

$$\begin{aligned} \bar{e}(\lambda, z) &= \frac{-i\mu_0\omega Ia}{2\gamma_0} J_1(\lambda a) e^{\gamma_0(z+h)}, \quad z < -h \\ \bar{e}(\lambda, z) &= \frac{-i\mu_0\omega Ia}{2\gamma_0} J_1(\lambda a) e^{-\gamma_0(z+h)}, \quad z > -h \end{aligned} \tag{A.14}$$

Then apply the inverse Hankel transform with the kernel being Bessel function of the first kind to A.14, the solution to Equation 2.12 in spatial domain is

$$\begin{aligned} e^p_\phi(\rho, z) &= \frac{-i\mu_0\omega Ia}{2} \int_0^\infty \frac{\lambda}{\gamma_0} e^{\gamma_0(z+h)} J_1(\lambda a) J_1(\lambda\rho) d\lambda, \quad z < -h \\ e^p_\phi(\rho, z) &= \frac{-i\mu_0\omega Ia}{2} \int_0^\infty \frac{\lambda}{\gamma_0} e^{-\gamma_0(z+h)} J_1(\lambda a) J_1(\lambda\rho) d\lambda, \quad z > -h \end{aligned} \tag{A.15}$$

This is the primary field of electric component of a loop source in the whole space.

APPENDIX B

THE FINITE DIFFERENCE REPRESENTATION OF EQUATION 4.7

The discretization of Equation 4.7 majorly follows the scheme suggested by Oristaglio and Hohmann [55]. Figure B.1 shows the coordinate system of the grid. The nodes (z_i, x_j) locate on the vertexes of each cell. The value of e_y is evaluated on the node. Suppose the average products of conductivity and $s^{1-\beta}$ for the cells adjoining with the node are $[\sigma s^{1-\beta}]_{i,j}$, $[\sigma s^{1-\beta}]_{i+1,j}$,$[\sigma s^{1-\beta}]_{i,j+1}$, $[\sigma s^{1-\beta}]_{i+1,j+1}$, as indicated in the Figure, the area-weighted average of the property on node (z_i, x_j) is:

$$< \sigma s^{1-\beta} >= \frac{[\sigma s^{1-\beta}]_{i,j}\Delta z_i \Delta x_j + [\sigma s^{1-\beta}]_{i+1,j}\Delta z_{i+1}\Delta x_j + [\sigma s^{1-\beta}]_{i,j+1}\Delta z_i \Delta x_{j+1} + [\sigma s^{1-\beta}]_{i+1,j+1}\Delta z_{i+1}\Delta x_{j+1}}{(\Delta z_i + \Delta z_{i+1}) \times (\Delta x_{i+1} + \Delta x_{j+1})} \tag{B.1}$$

where Δz and Δx are node spacings in x and z directions. The discretized expression of Equation 4.7 is then:

$$\frac{1}{\Delta z_i \Delta z_{i+1}}\left[\frac{2\Delta z_{i+1}}{\Delta z_i + \Delta z_{i+1}} e^y_{i-1,j} + \frac{2\Delta z_i}{\Delta z_i + \Delta z_{i+1}} e^y_{i+1,j} - 2e^y_{i,j}\right] +$$
$$\frac{1}{\Delta x_j \Delta x_{j+1}}\left[\frac{2\Delta x_{j+1}}{\Delta x_j + \Delta x_{j+1}} e^y_{i,j-1} + \frac{2\Delta x_j}{\Delta x_j + \Delta x_{j+1}} e^y_{i,j+1} - 2e^y_{i,j}\right] = \mu_0 < \sigma s^{1-\beta} >_{i,j} e^y_{i,j} + \mu_0 s J_s \tag{B.2}$$

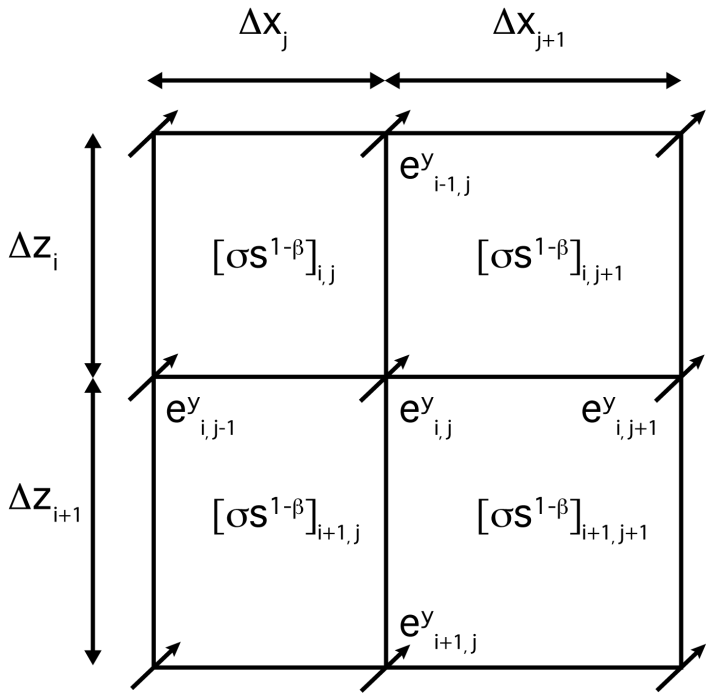

Figure B.1: The coordinate system for the discretized grid around node (z_i, x_j).